THE UNIVERSITY OF CHICAGO

MULTISCALE FEATURES AND MECHANISMS OF CORTICAL EPILEPTIFORM ACTIVITY

A DISSERTATION SUBMITTED TO
THE FACULTY OF THE DIVISION OF THE BIOLOGICAL SCIENCES
AND THE PRITZKER SCHOOL OF MEDICINE
IN CANDIDACY FOR THE DEGREE OF
DOCTOR OF PHILOSOPHY

INTERDISCIPLINARY SCIENTIST TRAINING PROGRAM:
NEUROBIOLOGY

BY
SOMIN LEE

CHICAGO, ILLINOIS
AUGUST 2022

to my spubbo

All generalization is a hypothesis. It ought always, as soon as possible and as often as possible, to be subjected to verification. If it does not stand this test, it ought to be abandoned without reserve. This is what we generally do, but sometimes with rather an ill humor. Well, even this ill humor is not justified. The physicist who has just renounced one of his hypotheses ought, on the contrary, to be full of joy; for he has found an unexpected opportunity for discovery.

-Henri Poincare, *La Science et L'Hypothese*, 1906

TABLE OF CONTENTS

LIST OF FIGURES

LIST OF TABLES

ACKNOWLEDGEMENTS

Sigmund Freud once said that the two cornerstones of life are work and love. After five years as a PhD student, I'm inclined to agree with him. This thesis would not have been possible without the countless number of people who have supported me in both arenas of life.

A huge amount of gratitude goes out to all who have supported me in work. Thank you to my high school calculus teacher, Dr. Kana Sris, who taught me the joy of learning and discovery. Thank you to Drs. Joel Mainland and Hiroaki Matsunami who so graciously took a chance on a high school student with no research experience and gave me my first taste of neuroscience. Thank you to Drs. Akira Sawa and Hanna Jaaro-Peled who encouraged me to pursue the career of a physician-scientist. An enormous amount of thanks goes to Drs. Marina Picciotto and Cali Calarco who supported me during my post-baccalaureate year.

Thank you to my advisor Dr. Wim van Drongelen, who gave me the confidence to join an EEG laboratory with little experience in math, signal processing, or programming. I could not have had such a successful pivot to a new field without your guidance, teaching, and support. Someone once told me that I probably won't like my PhD advisor by the time I'm done. I'm happy to say that we've proved them wrong.

Thank you to Drs. Naoum Issa and Shasha Wu. You have been great role models in my physician-scientist training, and I have learned a lot about what it means to be both an excellent clinician and researcher. Thank you to my remaining committee members, Dr. Jason MacLean and David Mogul, for providing me excellent discussions and feedback during my committee meetings. Finally, thank you to everyone in the MD/PhD office and the Neuroscience cluster office for helping me navigate the university and for making sure I always had all the resources I needed.

An equally large thanks goes out to those who have supported me in love. A happy scientist is a productive scientist, and I certainly could not have been happy without the support of my friends and family. Thank you, thank you, thank you to my parents who have been my personal cheering squad since day one. I know you thought it was a little crazy I wanted to do so much school, but you were nothing but supportive of my decision to start an 8+ year graduate program. Thank you to my husband Julian for being the most ridiculous and fun partner. Thanks for humoring me when I wanted to talk to you about science way past your bedtime, and thanks for helping me with my math homework when I was in way over my head. Thank you to my baby daughter Daphne for sleeping through the night. You constantly remind me that life doesn't have to be so serious.

A giant thanks to all my friends who have joined me for various parts of this journey. There are truly too many to thank properly, but a special acknowledgement goes out to Cali Calarco, my first and only work wife. I always thought friendships like ours were reserved for TV sitcoms, but I'm thrilled to say it happens in real life too. A special shout-out also goes to Reba Abraham for keeping things sane through my many existential crises. I really hope we start that flower farm one day.

ABSTRACT

Epilepsy is a neurological disorder characterized by recurrent, unprovoked seizures that produce a distinct signature of hypersynchronous neural activity in electroencephalographic (EEG) recordings. This phenomenon is generally attributed to hyperexcitability caused by an imbalance of excitatory and inhibitory activity in the brain. This model, however, does not sufficiently explain how seizures are generated since treatments that curb excitation and increase inhibition do not adequately treat 1/3 of epilepsy patients. These patients often turn to neurosurgical options to remove the culprit brain area suspected to be the origin of seizure activity. However, 1/3 of surgical patients fail to find adequate seizure relief, bringing into question the validity of how we identify, localize, and even conceive of epileptogenicity. The search for epileptogenic tissue is further complicated by the fact that seizures exhibit significantly different characteristics depending on the scale at which they are observed. Because observations do not readily translate across scales, accurate interpretation of clinical recordings requires in-depth understanding of seizure dynamics at various scales as well as knowledge of how these dynamics translate into recorded signals. To this end, the overall goal of this thesis is to gain a multiscale understanding of epileptiform activity using a combinination of signal analysis and mathematical modeling to develop mechanistically meaningful interpretations of clinical EEGs. This thesis is presented as a series of three studies. In the first study, we show that intracranial and extracranial EEG signals show a tight temporal coupling that suggests signals from deep brain sources may be detected by scalp EEG. In the second study, we present a novel method to obtain very low frequency activity in human ictal recordings. We then show that these low frequencies are observed at seizure onset. In the third and final study, we characterize the relationship between neural spiking and low frequency activity in epileptogenic brain areas. Throughout the presentation of these studies and in the concluding chapter, I discuss the potential clinical implications of these findings.

CHAPTER 1

INTRODUCTION

1.1 Epilepsy: a brief history

Seizures have likely been a feature of the human brain as long as human brains have existed, with the earliest written description of what we now call "epilepsy" dating to the Babylonians over 4500 years ago. This first record was not written so much as chiseled as it is a stone tablet describing an unconscious person turning left and right with froth flowing from the mouth (Labat, 1951). 1000 years later, the Babylonians would dedicate two full tablets[1] in their diagnostic text to epilepsy, referring to it as "the falling disease" (Wilson & Reynolds, 1990). Beyond Mesopotamia, descriptions of seizures have been found in the traditional medical text of all of the world's oldest civilizations including Egypt, Greece, China, and India (Panteliadis et al., 2017). The history of epilepsy is an ancient one that has spanned eras, cultures, and geography.

The earliest explanations of epilepsy were universally religious in nature with most ancient cultures attributing seizures to possession by demons or evil spirits (Temkin, 1994; Wilson & Reynolds, 1990). In the absence of any scientific understanding of the disease, those afflicted with epilepsy were frequently shunned as cursed, unclean, or immoral. Thus, epilepsy was considered the purview of priests and shamans, and the remedies offered were spiritual, taking the form of prayers and exorcisms (Gross, 1992; Temkin, 1994).

The scientific chapter in the story of epilepsy arguably starts in 400 B.C. with the publication of *The Sacred Disease,* an ancient Greek text that outlines the manifestations, causes, and treatments for seizures (Hippocrates, c.a. 400 B.C.E.).[2] *The Sacred Disease* offered a distinct

---

[1] Two is a remarkable number given that the whole series contains only 40 tablets meant to encapsulate "all diseases."

[2] The true authorship of *The Sacred Disease* remains unknown. It is an essay included in the larger body of work called the "Hippocratic Corpus," a collection of Greek medical texts with several authors that are attributed to Hippocrates for citation purposes (Temkin, 1994).

departure from the traditionally held spiritual explanations of epilepsy and emphasized that seizures are not the consequence of a diseased soul or demonic possession (Temkin, 1994). Epilepsy is instead described as an ailment of the brain and the body—an affliction no more divine than other somatic illnesses.

Despite the temporal chasm between *The Sacred Disease* and modern medicine, the description of a seizure provided in the text feels remarkably familiar:

> The patient becomes speechless and chokes; froth flows from the mouth; he gnashes his teeth and twists his hands; the eyes roll, and intelligence fails, and in some cases, excrement is discharged. These symptoms manifest themselves sometimes on the left, sometimes on the right, sometimes on both sides. (Hippocrates, c.a. 400 B.C.E.)

Evidently, the nature of seizures and its manifestations in the body has not changed throughout the course of human history. Our conception and understanding of epilepsy, however, has evolved significantly. Because society's relationship with epilepsy tends to reflect the prevailing scientific and religious views, treatments for epilepsy offers a sort of litmus test for the state of medicine in any given era.

In line with the medical theories proposed by contemporaries of his time, the author of *The Sacred Disease* provided a humoral explanation for seizures (Temkin, 1994). Epileptic fits were thought to be a consequence of an accumulation of phlegm in the brain. When the excess phlegm leaked out of the brain and entered the veins, the body contracted and trembled in response. Two millennia later in the era of Galen (2nd century AD), physicians began to describe seizures more distinctly as central or peripheral entities (Gross, 1992; Temkin, 1994). Auras, the phantom sensations that frequently precede a seizure, were first described and associated with specific somatic correlates as knowledge of human anatomy expanded (Gross, 1992).

By the 17th century, epilepsy was increasingly accepted as a brain disorder, although the underlying pathology was more widely believed to be vascular in nature (Temkin, 1994; World Health Organization, 2005). The study of epilepsy as a disorder of neural electrical activity emerged in the 18th and 19th centuries with the advent of modern neurology (Temkin, 1994). Inspired by Michael Faraday's new discoveries,[3] Dr. Robert Todd in 1849 first proposed an electrical hypothesis for seizures (World Health Organization, 2005). This hypothesis was later confirmed after Hans Berger's first human electroencephalogram (EEG) recording in 1929 (Berger, 1929).[4]

1.2 Current impact of epilepsy

The story of epilepsy and our attempts to describe and explain it is one that has engaged the human investigative spirit for many millennia. It is a story that continues today. Nearly 2500 years after the writing of *The Sacred Disease*, epilepsy still remains as one of the most common neurological disorders, affecting about 1% of the world population (World Health Organization, 2022). Beyond its high prevalence, epilepsy also accounts for 0.5% of the entire global disease burden with 12 million years of healthy life lost between 1990-2015 (Feigin et al., 2017).

The burdens of epilepsy for both the individual and society are multifold. Epilepsy patients, especially those who are not adequately treated, have reduced life expectancies and are at high risk for severe accidents and injury such as drowning and falling (Granbichler et al., 2017; Laxer et al., 2014; Tan et al., 2019). These risk factors can make tasks such as driving dangerous or impossible, resulting in reduced quality of life (Drazkowski, 2007). Comorbidities are high in

---

[3] Michael Faraday (1791-1867) was an English scientist who discovered many of the most fundamental concepts in electromagnetism (Williams, 2021).

[4] Although this seminal paper that is ubiquitously cited for the first human EEG recording was published in 1929, the actual recording was captured by Berger five years prior in 1924. History describes Berger as a melancholic man, and this delay in publication may have been driven by Berger's anxiety and self-doubts about the validity of what would eventually become one of the most important landmark moments in neurology (Kaplan, 2011).

epilepsy patients for both somatic (obesity, diabetes, stroke) and psychiatric (anxiety, depression, suicidal ideation) conditions (Keezer et al., 2016; Kobau et al., 2008; Tellez-Zenteno et al., 2007).

Epilepsy also carries a large socioeconomic burden as people with epilepsy report high rates of unemployment and low income (Kobau et al., 2008). Stigma is also prevalent in the lives of epilepsy patients in almost all spheres of life. Negative perception of people who experience seizures results in social exclusion and isolation at school, discrimination in work settings, and loss of friendship and romantic relationships (Shi et al., 2021).

1.3 Modern classification system for seizure disorders

Epilepsy is a neurological disease marked by the recurrence of unprovoked seizures (World Health Organization, 2022). More formally, the guidelines published by the International League Against Epilepsy (ILAE) states that a diagnosis of epilepsy can be made if any of the following criteria are met (Fisher et al., 2014):

1. At least two unprovoked (or reflex) seizures occurring more than 24 hours apart
2. One provoked (or reflex) seizure with a 60% or higher probability of further seizures over the following 10 years[5]
3. Diagnosis of an epilepsy syndrome

Due to the heterogeneous nature of seizures, however, it is difficult to talk about epilepsy as a single disorder. Like cancer, epilepsy is perhaps more accurately described as a large category of diseases. In an effort to standardize the descriptions of seizures and seizure disorders, the International League Against Epilepsy (ILAE) created in 2017 a structured way to classify seizures and epilepsy (Scheffer et al., 2017). This framework utilizes four components that can be used to

---

[5] 60% is the general recurrence risk of having a seizure after two unprovoked seizures.

describe a patient's seizure disorder: (1) seizure type, (2) epilepsy type, (3) epilepsy syndrome, and (4) etiology.

Seizure type refers to the characteristics of the onset of the seizure. There are three main categories: focal, generalized, and unknown. Although nuanced variations exist in the definition for these terms, focal seizures engage only one hemisphere, while generalized seizures engage distributed networks bilaterally.[6] Each of these types of onset can be further divided by their associated motor features and/or level of awareness. The guidelines list over a dozen motor descriptors, and a table of the "most common" behaviors during seizures features over 50 terms (Fisher et al., 2017).

Once a patient has a diagnosis of epilepsy, their epilepsy type and syndrome may be considered. Epilepsies may be generalized, focal, a combination of generalized and focal, or unknown. Epilepsy syndrome refers to clusters of clinical features that frequently occur together (Scheffer et al., 2017). The list of epilepsy syndromes is vast, but well-known examples include childhood absence epilepsy, Dravet syndrome, Lennox-Gastaut syndrome (Wilfong, 2022). Finally, etiology refers to the underlying cause for seizures. There are seven sub-categories: structural, genetic, infectious, metabolic, immune, and unknown (Scheffer et al., 2017).

Through such a framework, scores of different types of seizure disorders can be described in detail. The vast spectrum of different types of seizures, their etiologies, and clinical management is far too vast to be covered adequately in this introduction. For the purposes of this thesis, we will focus on the most common type of focal seizures in adults: temporal lobe epilepsy.

---

[6] Previously, the term "partial" was used to describe seizures with a limited area of onset, and "complex" was used for seizures that engaged the brain bilaterally. Because the clinical data used in this dissertation have been collected over the past several years, some clinical notations in the text use these older terms that are now considered outdated. For the purposes of this dissertation, "partial" is synonymous with "focal", and "complex" is synonymous with "generalized".

1.4 Temporal lobe epilepsy

The temporal lobe is an area that can be found on both sides of the brain, medial to the ears. It seems to be a particularly seizure-prone area of the brain—temporal lobe epilepsy (TLE) is the most common form of focal epilepsy in adults and accounts for over a quarter of all epilepsy cases (Asadi-Pooya et al., 2017; Stern, 2021; Tatum, 2012). Although temporal lobe seizures can occur both in the neocortex and mesial structures, the vast majority originate from mesial structures such as the hippocampus (Cendes, 2022; Stern, 2021). In these cases, the term mesial temporal lobe epilepsy (mTLE) may be used. A variety of lesions and pathologies such as cortical dysplasia, gliomas, traumatic and infectious lesions are associated with TLE, but hippocampal sclerosis is the most common and is present in over half of cases (Tatum, 2012).

TLE is one of the most treatment-resistant epilepsies, with approximately 1/3 of patients failing to achieve adequate seizure freedom through medications (Kwan & Brodie, 2000). These patients are then considered for surgical treatment. Although surgical outcomes are largely favorable, 1 of 3 surgical patients fail to achieve adequate seizure freedom, with up to 15% of patients seeing no improvement at all 1 year after surgery (Engel et al., 2003; Spencer & Huh, 2008; Téllez-Zenteno et al., 2005).

1.5 Surgical planning in temporal lobe epilepsy

Because most seizures in TLE are focal, patients are often good candidates for surgical intervention (Stern, 2021). The goal of epilepsy surgery is to remove the area of the brain that generates seizures. This culprit brain tissue is known as the epileptogenic zone (EZ), a theoretical brain area that is somewhat tautologically defined as the minimum amount of cortex that must be resected to produce seizure freedom (Jehi, 2018; Rosenow & Lüders, 2001). It is an area that can only be confirmed retrospectively as it depends on the final surgical outcome. Hence, for the purposes of surgical planning, the seizure onset zone (SOZ) is frequently used as a proxy for the EZ (Jobst et al., 2020). The SOZ is defined as the brain area where seizure activity is first observed by clinical electrodes (Rosenow & Lüders, 2001). The variety of clinical approaches and tests that are utilized to identify the SOZ/EZ are discussed in this section.

1.5.1 Seizure semiology

Seizure semiology refers to the description of clinically observable behaviors associated with a patient's seizures (Tufenkjian & Luders, 2012). Because seizures can exhibit specific features depending on the affected brain area, semiology can provide information about the anatomical area that is engaged during seizures. This area is known as the symptomatogenic zone and may overlap with or be proximate to the EZ (Chowdhury et al., 2021; Tufenkjian & Luders, 2012). Consequently, semiology may have value in helping identify the EZ, especially when imaging modalities do not point to a specific lesion (Tufenkjian & Luders, 2012).

Seizure semiology may be divided into four main categories: sensory/auras, motor, consciousness, and autonomic (Rossetti & Kaplan, 2010). Auras are common in TLE and are typically experiential (e.g., feelings of anxiety, déjà vu, fear) or viscerosensory (e.g., nausea). Perseverative automatisms involving the mouth and/or hands are also common (Blair, 2012). Most seizures in TLE are focal with impaired consciousness.

There are some limitations to using seizure semiology as a localization technique. Seizure semiology may have no localizing value if the symptoms are a consequence of seizure activity spreading to an area rather than originating in that area (Blair, 2012). Furthermore, different semiology categories can have different efficacy for helping localize seizures (Marks & Laxer, 1998). For example, auras seems to be reliable for differentiating between frontal lobe and temporal lobe focal seizures (Blair, 2012), but some motor manifestations are less reliable and may even allow correct lateralization of seizures (Marks & Laxer, 1998; Tufenkjian & Luders, 2012). Thus, seizure semiology is most effective when used in combination with other assessment tools such as scalp EEG (Serles et al., 2000). Finally, seizure semiology can be very subjective, and assessments can be highly variable among evaluators, necessitating the need for standardization (Tufenkjian & Luders, 2012).

1.5.2 Clinical electroencephalograms

Although clinical signs and symptoms are a useful tool in evaluating TLE, seizures are most definitively described by their electrographic features. One of the most important tools in the assessment of epilepsy is the electroencephalogram (EEG), a method that allows monitoring of the brain's electrical activity. Neural activity generates ionic currents, and the electric potential generated by the action of many synchronized neurons is reflected in the EEG recording.[7] The normal, healthy human brain exhibits a variety of electrical patterns, and aberrant patterns point to the presence of brain pathologies.

A variety of different types of EEG electrodes are used clinically in the assessment, diagnosis, and management of TLE. The scalp EEG is used in most initial assessments for seizure patients as it is the least invasive method. Electrodes are placed on the head following a standardized layout known as the international 10-20 system (Fig. 1.1A). The system includes 21 electrodes, each of which are assigned a letter and number that identifies its location on the head.[8]

---

[7] "Many" is a number that is dependent on a variety of factors such as the recording modality, the brain area that is being monitored, and the pathology being studied.

[8] It is not uncommon practice for clinical recordings to include additional electrodes in the spaces between the electrodes in the 10-20 layout. The positions of the additional electrodes are typically borrowed from the higher density 10-10 system (Jurcak et al., 2007).

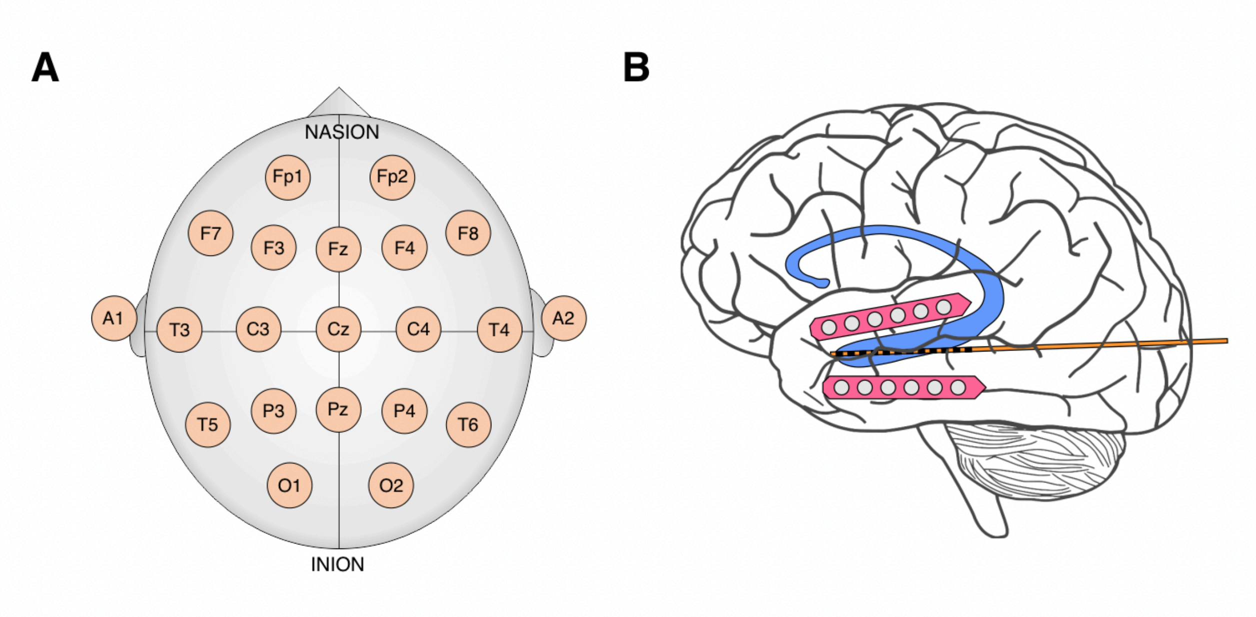

Figure 1.1. Illustrations of clinical EEG modalities.
(A) Schematic of scalp EEG electrode placement using the international 10-20 system. The 10 and 20 refer to the fact that the spacing between electrodes are 10% or 20% of the length of the skull along the front-back and left-right axes. The nasion is the bridge of the nose, and the inion is the bony prominence at the midline of the occipital bone. Even numbers are used for electrodes in the right hemisphere, and odd numbers are used for electrodes in the left hemisphere. Smaller numbers indicate greater proximity to the midline, and the letter z is used in lieu of a number for electrodes directly on the midline. Letters indicate the anatomical region of the electrode. Fp = pre-frontal, F = frontal, T = temporal, P = parietal, O = occipital, C = central, A = auricle.
(B) Electrocorticography electrodes (pink) may be in grid or strip form and are placed directly on the surface of the brain. The strip form is depicted in this figure. Depth electrodes (orange) are inserted into the brain for monitoring deeper structures such as the hippocampus (blue).

Because electrical potentials attenuate sharply with distance, the scalp EEG requires relatively large and distinct waveforms due to its distance from the brain (Nunez et al., 2006). The generation of potentials measurable by a distant electrode requires many neurons to fire and induce currents in synchrony and in the same direction. Consequently, scalp EEG is thought to largely reflect the summed activity of tens of millions to hundreds of millions of neurons in the neocortical surface of the brain on the order of 6cm^2 (Britton et al., 2016).[9] Although the spatial resolution for the scalp EEG is relatively poor, rough approximation of the SOZ and seizure lateralization is possible, especially in cases where seizures engage large neocortical areas.

To improve localizing power, the scalp EEG may be used in combination with other imaging methods such as positron emission tomography (PET), computerized tomography (CT), and magnetic resonance imaging (MRI) to more precisely identify a seizure locus (Rosenow & Lüders, 2001). In cases where a clear lesion is identified that is concordant with seizure semiology and scalp EEG, surgery may proceed without further invasive monitoring (Diehl & Lüders, 2000; Rathore & Radhakrishnan, 2015).

For some patients, the addition of more invasive EEG assessments may be indicated. For example, patients whose scalp EEG results are not concordant with imaging and/or seizure semiology, patients with no lesion identified on MRI, or patients with diffuse cortical dysplasia may require invasive studies (Jayakar et al., 2016; Rathore & Radhakrishnan, 2015). Additionally, invasive monitoring is indicated for patients whose seizures are suspected to be close to eloquent areas,[10] since a high level of spatial precision is desirable to avoid detriment to critical functions during neurosurgery (Rathore & Radhakrishnan, 2015).

Two main forms of invasive monitoring are electrocorticography (ECoG) and depth electrode recordings (Fig. 1.1B). For ECoG recordings, grids or strips of electrode contacts are placed directly on the surface of the brain. For recording from deeper structures, depth electrodes may be inserted into the brain. A major advantage of intracranial monitoring over scalp EEG is high spatial resolution. The diameter for the field of view for intracranial electrodes is thought to be ~2-3mm to ECoG contact and ~1-2mm for depth electrodes (Dubey & Ray, 2019; Parvizi &

---

[9] The neocortex is not only closest to the scalp but also contains large pyramidal neurons whose projections are in columnar, parallel form, allowing for summation of currents.

[10] "Eloquent cortex" is a term that entered the neurosurgical lexicon in the 1950's and refers to those brain areas that have functions such as motor, sensory, and language processing (Kahn et al., 2017).

Kastner, 2018). In many cases, a combination of depth and ECoG electrodes are used to monitor a single patient. The cost of high spatial resolution is the risk of undersampling, as it is hard to get coverage for large areas of the brain (Parvizi & Kastner, 2018).

Recordings from these probes are generally used to identify the seizure onset zone (SOZ). The SOZ is defined by the location of the electrode that first records seizure activity, and the resection area is identified by using all of the different clinical approaches in combination (Jobst et al., 2020; Rosenow & Lüders, 2001). Depending on the size of the area to be removed, laser ablation or resection may be performed. Laser ablations are used for smaller areas, and resections are preferred for areas larger than 1-2cm (Jobst et al., 2020).

1.6 Markers of epileptogenicity

Despite the extensive work that goes into localizing an epileptogenic focus for surgical resection, 1/3 of TLE surgical patients do not find adequate seizure freedom (de Tisi et al., 2011). Why does surgical resection fail for these patients? There are several reasonable hypotheses:

- The seizure had multiple onset foci, only one of which was detected and resected.
- The SOZ was poorly delineated, and some epileptogenic tissue was left behind.
- The seizure may have started elsewhere and propagated to the tissue recorded by the electrodes. Therefore, the SOZ was incorrectly identified due to undersampling.

There is one additional hypothesis that challenges our fundamental understanding of seizures. It is one that is of particular relevance to this thesis:

- The repertoire of electrographic features used to identify epileptogenic tissue is limited and incomplete.

This last hypothesis implies that the range of electrographic features that we associate with epileptiform patterns must be expanded. In this section, I review the evidence for some emerging markers of epileptogenicity, their potential, and current limitations.

1.6.1 Interictal epileptiform activity

The interictal period refers to the periods of time between a patient's seizures. Even when there is no active seizure activity, epilepsy patients tend to exhibit aberrant waveforms on EEG (Tatum, 2021). Interictal epileptiform discharges (IEDs) are large, transient paroxysmal events that happen in the absence of ictal events (Pillai & Sperling, 2006). IEDs are considered diagnostically important in the evaluation of epilepsy, as they are nearly ubiquitously observed in epilepsy patients (Staley & Dudek, 2006; Tatum, 2021; Vollmar et al., 2018). Their features can be quite heterogeneous, but common waveforms include sharp waves and spike-wave complexes (Kural et al., 2020; Noachtar & Remi, 2009). They can be observed through both extracranial and intracranial recording methods, but they are generally much more prominent in intracranial recordings, especially in the context of TLE (Pyrzowski et al., 2021).

IEDs have been traditionally considered a marker of epileptogenicity as they are frequently associated with the SOZ (Jobst et al., 2020; Tatum, 2021). IEDs also seem to have similar spatiotemporal properties as ictal discharges, such as location and direction or spread (Smith et al., 2022). Interictal discharges may also be useful as an early prodrome marker of epilepsy, as there is evidence that incidental findings of interictal discharges increases the risk of epilepsy diagnosis in the future (Seidel et al., 2016).

The utility of using IEDs as part of surgical planning, however, remains in debate (Dworetzky & Reinsberger, 2011). Higher rates of IEDs have been associated with increased risk of developing treatment resistant epilepsy and decreased surgical success (Krendl et al., 2008; Napolitano et al., 2021). The continued presence of IEDs post-surgery has also been associated with poor outcomes (Rathore & Radhakrishnan, 2010). A different study, however, showed that leaving behind some areas showing IEDs did not negatively impact surgical outcome (Kim et al., 2010). A study that used source localization on IEDs showed that resection of IED sources on ECoG resulted in better surgical outcomes (Lee et al., 2014), although the fact that IEDs can propagate makes them difficult to localize (Alarcon et al., 1997; Alarcon et al., 1994). Furthermore, the spatial distribution of IEDs, however, can fluctuate over time, making their spatial localization benefits less useful. (Conrad et al., 2020).

The use of interictal information is desirable because most recordings obtained from patients are interictal. Seizures are relatively rare events, and sometimes several days of monitoring is required to successfully capture a recording (Tatum, 2021). Therefore, getting useful information out of interictal recordings has the potential to dramatically reduce monitoring time and lengths of hospital stays.

One limitation of using IEDs is that they may be hard to detect non-invasively, especially when they originate from deeper structures. There is some evidence, however, that IEDs may have subtle features that allow for their identification on scalp EEG (Pyrzowski et al., 2021). Another limitation to using IEDs is that they may sometimes be misdiagnosed in non-epilepsy patients as there are some sharp transients that are normal variants but can be confused with epileptiform activity (Noachtar & Remi, 2009).

1.6.2 Epileptiform activity in unconventional frequency bands[11]

Real-world signals are typically composed of a heterogenous mixture of frequencies, and the recordings of neural activity are no exemption. Consequently, seizures can look remarkably different depending on the frequency band that is used for signal visualization. Clinical assessment occurs mostly in the relatively narrow range of 1-30Hz. There is increasing interest,

---

[11] This section is adapted from Lee, S., Issa, N.P., Rose, S., Tao, J.X., Warnke, P.C., Towle, V.L., van Drongelen, W., Wu, S. (2020). DC shifts, high frequency oscillations, ripples and fast ripples in relation to the seizure onset zone. *Seizure*. 77:52-58. doi: 10.1016/j.seizure.2019.05.001.

however, in studying seizure activity below and above this conventional range to help identify the EZ (Modur et al., 2012).

On the high end of the frequency spectrum are high frequency oscillations (HFOs). HFOs are defined as events faster than 80Hz with at least four oscillations that are distinct from background activity (Frauscher et al., 2017).[12] They have emerged as a marker of interest in identifying the EZ since they have been associated with various seizure onset patterns (Ferrari-Marinho et al., 2016; Weiss et al., 2016). Additionally, both retrospective and prospective studies have demonstrated that resection of areas with high rates of interictal HFOs is correlated with better surgical outcomes (Akiyama et al., 2011; Fedele et al., 2017; Fujiwara et al., 2012; Haegelen et al., 2013; Jacobs et al., 2010; Weiss et al., 2015). Inversely, the continued presence of HFOs post-surgery predicts poor seizure outcome (van 't Klooster et al., 2015).

At the opposite end the frequency spectrum is infraslow activity (ISA), which is defined as EEG activity below 0.5Hz (Modur et al., 2012; Thompson et al., 2016).[13] Similar to HFOs, slow oscillations have been associated with seizure onset patterns (Gumnit & Takahashi, 1965; Kanazawa et al., 2015; Rampp & Stefan, 2012; Wu et al., 2014). ISAs also seem to hold some promise as a marker of the EZ as full resection of areas with ISA activity has been associated with more positive surgical outcomes (Ikeda et al., 1999).

HFOs and ISAs may also help define a narrower area of tissue as they are more spatially restricted than conventionally assessed SOZ (Ikeda et al., 1996; Mader et al., 2005; Modur, 2014; Modur & Scherg, 2009; Rampp & Stefan, 2012; Rodin & Modur, 2008; Wu et al., 2014). Although

---

[12] In the literature, HFOs are sometimes divided into high gamma (80-150Hz), ripples (80-250Hz), fast ripples (250-500Hz), and very high-frequency oscillations (500-2000Hz). These ranges are somewhat arbitrary, however, and the exact definition of these bands varies by authors. The potential clinical implication of these subdivisions is a field of active research. In this introduction, I use the term HFO for all activity greater than 80Hz.

[13] In the literature, the term ictal baseline shift (IBS) or DC shifts is also used to refer to slow activity in ictal recordings. The term DC refers to direct current, and its use originates from the requirement of DC amplifiers to view the very low frequency signals (Rodin & Modur, 2008). For the purposes of consistency, I typically use the term ISA throughout this thesis.

very few studies have directly addressed the combined effects of using ISA and HFOs together, co-occurrence of HFOs and ISAs within the EZ has been observed (Gnatkovsky et al., 2014). Although the phase relationship between ISA and HFO as a marker of ictal activity is a recent and promising line of research (Hashimoto et al., 2020, 2021), the vastly different time scales make comparing the temporal dynamics of these two frequency bands difficult.

The study of unconventional frequencies in ictal EEGs has been hampered not by lack of interest, but rather by the limited technical ability to record such frequencies. Accurate and meaningful analysis of fast frequency activity is contingent upon several features of the EEG recording system. According to the Nyquist theorem, sampling rates used to record HFOs should be at least two times the upper bound of the frequency band of interest (Van Drongelen, 2018). Realistically, even higher rates are required to determine wave morphology. Additionally, low noise systems are particularly important for recording HFOs as they tend to have very low amplitudes (Zijlmans et al., 2017). Finally, because HFOs happen on such small timescales, visual analysis can be particularly time consuming, necessitating the development of automated detection algorithms (Wong et al., 2021).

Although the ability to record HFOs has been improved by increasing sampling rates in clinical EEGs, infraslow activity still presents a technical challenge in the actual recording process. EEG recording systems necessarily include a high-pass filter early in the measurement chain to remove large artifactual drifts that can saturate recording elements such as the amplifier. This filter unfortunately attenuates any legitimately seizure-related low frequencies, making ISA difficult to study in many EEG recordings. The studies that have utilized DC amplifiers to bypass this issue have largely been limited to the study of healthy subjects in experimental conditions (Grooms et al., 2017; Picchioni et al., 2011; Rodin et al., 2017) because standard clinical EEG equipment do not utilize DC amplifiers. Consequently, direct study of ISA in human ictal recordings has been limited.

1.6.3 Epileptiform activity across spatial scales

What a seizure looks like can vary dramatically across spatial scales. On one end of the spectrum are the single neurons whose primary action is to spike. On the other end are large local field potentials (LFPs) that are the summation of the spiking of many neurons of millions of neurons (Nunez et al., 2006). How the activity of these single neurons translates into global activity patterns is an active field of research.

Although recording from single cells has technical challenges that are difficult to overcome in the context of clinical patient recordings, microelectrodes allow us to observe the spiking activity of small populations of neurons. The arrays used for this thesis are 96 channel microelectrode arrays (MEA), sometimes called Utah arrays.[14] They are 4mmx4mm in size and are typically implanted in the putative seizure onset zone that was determined through conventional clinical methods (Fig. 1.2). The fast frequency activity measured by these electrode arrays is termed multiunit activity (MUA) and is thought to reflect the action potential or spiking activity of small or single neuronal units (Harrison & Pantelis, 2010).

---

[14] The Benhke-Fried depth electrode is another microelectrode option that is commercially available, but they were not used for any of the studies presented in this thesis. They are essentially depth electrodes that contain several microwires that fan out at the tip (Misra et al., 2014).

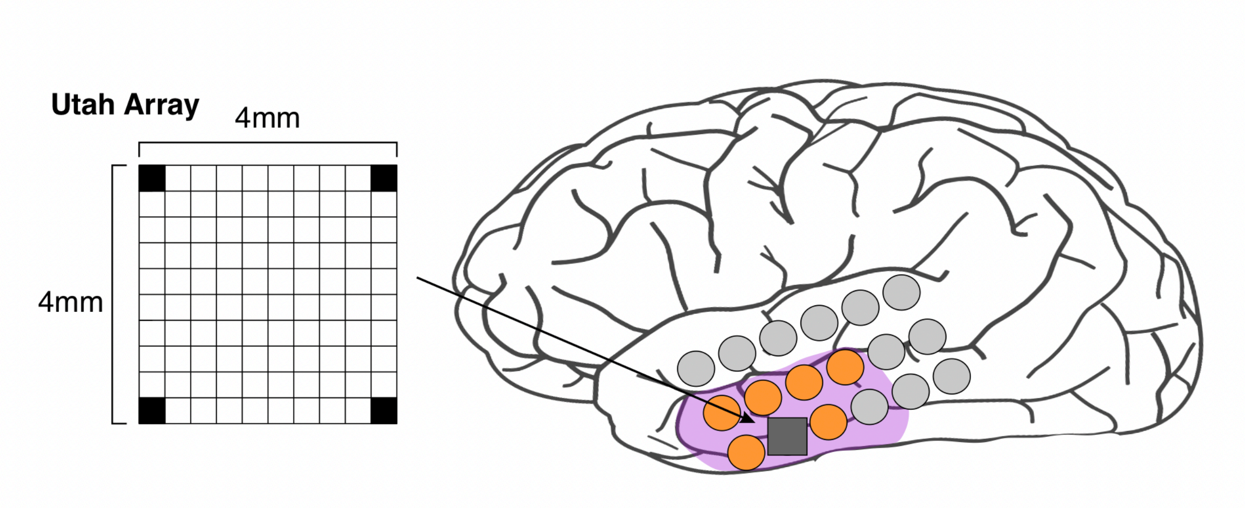

Figure 1.2. Schematic of a Utah microelectrode array (MEA) and example of array placement in surgical planning for a patient with temporal lobe epilepsy.
The Utah array is a 4mm x 4mm 96-electrode array that is arranged in a 10 by 10 grid of electrodes with empty corners. After assessment via electrocorticography, the MEA is placed in the putative seizure onset zone (dark gray square). Orange electrodes indicate areas that showed early seizure activity. Shaded purple area shows the part of the brain planned for resection.

Research using these arrays has let us glean how seizures manifest at spatial resolutions not achievable by conventional clinical recordings. What was uniformly referred to as the SOZ is a much more heterogeneous entity when viewed at a smaller scale. One study found that for a MEA implanted in the seizure onset zone, only 1/3 of electrodes showed any ictal activity related changes, suggesting that neurons in the SOZ behave heterogeneously (Bower et al., 2012). Another study showed that a MEA recording of an interictal epileptiform discharge (IED) showed the IED waveform in only a subset of channels, suggesting that the underlying tissue may actually be more mosaic (Yang et al., 2021).

MEA studies have demonstrated that cortical tissue that has been classically defined as the SOZ can be subdivided into two areas: recruited and unrecruited (Eissa et al., 2017; Schevon et al., 2012; Weiss et al., 2013).[15] The two areas are separated by a moving and spreading boundary known as the seizure wavefront (Schevon et al., 2012; Smith et al., 2022). In the recruited area, multi-unit spiking activity shows high levels of spiking activity that is also highly correlated with the overlying seizure LFP. In the unrecruited areas, spiking increases more moderately. Importantly, this spiking activity in unrecruited areas is not well correlated to the low frequency LFP. These two zones, as well as the wavefront, are not identifiable with lower spatial resolution modalities such as ECoG and depth probe recordings.

Additional studies have shown that the spiking activity in the recruited zone is correlated with overlying LFP activity in brain tissue that is on the order of several centimeters away from the putative SOZ (Eissa et al., 2017). These studies in sum paint a picture in which small micro to mesoscale ictal networks engage the macro-level hypersynchronous ictal activity that is observed in clinical recordings.

A major limitation in MEA studies is that they are very small, and it is impractical to sample from multiple brain areas. Consequently, obtaining a recording that captures activity from different types of seizure territories (i.e., recruited and unrecruited) is nearly impossible. Methods that allow for wider coverage studies are starting to be conducted using newer probes (Paulk et al., 2022). Additionally, the currently available dataset of these recordings is very limited due to the small number of patients who are participating in these studies.

1.7 Overview and aims of thesis

The elusive hunt for epileptogenicity raises a conceptually simple but philosophically complicated question—exactly what does a seizure look like? The issue becomes non-trivial when one realizes that seizures exhibit markedly different characteristics depending on the scale at

---

[15] The terms “core” and “penumbra” were used in the literature when this phenomenon was first reported. More recent studies have shifted to using the terms “recruited” and “unrecruited” as nuances in the spatial and temporal evolution of these areas have been characterized in greater detail. The work presented in this dissertation uses the terms “recruited” and “unrecruited”.

which they are observed. This complication is furthered by the numerous modalities and equipment used to monitor neural activity, ranging from scalp EEG electrodes that detect cumulative activity from millions of neurons to microelectrode arrays that have near single-neuron resolution. Because observations of neural activity do not readily translate across scales, accurate and meaningful interpretation of clinical recordings requires an in-depth understanding of which facets and mechanisms of seizures are captured by each recording method.

This thesis aims to fill some of the gaps in our ability to link the manifestations of epileptiform activity in EEG recordings across scales and frequencies with their underlying mechanisms by asking the following three questions:

1. How do seizure dynamics change across spatial and temporal scales?
2. How do these dynamics manifest in recorded EEG signals?
3. What may be the biological mechanisms underlying these dynamics?

The overall goal of this thesis is to characterize multiple facets of epileptiform activity by using a combination of clinical patient data, mathematical modeling, and signal analysis to develop mechanistically meaningful interpretations of clinical EEG. To achieve this goal, this thesis describes three projects in chapter 2-4.

Chapter 2: Characterization of the manifestations of hippocampal interictal activity in scalp EEG recordings

In this chapter, I will show that scalp EEG recordings can be used to detect and characterize distinct groups of hippocampal interictal discharges. By using signal analysis applied to a dataset composed of simultaneous intracranial and scalp recordings of temporal lobe epilepsy patients, I show that hippocampal interictal discharges are temporally associated with identifiable features in scalp EEG. I then show evidence that these scalp features are likely to reflect the hippocampal discharges through volume conduction and propagation, and that characterization of the scalp signals may help elucidate these different types of discharges.

Chapter 3: Digital reconstruction of infraslow activity in ictal recordings

In this chapter, I present a digital, inverse-filter tool that uses deconvolution to reconstruct the infraslow activity (ISA) in ictal recordings. I then show that reconstruction of ISA allows for observations of seizure onset and offset not visible via current methods. Finally, I discuss potential applications in applying reconstructed ISA to characterize the seizure onset zone.

Chapter 4: Characterization of the spatiotemporal relationship between ictal spiking and LFP during human focal seizures

In this chapter, I show that the spiking activity of individual neurons has a distinct temporal and spatial relationship to the overlying low-frequency local field potential. I show that there is a special mathematical relationship to these spatial and temporal patterns. Finally, I discuss how different patterns may allow identification of different mechanisms underlying focal seizures.

Chapter 5 is the concluding chapter for this dissertation in which I summarize the major findings presented in this thesis. I then discuss the potential future directions and clinical research and end with some closing thoughts.

1.7.1 A brief note on navigating this thesis

Chapter 2, 3, and 4 all have the same format. The summary and introduction sections are followed directly by the results and discussion. The methods are described in the last section of each chapter. I chose to present the results first to avoid burdening the reader with methodological details such as the specifics of patient recruitment, software versions, and stepwise explanations of analysis pipelines. While these details are necessary and useful, I felt that they detracted from the storyline when presented first without the context of the results and discussion. In places where I felt it was useful to do so, I periodically refer the reader to the methods section in the course of presenting the study's results. This in all cases refers to the "Methods" section found at the end of that given chapter.

CHAPTER 2

Manifestation of hippocampal interictal discharges on clinical scalp EEG recordings[1]

2.1 Summary

Epileptiform activity limited to deep sources such as the hippocampus is widely thought to be undetectable on scalp EEG. In this study, we challenge this notion and present evidence that interictal discharges restricted to the hippocampus have detectable effects on the scalp's electric field. Using paired intracranial and scalp EEG recordings obtained from 17 patients, we show that hippocampal interictal epileptiform activity visibly contributes to scalp EEG recordings and that these contributions are significant enough to be useful in a clinical setting. We first show that hippocampal spike-triggered averaging of the scalp EEG reveals clear signals that are temporally coincident with intracranially-recorded hippocampal interictal discharges. We then show that these signals have characteristics of hippocampal potentials that reach the scalp electrodes via volume conduction. Cross-correlation of intracranial hippocampal discharges with their associated scalp signals resulted in two classes of scalp waveforms—one with no time delay from the associated hippocampal discharges and another with significant delays between the observed scalp and hippocampal signals. Additionally, the scalp signals with no delay showed topographies with a broad field with higher amplitudes on the same side of the head as the hippocampal discharges and a left-right flip in polarity over the course of the discharge—observations that are consistent with a unilateral signal originating from an ipsilateral deep source. In contrast, scalp waveforms showing significant time lags showed a more complex, rotational dynamic, suggesting

---

[1] This chapter is adapted from Lee, S., Wu, S., Tao, J.X., Rose, S., Warnke, P.C., Issa, N.P., van Drongelen, W. (2021). Manifestation of Hippocampal Interictal Discharges on Clinical Scalp EEG Recordings. *Journal of Clinical Neurophysiology*. doi: 10.1097/WNP.0000000000000867

synaptic propagation and engagement of other brain areas may underlie these scalp patterns. Together, these results show that the topographic evolution of scalp manifestations of hippocampal interictal discharges may be used to distinguish spikes that are limited to the hippocampus from those that travel to or engage other brain areas.

2.2 Introduction

Mesial temporal lobe epilepsy (MTLE) is the most common form of focal epilepsy in adults, comprising over a quarter of all epilepsy cases (Asadi-Pooya et al., 2017; Stern, 2021). Despite its prevalence, MTLE is difficult to diagnose because hippocampal epileptiform activity is not readily identifiable on scalp electroencephalography (EEG) (Koessler et al., 2015; Wennberg et al., 2011). Previously, a quantitative study showed that hippocampal spikes produce on average 7μV deflections on scalp EEG, making them difficult to distinguish from background fluctuations of ~10μV. This observation led to the conclusion that hippocampal discharges can generate clinically detectable signals on scalp recordings only with the engagement of an extended neocortical network (Koessler et al., 2015). In early MTLE, however, epileptiform activity may be restricted to the hippocampus, and the development of scalp EEG methods for detecting signals from deep brain sources is important for early diagnosis (Jacoby et al., 1996; Sperling, 2004), prevention of misdiagnoses (Mirsattari et al., 2011), and reducing delay in getting definitive treatment (Berg, 2004; Simonato et al., 2012).

In contrast, some theoretical studies have argued that deep discharges might be detectable by both EEG and magnetoencephalography (MEG) (Attal et al., 2007; Goldenholz et al., 2009). This theoretical finding was recently corroborated by a study demonstrating that individual hippocampal discharges can sometimes be detected by MEG (Pizzo et al., 2019). In a clinical study, a subset of intracranially recorded hippocampal discharges were associated with waveforms visible on scalp EEG (Issa, Wu, et al., 2018). This study, however, could not preclude the possibility that the scalp waveforms were reflective of epileptiform activity that also engaged neocortical areas outside the hippocampus.

In this study, we provide evidence that hippocampal signals manifest on scalp recordings and result in distinct topographic patterns on the scalp that may allow inference of the nature of the underlying intracranial activity. These scalp topographies could be differentiated by their timing in relationship to the hippocampal activity, opening up the possibility that epileptiform activity limited to the hippocampus may be identified and characterized through noninvasive recording methods. Using simultaneous intracranial and scalp EEG recordings of hippocampal interictal epileptiform discharges, we provide evidence that hippocampal discharges are associated with signals observable in scalp recordings that fall into two categories: scalp signals that are consistent with the volume conduction of a single, deep, unilateral source, and scalp signals suggestive of epileptiform that engages other brain areas through physiological mechanisms such as synaptic propagation. The ability to characterize and differentiate hippocampal discharges using scalp EEG would improve diagnostic power, prevent misdiagnoses, and potentially reduce the need for invasive intracranial monitoring in the diagnosis and treatment of MTLE.

2.3 Results

2.3.1 Classification of hippocampal interictal discharges

Hippocampal interictal discharges were recorded on intracranial electrodes in 16 patients. Individual discharges from individual subjects were detected with an automated algorithm and grouped based on morphological similarity in the time domain using connected components analysis (Methods). Across the 16 patients, 42 groups of hippocampal discharges were found. A spike triggered average (STA) was calculated for each group using the hippocampal discharge as the trigger (Fig. 2.1). Figure 2.1A shows example STA signals from hippocampal depth electrodes for the five groups of discharges found in Patient 1. In groups 1, 2, 3, and 5, scalp EEG amplitudes were larger on the temporal channels ipsilateral to the spiking hippocampus and were inverted in polarity on the left temporal channels (Fig. 2.1B). Group 4, which had the smallest intracranial signals (Fig. 2.1A), also showed the smallest scalp signals with maximal amplitudes in frontal channels (Fig. 2.1B). Scalp EEG amplitudes ranged between 1 and 19μV with an average±standard deviation of 5.5±4.1μV (N=42 groups; Fig. 2.2).

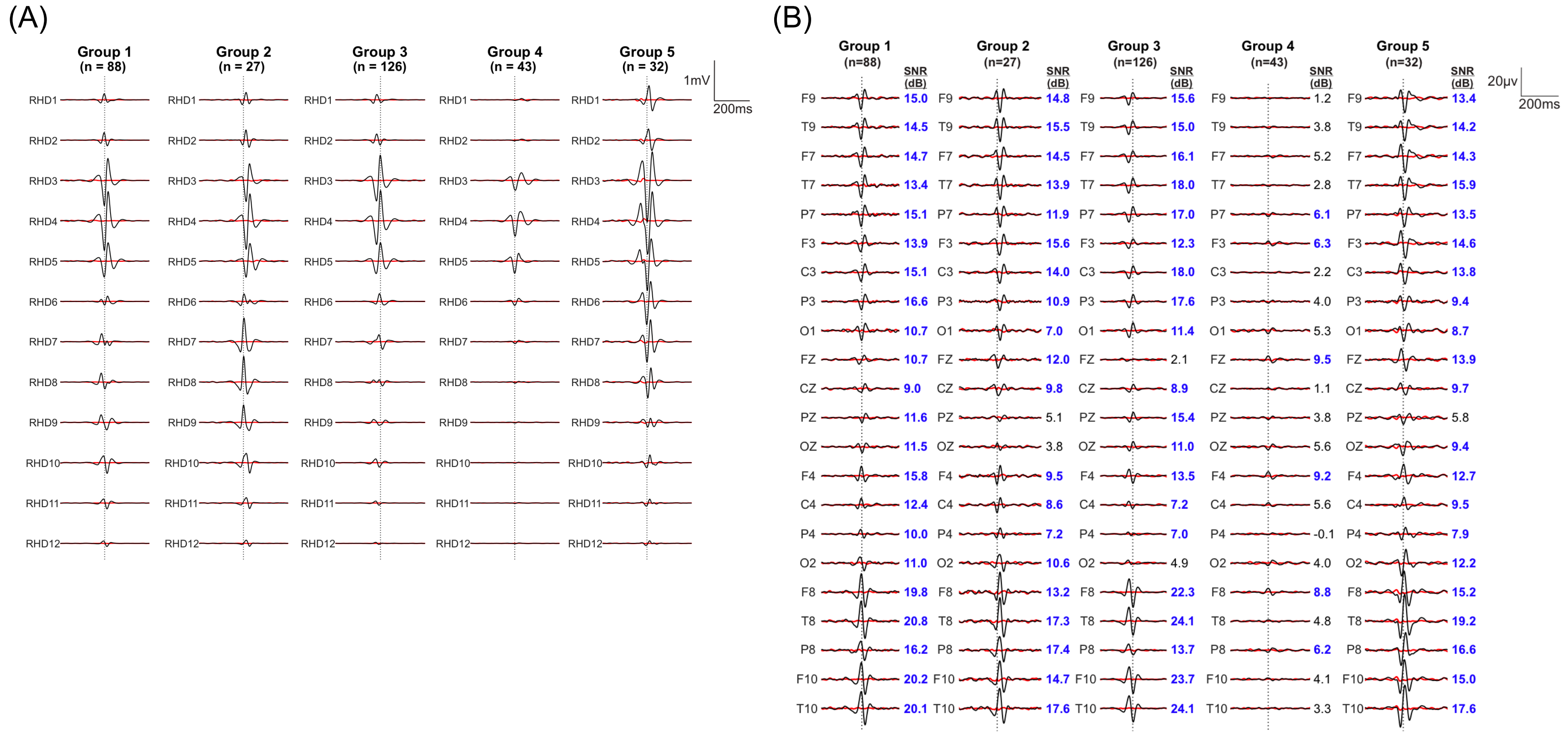

Figure 2.1. Spike triggered averages (STAs) for the hippocampal discharges in the five groups of Patient 1. Black traces are the STAs and the red traces show the associated noise estimates. Noise was estimated in the 250ms epochs before and after the discharge epoch of 500ms. **(A)** STAs of intracranial channels. The depth electrode label is indicated for each waveform. RHD = right hippocampal depth electrode. RHD1 is the most anterior contact, and RHD12 is the most posterior contact. **(B)** STAs of scalp EEG channels. The electrode location and the SNR (dB) are indicated left and right for each waveform. SNR values greater than 6dB are denoted in blue.

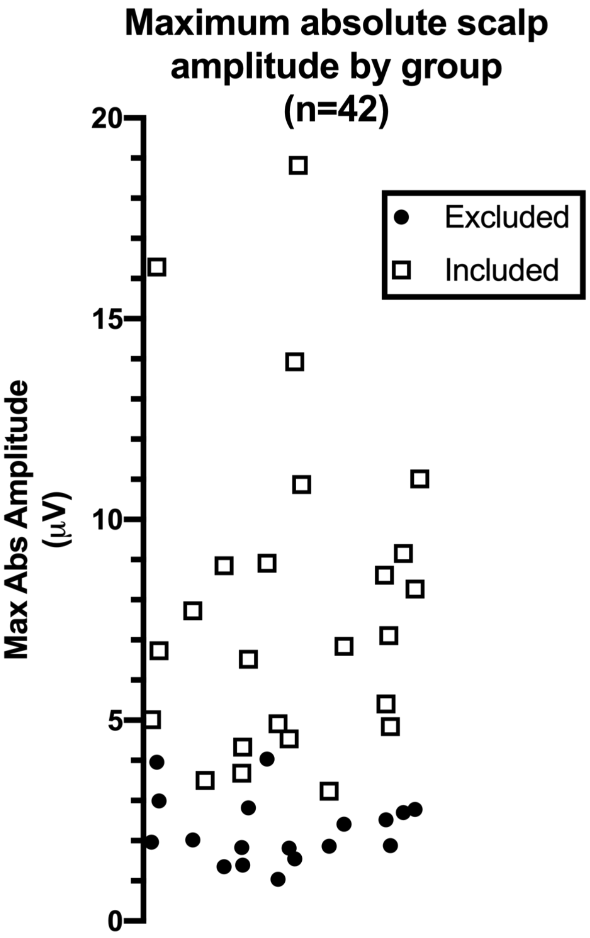

Figure 2.2. Distribution of maximum absolute scalp STA amplitudes by group. For each of the 42 groups of hippocampal discharges, the greatest absolute amplitude seen across all channels in the scalp signal STA is plotted. Symbol shapes indicate groups included or excluded from the analysis shown in Figure 2.4C.

2.3.2 Characterization of scalp waveforms based on temporal lag

Next, we asked if the observed scalp EEG patterns were consistent with the volume conduction of hippocampal discharges. Volume conduction occurs at the speed of light, so a finding of no lag between a scalp signal and an associated hippocampal discharge would be consistent with volume conduction. Temporal lag was determined from the cross-correlogram between each scalp EEG channel STA and the depth electrode channel STA with the greatest amplitude (Fig. 2.1, 2.3). For example, in Group 1, cross-correlation of the STA of scalp channel

F9 and the STA of channel RHD4 yielded a maximum correlation coefficient of 0.93 at a lag time of -3ms, where a negative value implies the scalp signal leads the hippocampal signal (Fig. 2.3A).

Although volume conduction theoretically occurs with zero lag, noise in real recordings may cause the peak in cross-correlations of synchronous signals to deviate from zero. To determine the range of measured lag times that were sufficiently small to be interpreted as zero, we conducted a Monte Carlo simulation of lag times resulting from cross-correlation of two identical signals corrupted by varying levels of noise (Methods). The black curve in Figure 2.3B shows the result of this simulation and represents the 99% confidence interval (CI) for the distribution of lag times across the range of signal to noise ratios (SNR). For example, for the cross-correlation of an 8dB scalp signal with a 25dB hippocampal signal, the 99% CI of lag times was ±4.8ms. As expected, signals with low SNR have a larger spread of lag times than signals with high SNR. This non-zero threshold for lag times does allow for the possibility of physiological propagation in signals categorized as volume conduction. Consequently, we interpret small lag times as not proof of volume conduction, but rather a characteristic that is consistent with volume conduction.

The scatter plot in Figure 2.3B shows the lag times of all scalp channel STAs for Patient 1. Points that fall below the 99% CI line have a lag sufficiently close to zero to be consistent with volume conduction. For points that fall above the simulation curve, scenarios involving secondary sources likely contribute to the scalp signal. Of the 5 groups identified, Group 4 had the smallest amplitude signals in both the hippocampal and scalp channels. The small and sparse nature of the scalp signals seen in Group 4 reduces their interpretability, and therefore we highlight here the results of other groups with more robust and distinctive characteristics. Of the 20 channels with significant scalp signals in Group 2, 16 channels had lag times below the 99% CI while 4 channels had lag times above the 99% CI. This observation suggests that the scalp correlates seen for Group 2 are more consistent with volume conduction. In contrast, Group 5 had 21 channels with significant scalp STA signals, 17 of which had lag times greater than the 99% CI, suggesting that the scalp correlates for Group 5 are more consistent with a propagated or secondary source.

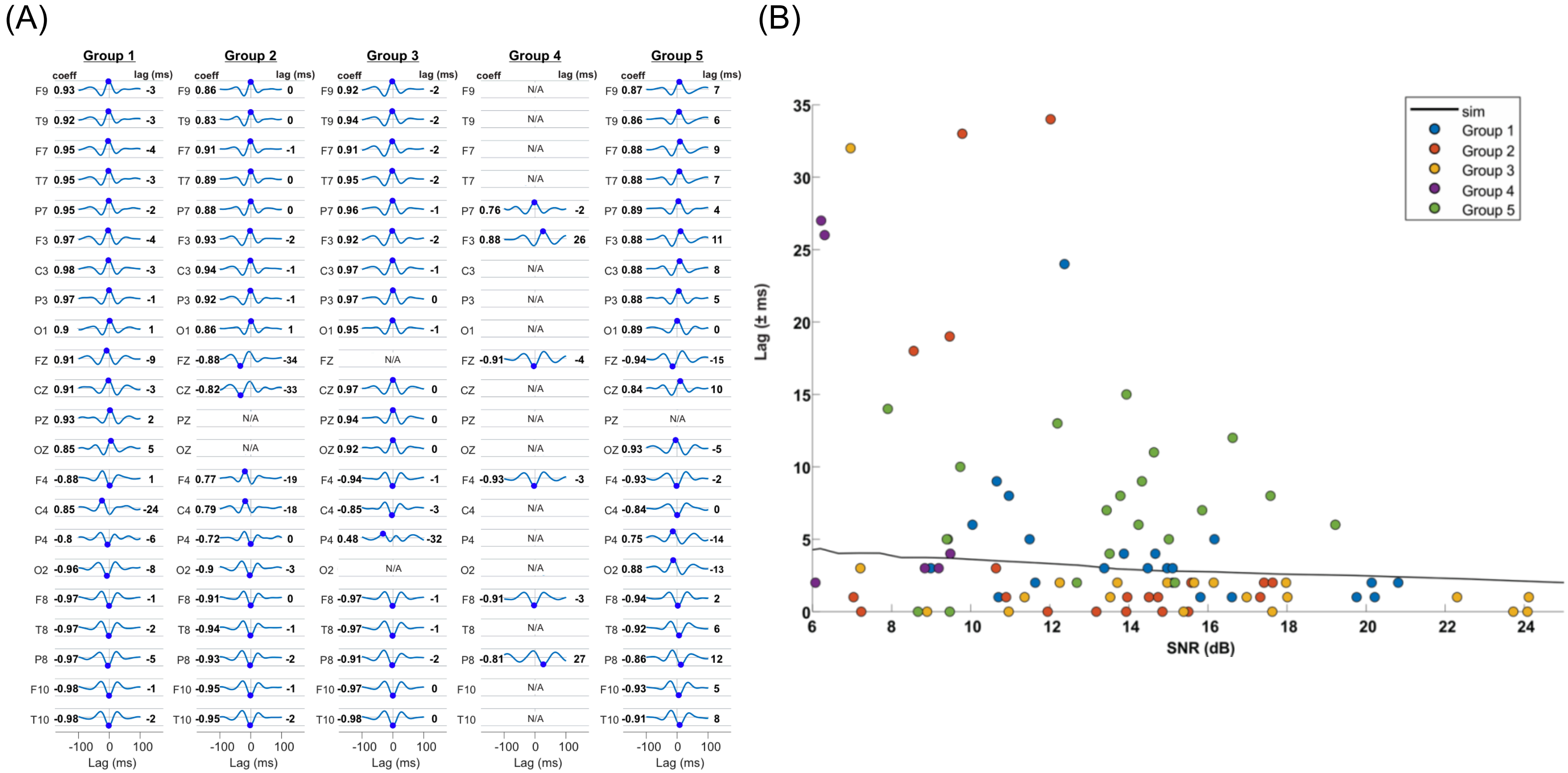

Figure 2.3. Cross-correlation analysis of intracranial and scalp EEG STAs of hippocampal discharges.
(A) Cross-correlograms for Patient 1. Cross-correlation was determined between the largest hippocampal signal in Figure 2.1A and its associated scalp waveforms depicted in Figure 2.1B. Correlation values are scaled between ±1 (grey horizontal lines) and the lags are computed between ±100ms. For each scalp electrode, the greatest absolute correlation coefficient and its lag (ms) are written on the left and right, respectively, for each waveform. The greatest absolute correlation coefficient for each correlogram is indicated by the blue dot. **(B)** Determining scalp channels with lags consistent with volume conduction of a hippocampal source. Scatterplot of lags plotted versus the SNR of the five groups of Patient 1. The solid line indicates the simulated 99% confidence for zero lag corrupted by noise. Note that for groups 2 and 3 most channels are below the line while for group 5 most are situated above the line.

2.3.3 Topographic analysis of scalp STAs

In addition to temporal correlation, we investigated the spatiotemporal development of scalp discharges. We hypothesized that scalp topographies that reflect volume conduction from a single, deep source would exhibit a relatively stationary dipole, while sources that propagate to and engage other brain areas would show a more dynamic evolution of scalp potentials. The scalp STAs for each group were used to generate topographic maps of scalp potentials at different time points. The topographies for the five groups from Patient 1 are shown in Figure 2.4A. Qualitatively, some of the discharges show fields that are largely stationary except for an abrupt flip in polarity (Fig. 2.4A, Group 2), while others show a more dynamic, rotational pattern (Fig. 2.4A, Group 5). To quantify this observation, we used the standard deviation (SD) in the field dipole angle as a metric to determine how the topography of each discharge evolves over time (Fig. 2.4B). Of the 42 groups, 24 met the criteria for inclusion in this analysis (Fig. 2.2). A small angle-SD implied a relatively stationary dipole, while a high angle variance implied a rotating dipole. We then asked if the SD of this angle correlated with the percentage of scalp channels with no lag in that group (Fig. 2.4C). The groups dominated by zero lag times showed smaller SD (i.e., more stationary topographies) than groups with predominantly non-zero lag times ($r = -0.61$; $p = 0.001$). This supports the hypothesis that scalp manifestations consistent with volume conduction are more stationary than discharges consistent with other mechanisms such as neuronal propagation.

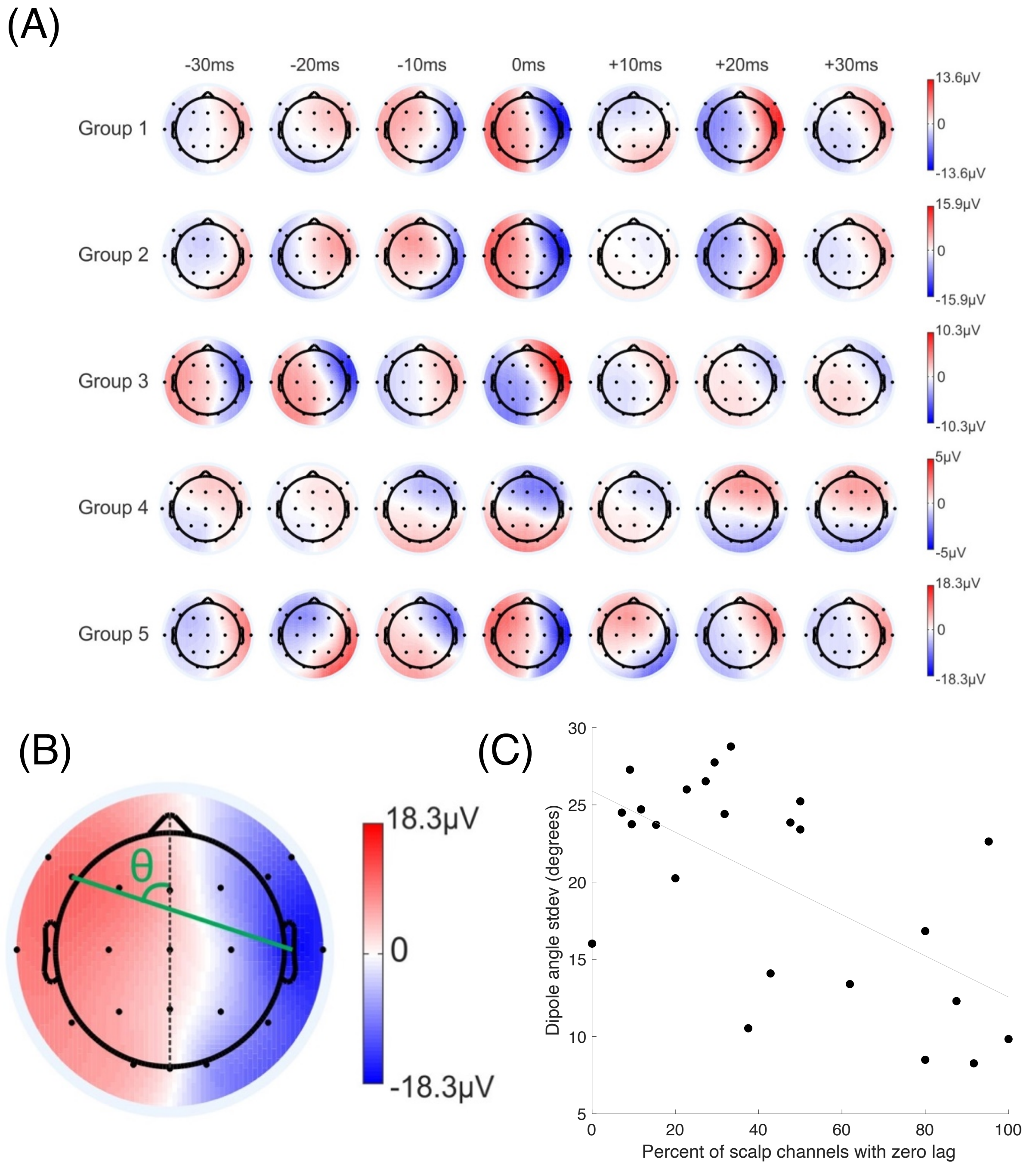

Figure 2.4. Topographic analysis of hippocampal discharge-related scalp EEG signals.
(A) Topography of the five groups of discharges in Patient 1. The zero value of the time scale is aligned with the maximum amplitude of the discharge. **(B)** To estimate the angle of the dipole underlying the topographic field, a line was drawn between the electrodes with the maximum and minimum value (green). The zero–degree axis was defined as the inion-nasion line (dotted black). **(C)** For all patients and groups: variance of topography plotted versus the % of channels with zero lag. The line is the linear regression (n = 24; r = -0.62, p = 0.001).

2.3.4 Theoretical estimation of scalp signal amplitudes

The scalp signals observed in our study were on the order of 10μV (Fig. 2.1), which are consistent with other studies (Koessler et al., 2015) . We wished to estimate whether this amplitude was plausible from a physics viewpoint. To probe the underlying physics associated with our volume conduction hypothesis, we estimated the theoretical order of magnitude for local and scalp measurements of a hippocampal source using a four-shell model of the head (Fig. 2.5) (Methods). The results of this model showed that intracranial measurements of the hippocampal source range from 0.5mV to 30mV as the electrode distance from the hippocampus decreases from 6cm. In our analysis of the theoretical clinical scalp EEG, we observed a range between ±25μV, depending on the location of the scalp electrode (Fig. 2.5B). The ranges for these intracranial and scalp values agree well with the findings in our patient data shown in Figure 2.1.

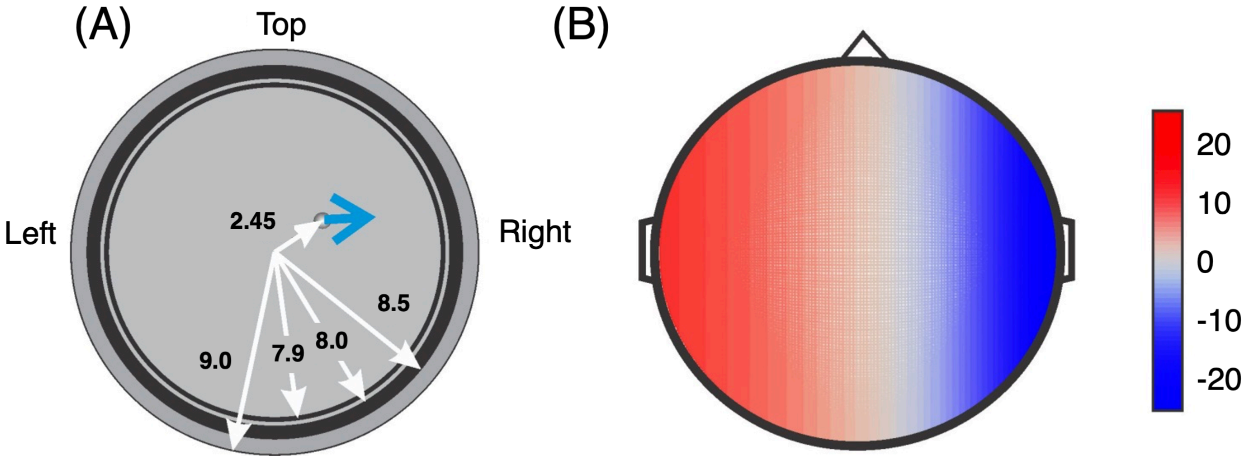

Figure 2.5. Estimation of the effect of a hippocampal source on the scalp potential. **(A)** A four-shell spherical model representing the brain, cerebrospinal fluid, skull, and skin. The hippocampal dipole is indicated by the blue arrow. Distances are expressed in cm. **(B)** Predicted topographic map at the scale generated by the field evolved by the dipole in (A). Color scale is in μV.

2.4 Discussion

In this study, we present evidence that scalp waveforms associated with hippocampal interictal discharges have varying topographic morphology. Furthermore, whether the scalp waveform was consistent with volume conduction of a hippocampus-limited discharge could be determined by comparing the lag time between the scalp and hippocampal signals. While the exact source of any signal cannot be definitively proven without sampling from all brain areas simultaneously, the observations in our study suggest that the combination of cross-correlation lag time analysis and scalp topographic analysis can be used to group and categorize hippocampal spikes into those consistent with physiological propagation and those consistent with volume conduction.

Two types of scalp topography were identified—static and dynamic (Fig. 2.4). In the static case, electrical fields were consistent with a largely stationary dipole with an abrupt left-right flip during the course of the discharge (Fig. 2.4A, Groups 1 & 2). These characteristics, along with the observations that waveforms were present bilaterally with higher amplitudes on the side ipsilateral to the hippocampal spike and with inverted polarity on the contralateral scalp electrodes, point to a lateralized, single, deep source. Additionally, the near-simultaneous timing of the scalp and hippocampal waveforms and their high correlations are consistent with a signal that travels from the hippocampus to the scalp via volume conduction, an electromagnetic process that occurs with virtually zero delay. In contrast, scalp waveforms that occur with significant lag from the hippocampal discharge showed more complex, rotational dynamics, suggestive of a signal that either travels to or engages other cortical areas using a more time-consuming mechanism such as neuronal propagation and synaptic transmission (Fig. 2.4A, Groups 3 & 5). By using only hippocampal depth and scalp electrodes, it is not possible to ascertain the exact origin of physiologically propagated signals. This limitation may be addressed in future studies that incorporate recordings from other cortical areas simultaneously.

Other groups have suggested that differences in topographic evolution can be used to differentiate between benign and pathological scalp small sharp spikes (Wennberg et al., 2018). Both the static and dynamic waveforms observed in our study show a horizontal dipole at the time of the spike, consistent with what has been described as benign epileptiform transients of sleep (BETS) (Wennberg et al., 2018). However, BETS showed a 30° rotational component, suggesting that our dynamic group aligns more with what has been described as BETS while our static group may be more aligned with pathological waveforms (Issa, Lee, et al., 2018). To differentiate between benign versus pathological waveforms, more comprehensive prospective studies using both neurotypical and epileptic patients will be required.

In mesial temporal lobe epilepsy, epileptiform activity can be limited to deep structures such as the hippocampus or involve larger networks that include neocortical regions. Classical epileptiform discharges such as spikes and sharp waves are frequently observed on scalp EEG when neocortical regions are involved (Koessler et al., 2015; Merlet & Gotman, 1999). When epileptiform activity is restricted to regions around the hippocampus, however, scalp waveforms are not readily apparent (Wennberg et al., 2011), and only small sharp spikes have been implicated as scalp EEG markers of hippocampal discharges (Issa, Wu, et al., 2018). While the natural history of temporal lobe epilepsy is incompletely defined (Berg, 2008; Hesdorffer et al., 2016; Issa, Sedler, et al., 2018; Shukla & Prasad, 2012), one line of thought posits that epileptogenic activity is restricted to the hippocampus in the early phases of MTLE with recruitment of neocortex occurring as the disease progresses (Morrell, 1985; Morrell et al., 1989; Wennberg et al., 1997). Because engagement of larger networks may be associated with poorer surgical outcomes with targeted resections (Sinha et al., 2017), the ability to detect and differentiate early hippocampal discharges with or without neocortical involvement could lead to earlier diagnosis, prevent misdiagnoses, and improve patient outcomes.

For clinical purposes, hippocampal discharges in early MTLE should ideally be identifiable without the need for invasive monitoring. Scalp markers are likely to be low in sensitivity for the detection of individual hippocampal discharges since we are relying on greatly attenuated hippocampal signals to break through the relatively high noise levels of the scalp EEG. Chen et al. (2020) found that in patients evaluated in an epilepsy monitoring unit, small sharp spikes on scalp EEG had an odds ratio of 9.1 for epilepsy, but only a sensitivity of ~19%. In our own dataset, approximately 15% of all hippocampal spikes were associated with a visible waveform on the scalp, results that are within range with the detection rate of 22% found by down-sampling dense array scalp EEG signals (Yamazaki et al., 2012). Although sensitivity for individual hippocampal discharges is low, small sharp spikes may be visible in up to 50% of patients with hippocampal discharges (Issa, Wu, et al., 2018). If indeed some of these waveforms are a result of volume conduction of hippocampal discharges, higher rates of detection may be possible for patients with smaller heads and thinner skulls, meaning that this may be a particularly useful marker in pediatric populations. For example, children with febrile status epilepticus have been shown to be at higher risk for developing TLE (Lewis et al., 2014), and small sharp spikes might be an early marker for such pathology.

Previous studies concluding that hippocampal discharges are undetectable on the scalp due to signal attenuation have largely relied on signal-to-noise ratio (SNR) calculations. By definition, low amplitude signals embedded in high amplitude noise yield SNR values < 1. These signals, however, may still be visible if they have features distinct from background signals. SNR calculations find signals that differ from background by their amplitude and power. Signals captured in clinical recordings, however, have other attributes that can be used to identify low amplitude signals:

(1) Clinical recordings utilize multichannel systems. A low amplitude signal that is undetectable in a single channel may become readily visible if it is synchronously observed in several channels. The ability to identify low amplitude signals by extracting information

across multiple channels may be uniquely advantageous in the measurement of deep sources, since these signals are more likely to be captured by multiple electrodes.

(2) Differences in frequency composition can be used to identify signals. Low amplitude signals embedded in high amplitude noise may be identified if their frequency composition is distinct from noise. For example, a very small discharge with a fundamental frequency of 20Hz may be highly noticeable if the background noise and rhythms are composed of lower frequencies.

2.5 Methods[2]

2.5.1 Patients and data acquisition

Data were collected from 17 patients (10 females; Table 2.1) undergoing phase II monitoring for medically intractable, right temporal lobe epilepsy between 2015 and 2017 at the University of Chicago Adult Epilepsy Center. Written informed consent was provided through a process approved by the University of Chicago Institutional Review Board.

Intracranial recordings were collected using depth electrodes placed into the right hippocampus. All patients were implanted with a 12-channel depth electrode placed along the length of the right hippocampus, with contact #1 (RHD1) being most anterior and contact #12 (RHD12) being most posterior. Although other intracranial electrodes were placed in various locations for all patients, only the RHD intracranial electrodes and scalp EEG electrodes were analyzed for this study. Contact locations were confirmed with post-implantation CT scans.

Scalp EEG data collected from the following 22 electrodes (named according to the international 10-10 arrangement) were used for analysis: F9, T9, F7, T7, P7, F3, C3, P3, O1, Fz, Cz, Pz, Oz, F4, C4, P4, O2, F8, T8, P8, F10, T10. Data from Fp1, Fp2, M1, and M2 were recorded but

---

[2] Custom scripts used to generate the results presented in this chapter can be found at https://github.com/sominlee14/hippocampal_ied (Appendix).

not included in this analysis because they typically contained large non-cortical artifacts. All hippocampal depth and scalp EEG signals were collected using the XLTEK system (Natus, Pleasanton, CA, USA). Signals were digitized at 1024 samples/s and referenced to the FCz electrode. The raw broadband data (0.1-344 Hz) were stored for subsequent analysis.

Table 2.1. Summary of demographics and diagnoses for 16 patients.
MTLE = mesial temporal lobe epilepsy

Patient #	Age	Gender	Diagnosis
1	51	Female	Right MTLE
2	21	Male	Bilateral MTLE
3	33	Male	Bilateral MTLE
4	51	Male	Bilateral MTLE
5	33	Female	Right MTLE
6	21	Male	Bilateral MTLE
7	22	Female	Right MTLE
8	22	Female	Bilateral MTLE
9	24	Male	Right MTLE
10	40	Female	Right MTLE
11	19	Female	Right MTLE
12	47	Female	Right MTLE
13	26	Male	Right MTLE
14	43	Male	Right MTLE
15	58	Female	Right MTLE
16	44	Female	Bilateral MTLE

2.5.2 Data analysis pipeline

For each patient, a two-hour EEG segment recorded during drowsiness and sleep was analyzed. A custom C^{++} routine was used to convert raw data into Matlab files. All other analyses and statistics were performed in Matlab (Matlab, Natick, MA, USA). The relationship between intracranial and extracranial signals was analyzed using the following pipeline:

1. Automated detection of intracranially recorded hippocampal discharges
2. Grouping of similarly shaped hippocampal discharges using connected components analysis
3. Calculation of spike-triggered averages (STAs) of intracranial and scalp EEG signals
4. Cross-correlation of intracranial and scalp EEG signals
5. Topographic analysis of scalp signals

Unless otherwise noted, the average reference montage was used, in which all signals were referenced to the average of the scalp EEG channels. All analyses were performed separately for each patient. Specifics of these five steps are described below.

(1) Detection of hippocampal discharges

Signals from the 12 channels on the right hippocampal depth (RHD) electrode were used to identify epochs containing interictal discharges. Because the detection method only utilized intracranial channels, the FCz common reference montage was used. EEG signals were digitally filtered using a zero-phase, 2nd order 10-50Hz Butterworth bandpass filter. The signals from the 12 RHD channels were then averaged, and peak detection was applied. Peaks were defined as points having an absolute amplitude >5 standard deviations from the signal mean and that were a local minimum or maximum in a 1 second window. This detection method was independently validated by visual inspection by an epileptologist.

(2) Grouping of hippocampal discharges

Hippocampal discharges in a given subject were grouped by waveform using connected component analysis (Hopcroft & Tarjan, 1973). A 500ms epoch centered on each peak was used for classification. For each epoch, signals from the 12 RHD channels were concatenated, creating a 6000 ms-long vector. A correlation coefficient was then calculated between pairs of vectors, resulting in an n x n correlation matrix where n was the number of hippocampal discharges (Fig. 2.6A). Using a correlation coefficient threshold, this correlation matrix was converted into a binary matrix by replacing coefficients above or below the threshold with 1's and 0's, respectively (Fig. 2.6B). This binary matrix was then converted into an undirected graph in which discharges were represented by nodes connected by edges specified by 1's in the matrix. The connected components of this graph were extracted using the Matlab function *conncomp*, which assigns two nodes to the same component if they are connected by an edge. A group was defined as the set of discharges belonging to the same connected component (Fig. 2.6C).

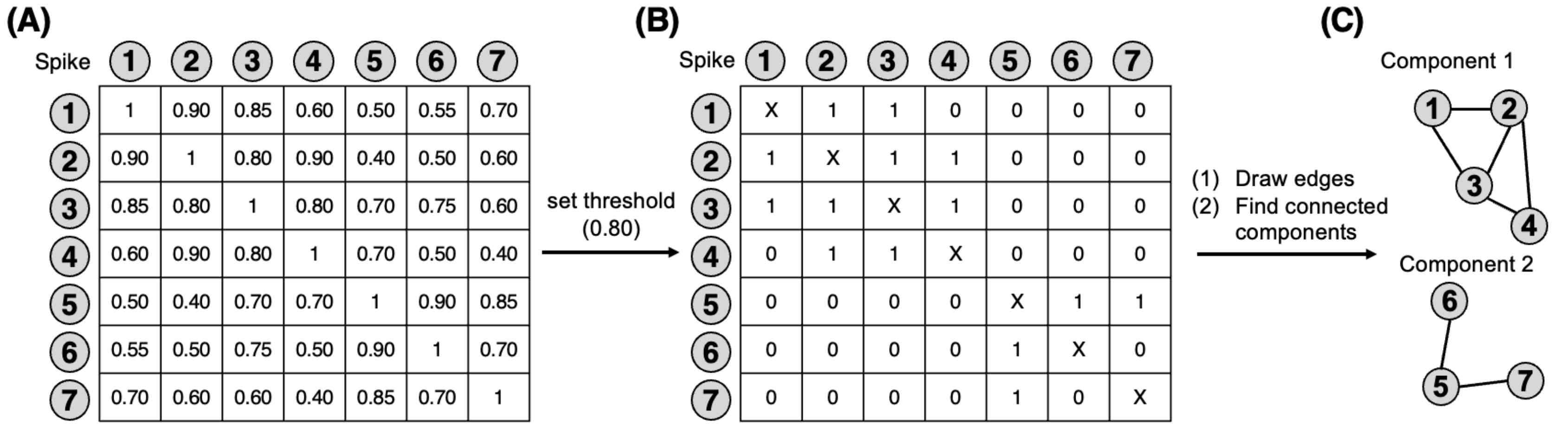

Spike	①	②	③	④	⑤	⑥	⑦
①	1	0.90	0.85	0.60	0.50	0.55	0.70
②	0.90	1	0.80	0.90	0.40	0.50	0.60
③	0.85	0.80	1	0.80	0.70	0.75	0.60
④	0.60	0.90	0.80	1	0.70	0.50	0.40
⑤	0.50	0.40	0.70	0.70	1	0.90	0.85
⑥	0.55	0.50	0.75	0.50	0.90	1	0.70
⑦	0.70	0.60	0.60	0.40	0.85	0.70	1

Spike	①	②	③	④	⑤	⑥	⑦
①	X	1	1	0	0	0	0
②	1	X	1	1	0	0	0
③	1	1	X	1	0	0	0
④	0	1	1	X	0	0	0
⑤	0	0	0	0	X	1	1
⑥	0	0	0	0	1	X	0
⑦	0	0	0	0	1	0	X

Figure 2.6. Schematic of finding connected components using correlations between spikes.
(A) Example correlation matrix of spike comparisons. **(B)** Binary matrix created from setting a threshold correlation coefficient. **(C)** Connected components generated from using 1's in the binary matrix as edges. In this dummy example of seven spikes, spikes 1-4 are in one group, and spikes 5-7 are in another group.

To determine the appropriate threshold correlation coefficient for the grouping procedure, discharges were preliminarily grouped using threshold values ranging from 0.5 to 1.0 in 0.01 increments. The threshold value that maximized the number of large groups (defined as ≥20 discharges/group) was used in the final analysis (Fig. 2.7). This threshold value was determined for each patient separately.

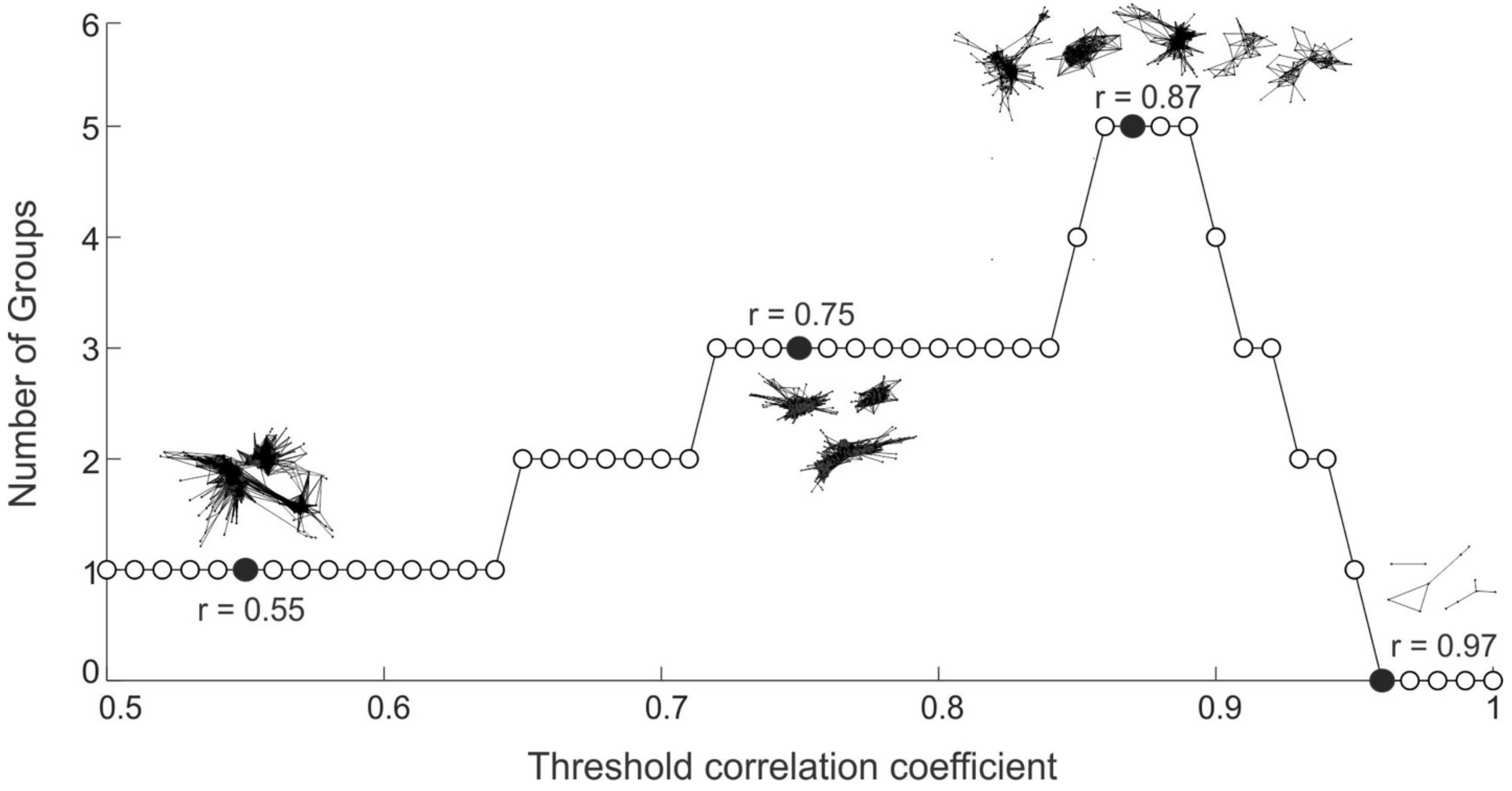

Figure 2.7. Determination of threshold for connected components analysis to group hippocampal peaks detected in Patient 1.

Connected components analysis as described in the text was performed with a range of correlation coefficients to determine the appropriate threshold value. If the threshold is too low (r = 0.55), the analysis yields one large group. As the threshold is increased (r = 0.75), this large group breaks apart into smaller groups. The threshold that yields the highest number of large groups (r = 0.87) was used for the final analysis. In cases where a range of coefficients met this criterion, the median value was chosen. If the threshold is too high (r = 0.97), peaks are sorted into very small groups, none of which contain more than 20 peaks.

(3) Calculation of spike-triggered averages for EEG signals

For each group of discharges, spike-triggered averages (STAs) for RHD and scalp EEG signals were calculated. STAs were calculated by averaging the signals from all discharges in a given group, using the peaks detected in the RHD signals as triggers. Noise levels were estimated using 250ms flanks before and after the 500ms STA epoch. The signal-to-noise ratio (SNR) in dB was defined as:

$$SNR = 20log_{10}\left(\frac{RMS_{signal}}{RMS_{noise}}\right) \tag{2.1}$$

where $\mathrm{RMS}_{\mathrm{signal}}$ is the root mean square (RMS) amplitude of the STA and $\mathrm{RMS}_{\mathrm{noise}}$ is the RMS amplitude of the 250ms flanks around the STA. Scalp STAs with an SNR≥6dB were used for subsequent analyses.

(4) Cross-correlation of intracranial and scalp EEG signals

We determined the temporal relationship between the hippocampal discharge measured by the intracranial channels and the voltage changes measured by the scalp electrodes. Within each group of hippocampal discharges, we computed the cross-correlation R_{xy} between the intracranial channel STA with the highest amplitude (x) and scalp STAs at each electrode (y) using:

$$R_{xy}[k] = \sum_{m=1}^{N} x[m]y[m-k] \tag{2.2}$$

in which m is the index of the sampled data point, N is the total number of samples in the epoch, and k is the lag time. This procedure resulted in 22 cross-correlograms per group. For each cross-correlogram, the lag time at which the greatest absolute correlation occurred was determined.

Although volume conduction theoretically occurs with zero lag, noise in real recordings may cause the peak in cross-correlations of synchronous signals to deviate from zero. To determine what range of lag times is sufficiently small to be interpreted as zero, we conducted the following Monte Carlo simulation. We generated two 500ms epochs containing identical 20Hz sine waves: one epoch represented the intracranial hippocampal discharge and the other represented the scalp EEG signal. After various levels of random Gaussian noise were added to each epoch, the two epochs were cross-correlated, and the lag time at which the maximum correlation occurred was determined. The SNR for the epoch representing the intracranial signal was fixed at 25dB (a level based on our measurements), while a range of 6-25dB was used for the epoch representing the scalp signal. This procedure was repeated 1000 times for each noise level to generate a distribution of maximum correlation lag times for a range of SNRs. The 99% CI for this distribution was determined, and lag times within this interval were considered to be sufficiently small to be interpreted as having no delay.

(5) Topographic analysis of scalp signals

For each discharge group, the scalp STAs were used to create field potential maps using EEGLAB software (Delorme & Makeig, 2004), using the *topoplot* function with default electrode coordinates. Topographic maps were generated for each time point across the 500ms STA epoch. The topographic maps reflect 2-dimensional projections of 3-dimensional coordinates of the scalp electrodes.

The dynamics of the scalp topography were quantified by the standard deviation (SD) in the direction of the scalp field dipole during the course of the 500ms discharge epoch. For each time point, the direction of the scalp field dipole was estimated by the angle between the inion-nasion line and the line connecting the electrodes with the minimum and maximum amplitude (Fig. 2.4B). The dipole angle was calculated at time points with a dipole amplitude ≥5 standard deviations from the mean dipole amplitude over the 500ms epoch. To obtain reliable SD estimates, we only included groups that had scalp EEG SNR ≥6dB in at least 5 channels and waveforms with a minimum duration of 20ms.

2.5.3 Volume conduction estimation

We employed a four-shell, spherical model representing brain tissue, CSF, skull, and skin. The radii of these four layers were set at 7.9, 8.0, 8.5, and 9.0cm, and the location of the hippocampal source at 2.45cm (Nunez et al., 2006) (Fig. 2.5A). We set the soft tissue (brain tissue and skin) conductivity at 0.33 $(\Omega.\mathrm{m})^{-1}$, the soft tissue/skull conductivity ratio at 20, and the CSF/soft tissue ratio of 5 (Nunez et al., 2006; Zhang et al., 2006). During the peak of the interictal hippocampal discharge, we assumed that 10^5 neurons are active, each with 2000 active synapses that each generates 1pA. At a 1mm distance between the cellular sink and source, this translates into a hippocampal dipole moment of 2.10^{-7} Am, which is a value close to the 10^{-7} Am used in Naess et al. (2017). We used equations (5), (6), (17), and (18) from Naess et al. (2017) to compute the amplitude of scalp and depth signals. Note that the parameters in these equations are corrected versions from the ones in Appendix G in Nunez et al. (2006).

CHAPTER 3

Digital reconstruction of infraslow activity in ictal recordings[1]

3.1 Summary

Infraslow activity (ISA) is a biomarker that has recently become of interest in the characterization of seizure recordings. Recent data from a small number of studies have suggested that the epileptogenic zone may be identified by the presence of ISA. Investigation of low frequency activity in clinical seizure recordings, however, has been hampered by technical limitations. EEG systems necessarily include a high-pass filter early in the measurement chain to remove large artifactual drifts that can saturate recording elements such as the amplifier. This filter, unfortunately, attenuates legitimately seizure-related low frequencies, making ISA difficult to study in clinical EEG recordings. In this study, we present a deconvolution-based digital inverse filter that allows recovery of attenuated low frequency activity in intracranial recordings of temporal lobe epilepsy patients. First, we show that the unit impulse response (UIR) of an EEG system can be characterized by differentiation of the system's step response. As proof of method, we present several examples that show that the low frequency component of a high-pass filtered signal can be restored by deconvolution with the UIR. We then demonstrate that this method can be applied to biologically relevant signals including clinical EEG recordings obtained from seizure patients. Finally, we discuss how this method can be applied to study ISA to identify and assess the seizure onset zone.

3.2 Introduction

Epilepsy is one of the most prevalent neurological conditions and affects over three million people in the United States (Zack & Kobau, 2017). A third of patients with epilepsy continue to

---

[1] Results presented in this chapter are in revision at *Scientific Reports*.

experience seizures despite medication treatment (Kwan & Brodie, 2000). Although many of these patients pursue surgical options, 40-70% of surgical patients continue having seizures after resective surgery (Téllez-Zenteno et al., 2005). Surgical intervention is thought to fail in these cases due to the incomplete removal of the culprit brain tissue, a putative and theoretical area known as the epileptogenic zone (EZ). Because the EZ is an area that can only be defined post-surgically, the seizure onset zone (SOZ) is used as a proxy for the EZ during surgical planning (Jobst et al., 2020). The limited efficacy of surgical interventions suggests that our ability to identify the SOZ/EZ is insufficient. Thus, identifying features that are unique to the SOZ/EZ has great potential for improving surgical outcomes.

Low frequency ictal activity is a biomarker that has recently become of interest in the characterization of seizure recordings. Recent data from a number of studies suggest that the EZ may be identified by the presence of very low frequency oscillations (Ikeda et al., 2020; Modur, 2014; Wu et al., 2014) (for a review, see Lee et al. (2020)). Termed "infraslow activity" (ISA) or direct current (DC) shifts in the literature, this low frequency band is typically defined as activity below 0.1 or 0.5Hz. This frequency band is much slower than the 1-70Hz band at which clinical EEGs are typically interpreted. The study of low frequency activity in seizure recordings, however, has been hampered by technical limitations. EEG systems necessarily include a high-pass filter early in the measurement chain to remove large artifactual drifts that can saturate recording elements such as the amplifier. This filter unfortunately attenuates legitimately seizure-related low frequencies, making ISA difficult to study in clinical EEG recordings. Although a few studies have utilized DC amplifiers to try to bypass this issue (Kim et al., 2009; Miller et al., 2007; Vanhatalo et al., 2003; Vanhatalo et al., 2004), DC amplifiers are not immune to saturation issues (Fig. 3.1). Furthermore, standard clinical EEG equipment does not utilize DC amplifiers, making observing ISA directly in clinical recordings difficult. Consequently, development of a method to evaluate ISA in recordings obtained with alternating-current (AC) amplifiers is desirable.

In this study, we present a novel approach to digitally reconstruct attenuated low frequency activity in clinical EEG recordings using a deconvolution-based inverse filter. First, we show that a clinical EEG recording system's unit impulse response (UIR) may be derived by differentiation of the system's step response. We then use this UIR to deconvolve a variety of synthetic signals to demonstrate successful restoration of attenuated low frequencies. We then show that this method is stable when applied to clinical intracranial recordings obtained from temporal lobe epilepsy patients. Finally, we discuss how this method may be applied to study ISA as it relates to the identification and assessment of the SOZ.

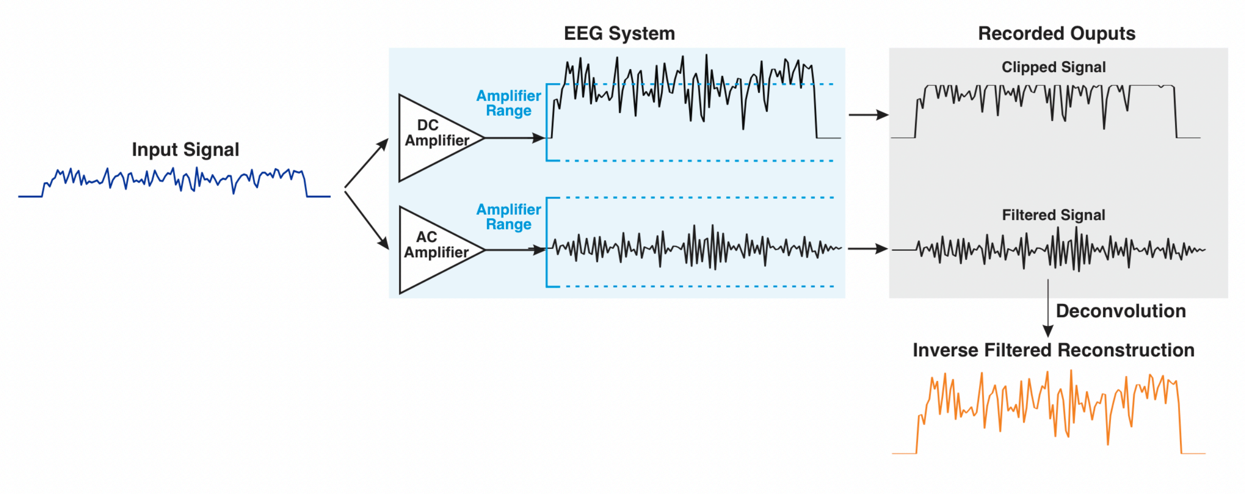

Figure 3.1. Limitations in using direct-current (DC) and alternating-current (AC) amplifiers in recording low frequency activity.
Although the use of a DC amplifier allows preservation of low frequency components, signals can become clipped if the large amplitude slow activity exceeds the range of the amplifier (top chain). AC amplifiers include a high-pass filter that allows signals to comfortably stay within the amplifier range, but low frequency activity is greatly attenuated (lower chain). Using a deconvolution-based inverse filter algorithm to digitally restore low frequency activity in signals measured with an AC amplifier is one solution to this issue (bottom, orange trace).

3.3 Results

In linear time invariant (LTI) systems, the effects of recording elements such as filters on signals may be mathematically described as a convolution of the input signal with the system's characteristic unit impulse response (UIR) (Fig. 3.2). Inversely, the input of this system can be found by deconvolution of the output signal with the UIR (Fig. 3.2). If the LTI element in question is a filter, the deconvolution operation may be thought of as an "inverse filter" that allows for recovery of frequencies attenuated by the filter. While this concept is mathematically straightforward, the challenge of applying this method to real-world signals lies in the ability to accurately characterize the UIR of the recording system.

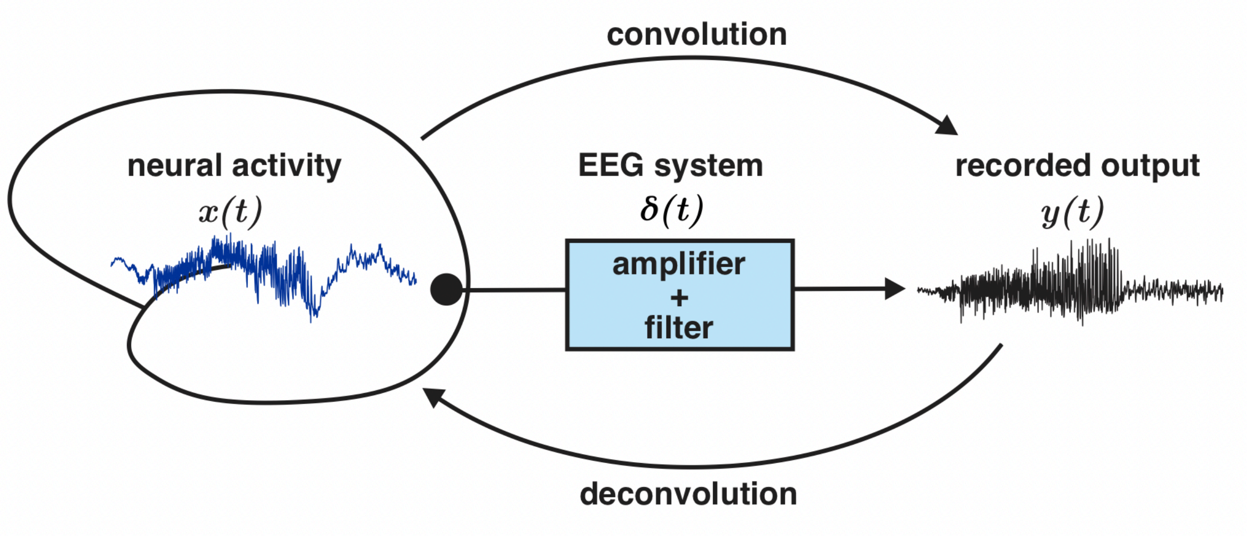

Figure 3.2. Elements of a linear time invariant (LTI) system may be described by convolution and deconvolution operations.
In a LTI system, output function $y(t)$ may be described by a convolution of the input signal $x(t)$ with the system's unit impulse response $\delta(t)$. Inversely, the input signal may be obtained by deconvolving $y(t)$ with $\delta(t)$. The unit impulse response fully characterizes the LTI system in the time domain. In this schematic, the LTI system is the EEG recording machinery that includes elements such as amplifiers and high-pass filters.

3.3.1 Characterization of the unit impulse response of a clinical EEG system

Mathematically, the UIR of a system is the derivative of the system's step response (Van Drongelen, 2018). To characterize the UIR of a clinical EEG unit (Natus XLTEK Brain monitor with Connex headbox), we used a digital/analog (D/A) converter to input a synthetically generated step function (Fig. 3.3A) (Methods). The output measured by the EEG system (i.e., the system's step response) was fitted with a 9th order polynomial (Fig. 3.3B, C). Taking the derivative of this polynomial approximation resulted in the putative characteristic UIR of the recording system (Fig. 3.3D). The accuracy of this UIR was verified by deconvolving the recorded output of a test function with known low frequency activity. The test function was a series of two step functions (Fig. 3.4A). Deconvolution of the recorded output of these step functions (Fig. 3.4B) with the UIR resulted in a reconstruction that resembled the input (Fig. 3.4C). Notably, the flat feature of the step functions was restored, confirming that this method is appropriate for reconstructing DC shifts. The deconvolution operation was also robust to noise, as the square shape of the reconstruction was preserved even with the addition of high levels of normally distributed random noise (Fig. 3.4D-F).

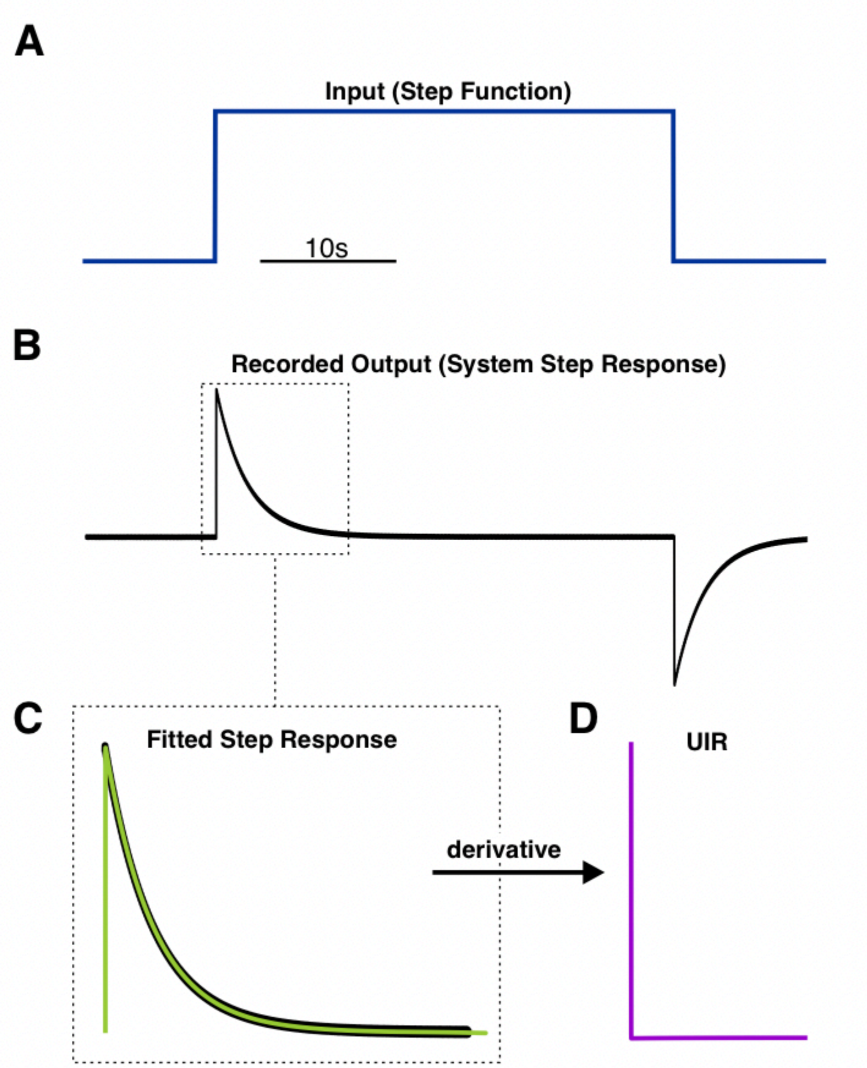

Figure 3.3. Determination of an EEG system's unit impulse response (UIR) by measuring the system's step response.

A synthetically generated step function was used as input into the EEG system **(A)**. The measured output was the system's step response **(B)**. This step response was fitted with a 9th order polynomial (light green trace) **(C)**. Taking the derivative of this polynomial function resulted in the system's UIR **(D)**.

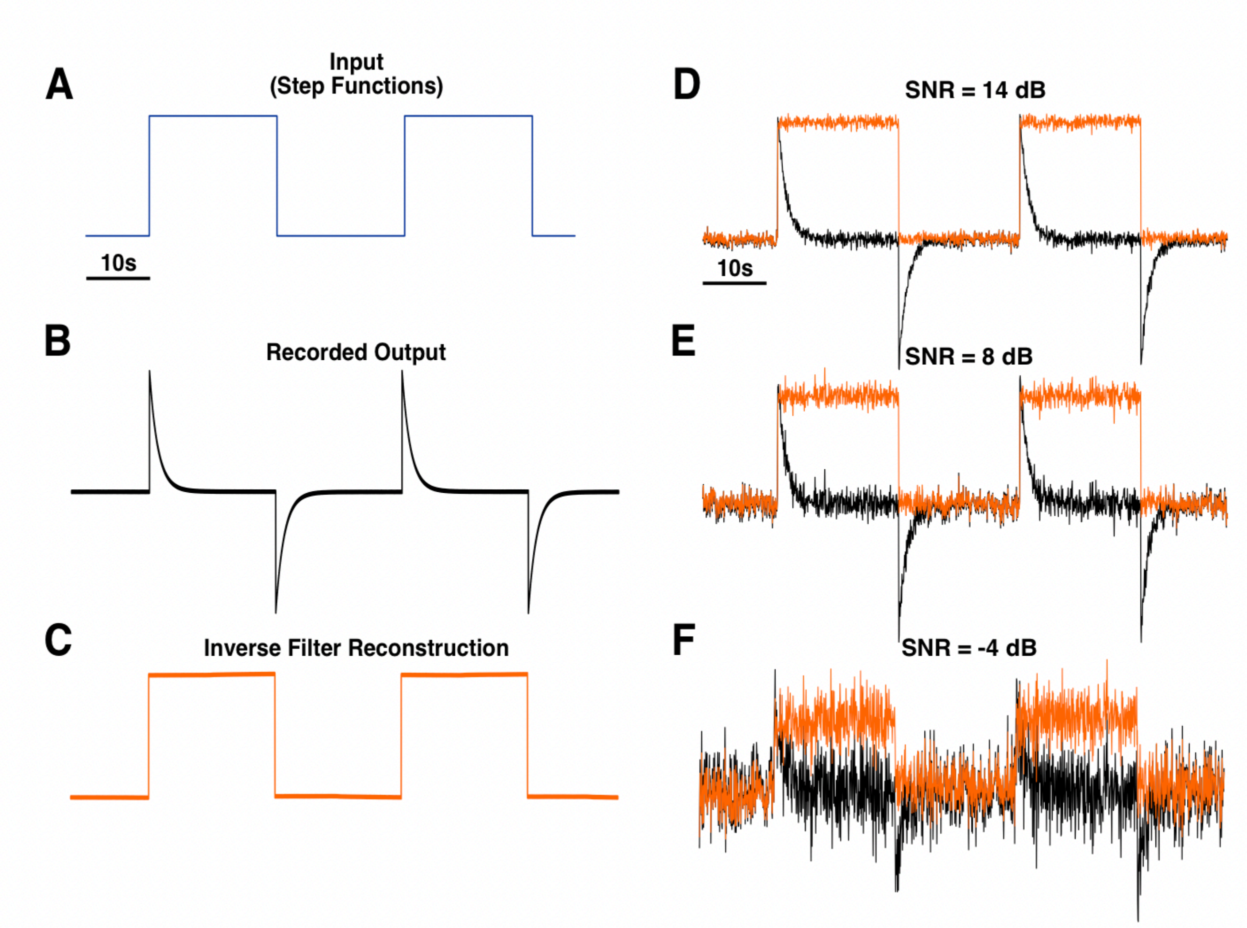

Figure 3.4. Application of deconvolution-based inverse filter to step functions. A series of two step functions was used as a test input signal **(A)**. The EEG system's recorded output **(B)** was deconvolved by the unit impulse response (UIR) depicted in Figure 2D, which resulted in the reconstruction of the original step function **(C)**. This method was able to reconstruct the general step function shape with high fidelity even with the addition of varying levels of normally distributed random noise **(D, E, F)**. In panels D, E, and F, the black traces show the recorded output with added noise, and the orange traces show the inverse filtered reconstructions. SNR = signal-to-noise ratio.

3.3.2 Validation of deconvolution-based inverse filter using synthetic signals

We then tested our inverse filter procedure on two different types of synthetic signals. All inputs were generated digitally in MATLAB and converted to an analog signal using a digital/analog converter to be used as inputs into the EEG system (Methods). The first test signal was a step function with a 10Hz sine overlay (Fig. 3.5A). As expected, the DC component of the recorded output was greatly attenuated by the system's 0.1Hz high-pass filter while the 10Hz sine was unaffected (Fig. 3.5B). Deconvolution of this output with the UIR reconstructed a function that closely resembled the original synthetic input (Fig. 3.5C).

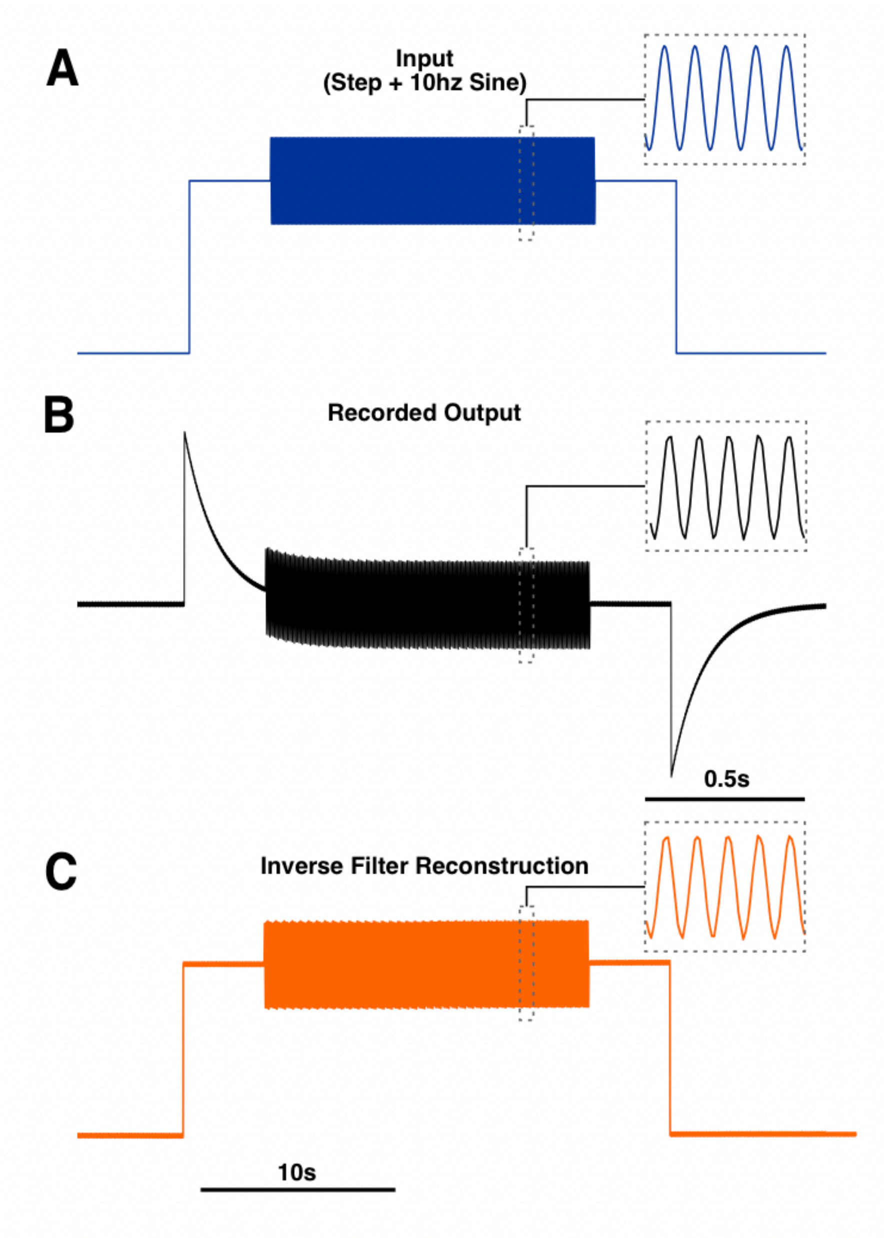

Figure 3.5. Inverse filter reconstruction of a step function with a 10Hz oscillation. A signal composed of a 10Hz oscillation riding on the top of a step function was used as input into the EEG system **(A)**. The system's recorded output **(B)** was deconvolved with the system's UIR, resulting in a reconstruction of the original step function **(C)**. The dotted line insets indicate a 0.5s window showing the 10Hz oscillation.

Next, we tested an input that was a mixed sine function composed of the following frequencies: 0.01, 0.05, 0.07, 0.15, 0.2, 1, 6, and 10Hz (Fig. 3.6A1). Presence of these frequency components were confirmed with an amplitude spectrum (Fig. 3.6A2). Low frequency components were visibly attenuated in the EEG system's recorded output, and an amplitude spectrum confirmed this attenuation (Fig. 3.6B1, B2). Inverse filtering of the recorded output resulted in a mixed sine wave with the low frequency components restored, which was evident by visual inspection of the time series and confirmed by the amplitude spectra (Fig. 3.6C1, C2).

The phase spectra of the recorded output showed that the recording process distorts the phase of the input signal (Fig. 3.6A3, B3). The phase spectra of the original input and reconstruction were similar, demonstrating that the inverse filter was also able to correct the phase distortion caused by the EEG system (Fig. 3.6A3, C3). The fidelity of the reconstruction to the original input was quantified by correlation analysis. The time series, amplitude spectra, and phase spectra of the original input were more highly correlated with the reconstruction than the recorded output (Table 3.1).

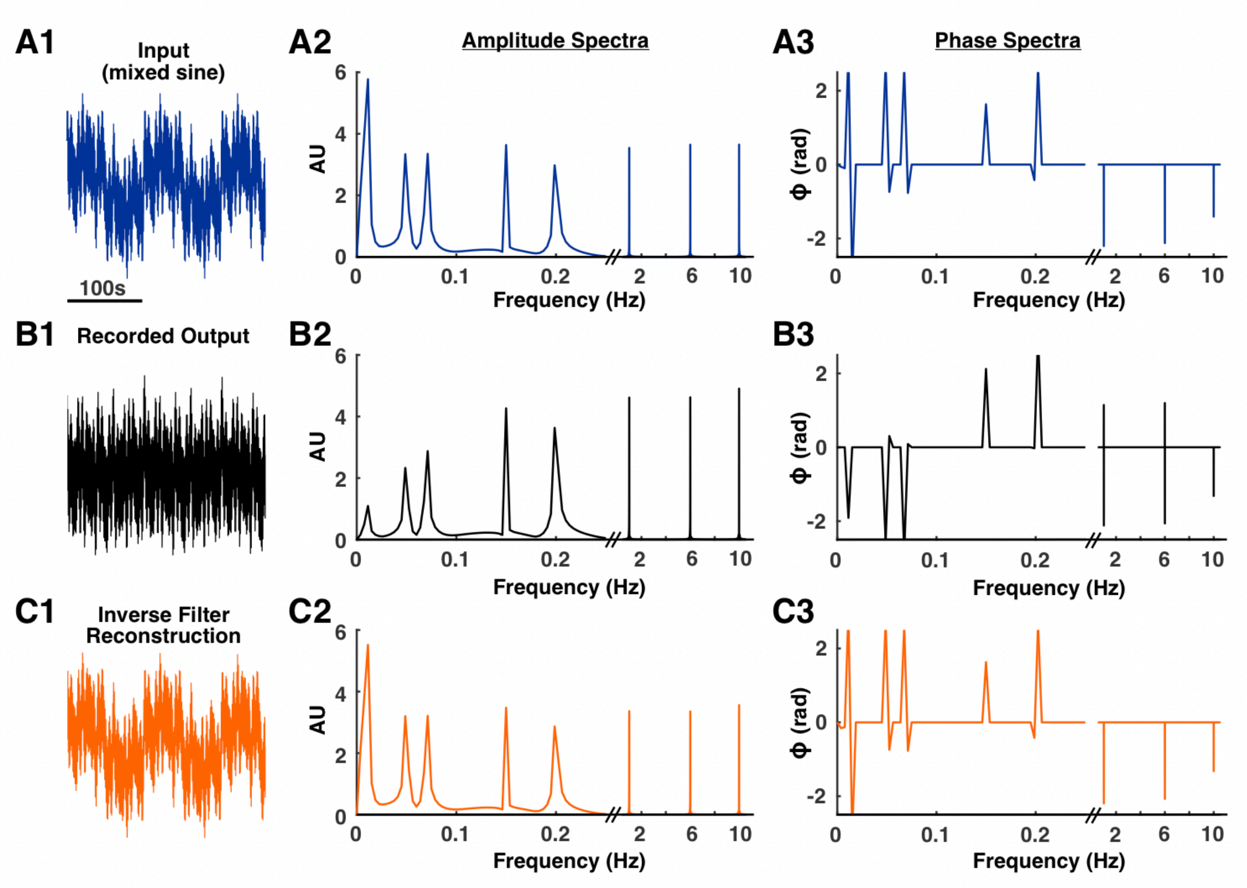

Figure 3.6. Inverse filter reconstruction of a mixed sine signal.
An input signal with known low frequency components was generated by mixing sine waves of varying frequencies **(A1)**. The frequency composition was confirmed with an amplitude spectrum **(A2)**. As expected, activity in frequencies below 0.1Hz was attenuated in the recorded output **(B1, B2)**. The recording process also introduced a phase distortion **(A3, B3)**. Deconvolution of the recorded output with the system's UIR resulted in a signal with the low frequency components restored **(C1, C2)**. This deconvolution process also corrected the phase distortion **(A3, C3)**.

Table 3.1. Correlation results for comparing the time series, amplitude spectra, and phase spectra for the mixed sine signal.
In all comparisons, the correlation between the input and reconstruction was higher than the correlation between the input and recorded output.

Correlation results for mixed sine signal

Time series correlations

		Recorded output	Inverse filtered reconstruction
Input	Pearson correlation Sig. two-tailed N	r = 0.70 p < 0.001 n = 68304	r > 0.99 p < 0.001 n = 68304

Amplitude spectra correlations

		Recorded output	Inverse filtered reconstruction
Input	Pearson correlation Sig. two-tailed N	r = 0.84 p < 0.001 n = 34153	r > 0.99 p < 0.001 n = 34153

Phase spectra correlations

		Recorded output	Inverse filtered reconstruction
Input	Pearson correlation Sig. two-tailed N	r = 0.036 p < 0.001 n = 34153	r > 0.99 p < 0.001 n = 34153

3.3.3 Application of deconvolution-based inverse filter to a known biological signal

Next, we wished to test a signal that was of biological relevance. A recording of a hippocampal seizure in a mouse that was available through a public repository was used (Bonaccini Calia et al., 2022) (Methods). This seizure was originally recorded with a DC amplifier, which allowed preservation and recording of low frequency components. Notably, there is a DC shift prior to the start of the seizure and spreading depolarization activity after the seizure (Fig. 3.7A1). These features were predictably attenuated in the recorded output (Fig. 3.7B1). Inverse filtering of this recorded output resulted in a signal that was similar to the original input signal in time, frequency, and phase (Fig. 3.7C1, C2, C3). This fidelity was confirmed with correlation analysis that showed that, for all measures, the input signal was more highly correlated with the reconstruction than the recorded output (Table 3.2).

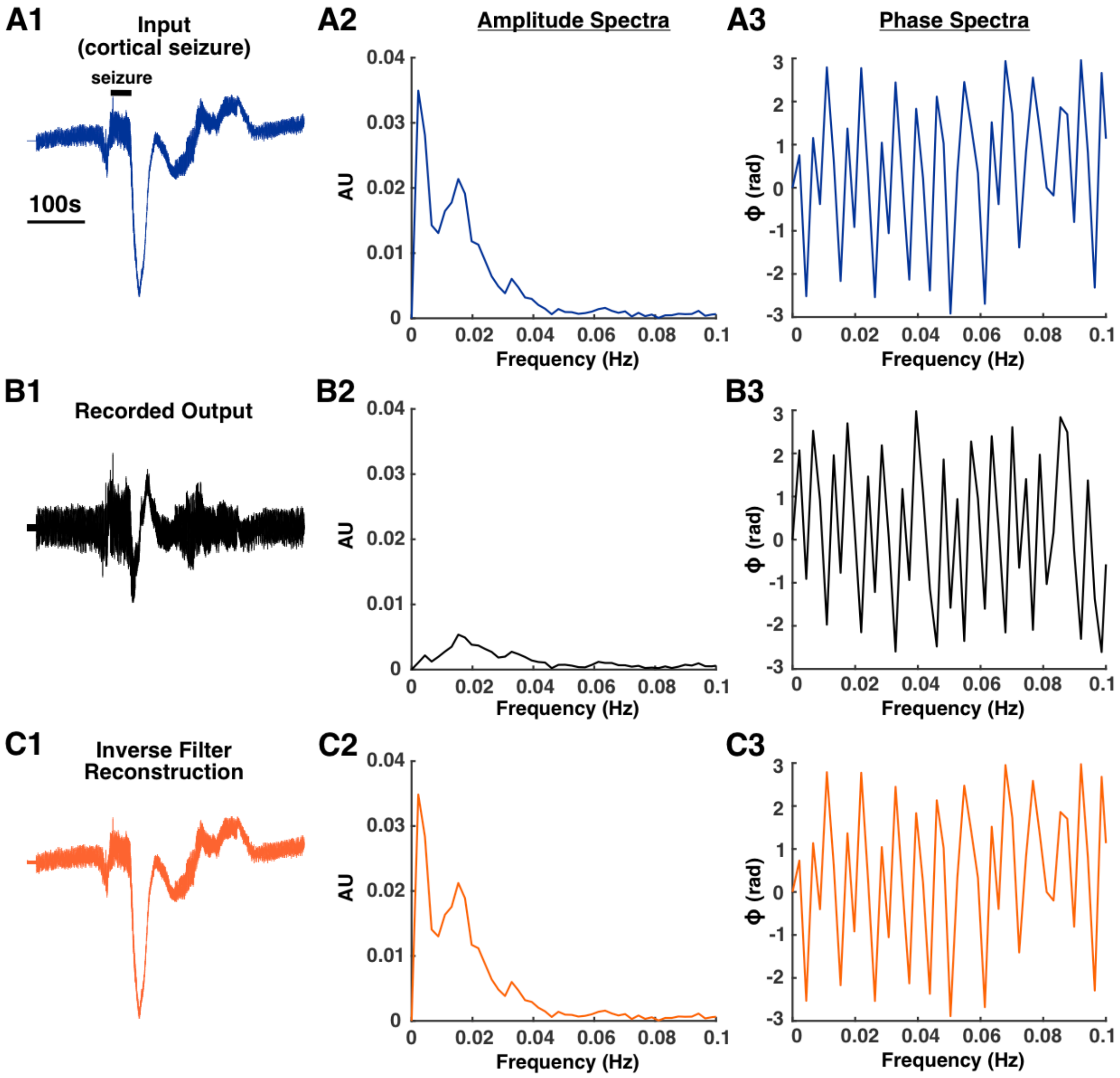

Figure 3.7. Inverse filter reconstruction of a mouse hippocampal seizure

A mouse hippocampal seizure with a known low frequency shift shortly after seizure offset was used as the input signal **(A1)**. The presence of infraslow frequencies was confirmed with an amplitude spectrum **(A2)**. As expected, activity in frequencies below 0.1Hz was attenuated in the recorded output **(B1, B2)**. The recording process also introduced a phase distortion **(A3, B3)**. Deconvolution of the recorded output with the system's UIR resulted in a signal with the low frequency components restored **(C1, C2)**. This deconvolution process also corrected the phase distortion **(A3, C3)**.

Table 3.2. Correlation results for comparing the time series, amplitude spectra, and phase spectra for the mouse cortical seizure.
In all comparisons, the correlation between the input and reconstruction was higher than the correlation between the input and recorded output.

Correlation results for mouse cortical seizure

Time series correlations

		Recorded output	Inverse filtered reconstruction
Input	Pearson correlation	$r = 0.22$	$r > 0.99$
	Sig. two-tailed	$p < 0.001$	$p < 0.001$
	N	$n = 116797$	$n = 116797$

Amplitude spectra correlations

		Recorded output	Inverse filtered reconstruction
Input	Pearson correlation	$r = 0.66$	$r > 0.99$
	Sig. two-tailed	$p < 0.001$	$p < 0.001$
	N	$n = 58399$	$n = 58399$

Phase spectra correlations

		Recorded output	Inverse filtered reconstruction
Input	Pearson correlation	$r = 0.72$	$r = 0.90$
	Sig. two-tailed	$p < 0.001$	$p < 0.001$
	N	$n = 58399$	$n = 58399$

3.3.4 Application of deconvolution-based inverse filter to clinical EEG recordings

In the results presented so far, we validated the ability of our inverse filter algorithm to restore low frequencies by using known input signals. Next, we wished to test our inverse filter on a dataset where the ground truth (i.e., the original signal) is unknown. To do this, we used the inverse filter to study low frequency activity in seizure recordings obtained during long-term monitoring of temporal lobe epilepsy patients. Because the EEG set-ups used in the inpatient unit are not portable, characterizing the UIR using the laboratory-based D/A signal generation system is impractical. Therefore, we wished to develop a more convenient method to characterize the UIR. To do this, we took advantage of the fact that the clinical system includes a square wave calibration signal. Because a square wave is simply a series of step functions, we recorded this calibration output, averaged three step responses, and fitted a function to this average to approximate the system's step response (Fig. 3.8A). To check that the UIR was characterized correctly, this UIR was used to deconvolve the recorded calibration signal, which resulted in a function resembling a square wave (Fig. 3.8B).

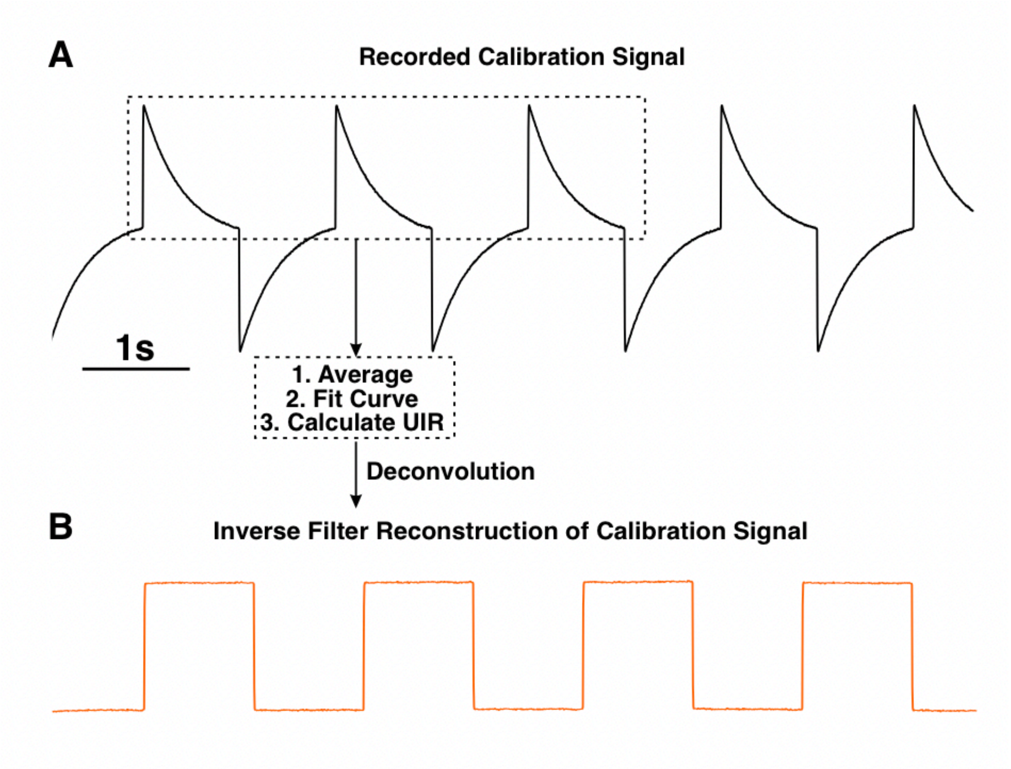

Figure 3.8. Characterizing the unit impulse response (UIR) for an inpatient XLTEK EEG system using the native calibration signal.
The native calibration signal is known to be a square wave, which may be thought of as a series of step functions. The average of three peaks in the calibration signal was used to approximate the system's step response and calculate the UIR **(A)**. Deconvolution of the calibration signal with the calculated UIR resulted in the expected square wave **(B)**.

The UIR derived from the calibration signal was used to deconvolve intracranial recordings obtained from epilepsy patients undergoing presurgical monitoring for medically intractable, temporal lobe epilepsy (Table 3.3). Figures 3.9 and 3.10 show example reconstructions of right-sided hippocampal depth (RHD) electrodes for two different patients. The depth probe is inserted along the anterior-posterior axis of the hippocampus, with RHD1 being the most anterior electrode (Methods).

Table 3.3. Patient demographics and diagnoses.
Age refers to the age at which the recording was obtained. TLE = temporal lobe epilepsy

Patient #	Age (years)	Gender	Diagnosis	Engel score
1	20	Female	Drug-resistant TLE	II
2	51	Female	Drug-resistant TLE	I

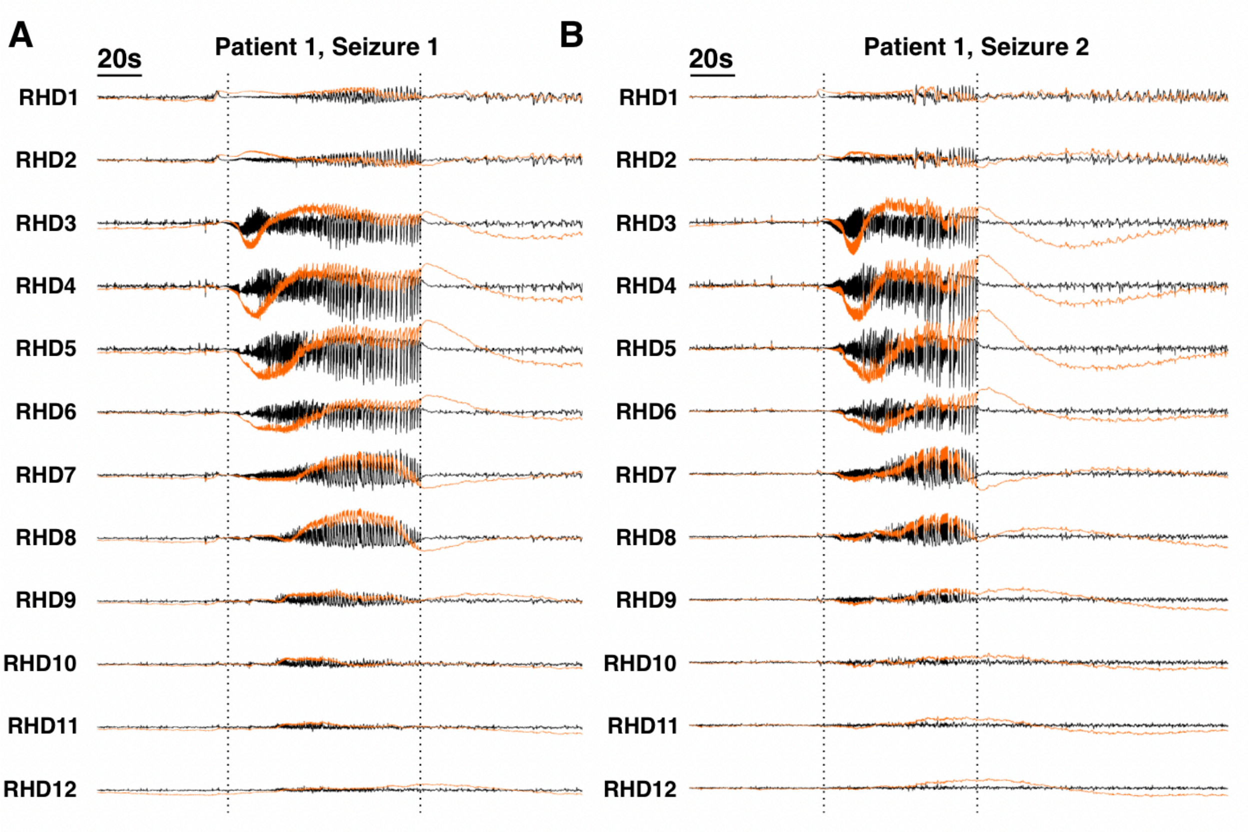

Figure 3.9. Inverse filter reconstruction of two intracranial ictal recordings for Patient 1.

Black traces are the raw recorded signals, orange traces are the inverse filtered signals. Large amplitude, low frequency shifts are present at the start of the seizure in electrodes RHD3-6 **(A)**. These observations were replicated in a second seizure from the same patient **(B)**. RHD = right hippocampal depth. Vertical dotted lines indicate seizure onsets and offsets.

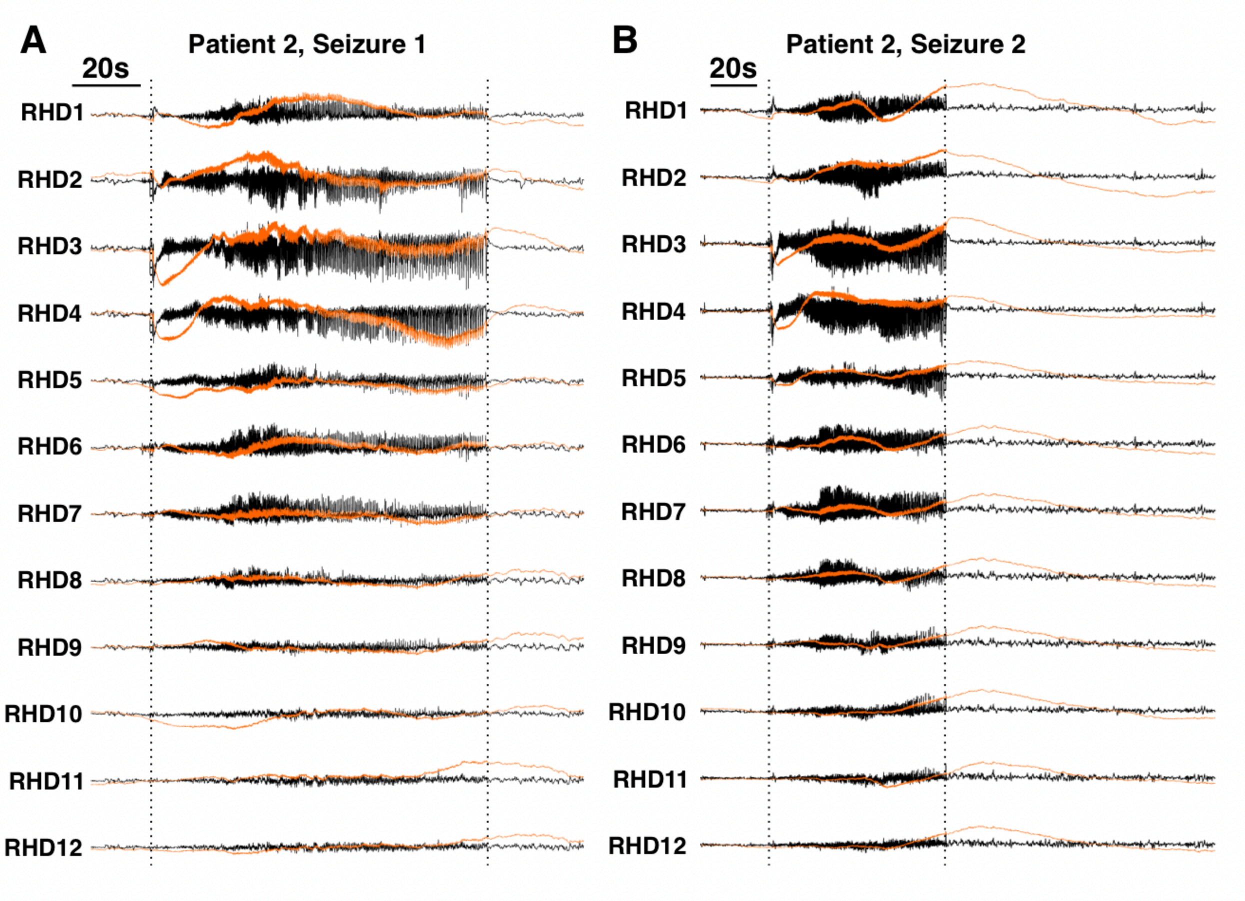

Figure 3.10. Inverse filter reconstruction of intracranial ictal recordings for Patient 2.

Black traces are the raw recorded signals, orange traces are the inverse filtered signals. Large amplitude, low frequency shifts are present at the start of the seizure in electrodes RHD3-4 **(A)**. These observations were replicated in a second seizure from the same patient **(B)**. RHD = right hippocampal depth. Vertical dotted lines indicate seizure onsets and offsets.

To demonstrate that the reconstructions successfully recovered low frequency signals, high resolution, time-frequency analysis was performed using a Morlet wavelet. An example of the wavelet analysis for a single channel result for Patient 1, Seizure 1 is shown in Figure 3.11. A distinct lack of power in frequencies below 0.1 Hz was observed in the analysis of the raw signal (Fig. 3.11B), as expected by the presence of the 0.1Hz high-pass filter in the recording system. The inverse filtered reconstruction showed a clear increase in power in the sub-0.1Hz frequency band that is not present in the raw signal (Fig. 3.11C). The increase in power was also temporally aligned with the seizure onset (vertical dotted lines).

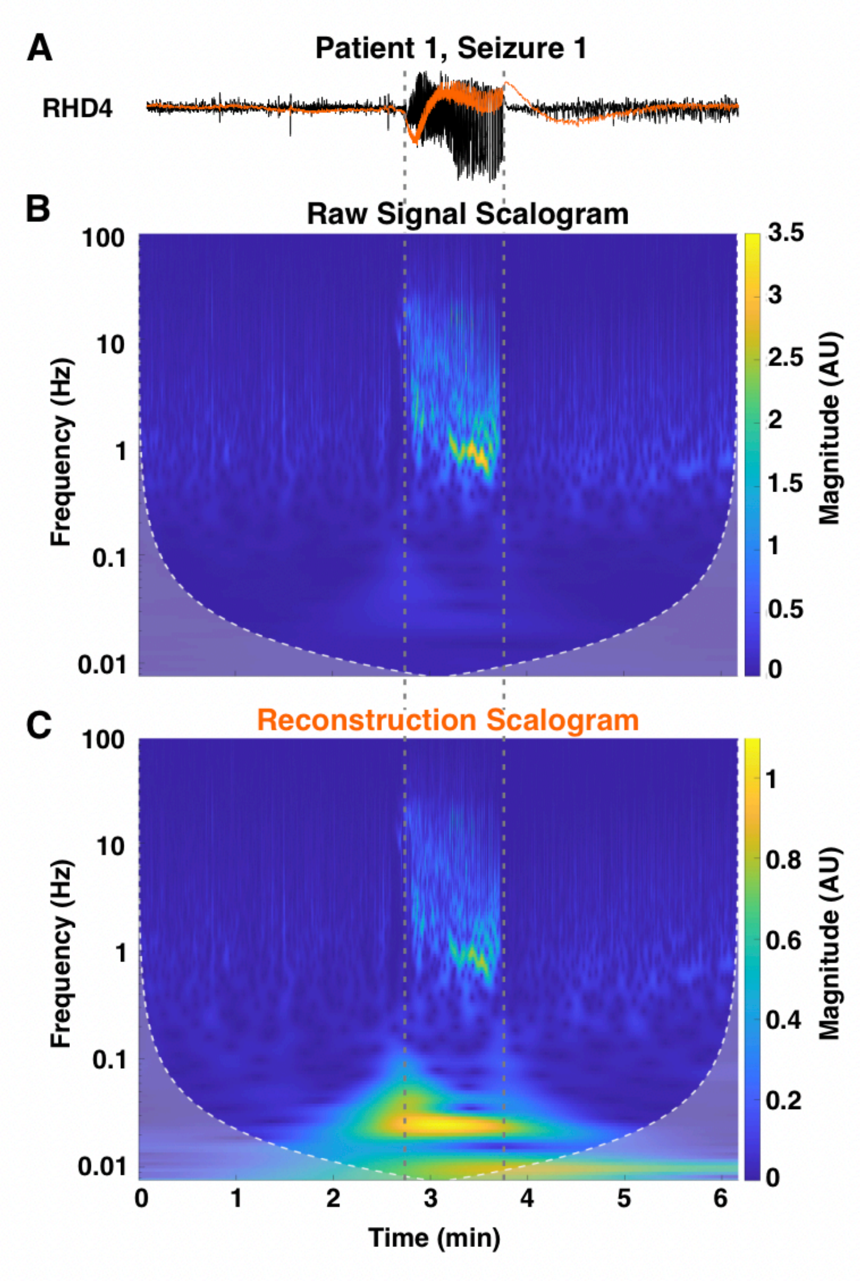

Figure 3.11. Wavelet analysis of channel RHD4 for the recording for Patient 1, Seizure 1.
The inverse filtered reconstruction (orange trace) shows a large low frequency component at seizure onset that is not apparent in the raw recording (black trace) **(A)**. Time-frequency analysis confirmed that frequencies below 0.1Hz are severely attenuated in the raw recording **(B)** but restored in the reconstruction **(C)**. The vertical dotted lines indicate seizure onset and offset.

The restoration of these low frequency components allowed for observations not readily apparent in the raw recordings. In Patient 1, channels RHD3 and RHD4 showed prominent downward shifts at the start of the seizure (Fig. 3.9A). Channel RHD3 also showed a small upward shift prior to seizure onset. Notably, channels RHD3 and RHD4 were identified as the seizure onset zone (SOZ) during the presurgical assessment of this patient. The SOZ was determined by visually identifying channels that first showed ictal activity in the conventional clinical band of 1-70Hz. Channels RHD5 and RHD6 also showed prominent downward shifts that occurred shortly after the shifts in RHD3 and RHD4. Patient 2 showed similar patterns except the downwards shifts were more concentrated in channels RHD3 and RHD4 (Fig. 3.10A). For Patient 2, RHD1-8 were identified as the SOZ during conventional clinical assessment. For both patients, these patterns were replicated in a second seizure recording (Fig. 3.9B, 3.10B), showing that this inverse filter method performs reliably and consistently when applied to clinical recordings.

3.4 Discussion

3.4.1 Advantages of the deconvolution-based inverse filter

The deconvolution-based inverse filter presented in this study offers several advantages over current approaches to studying infraslow activity (ISA) in clinical recordings. The use of DC amplifiers has been suggested as a way to preserve low frequency signals in EEG recordings, and some studies have successfully used such set-ups to study ISA (Kim et al., 2009; Miller et al., 2007; Vanhatalo et al., 2003; Vanhatalo et al., 2004). This method, however, has not been a practical solution for studying ISA in larger, clinical datasets because DC amplifiers are not used in standard clinical equipment. Furthermore, even DC amplifiers have amplifier range limitations that are determined by the power supply potentials. When signals exceed this range, signals become clipped and useful information is lost (Fig. 3.1). One distinct advantage of the method presented in this study is the ability to apply this technique retroactively to clinical recordings obtained with an AC amplifier. The method is entirely computational and does not require any specialty equipment. Consequently, the inverse filter algorithm can be applied to any recordings that are obtained from a system for which a unit impulse response (UIR) can be successfully characterized.

This method is also able to reconstruct the phase information of the original input signal. Hardware filter components, such as those in EEG systems, introduce phase distortions during the filtering process. Our inverse filter method not only reconstructs the attenuated frequency components but also restores the original phase relationships across the spectrum (Fig. 3.6, 3.7). The fidelity of the phase spectrum is important as it allows for accurate comparisons of the relative timing of signal components. This timing is particularly important when studying the activity of different frequency bands in relation to the seizure onset or when studying relationships such as ISA-HFO coupling.

Some other studies have posed the idea of an inverse filter to reconstruct low frequency activity in EEG recordings (Kemp et al., 2010; Nasretdinov et al., 2021). The inverse filter algorithms presented in these studies, however, necessitate characterization of various filter parameters such as resistance and capacitance. This requires knowledge of the precise specifications of the EEG system's real-time, high-pass filter implementation, which may not be readily available, proprietary, or otherwise difficult to obtain. In contrast, the method presented in this study is completely non-parametric, and no specific attributes of the equipment need to be known to characterize the system's UIR. Furthermore, the UIR may be obtained for any clinical recording equipment that include a native calibration signal, which allows this method to be potentially applied more ubiquitously to clinical recordings (Fig. 3.8).

3.4.2 Limitations of the deconvolution-based inverse filter

The deconvolution-based inverse filter relies completely on the ability to accurately characterize the UIR of the recording system. Since the UIR is specific to the model of the amplifier, the UIR must be re-characterized if a different model of amplifier is used. Consequently, any updates to hospital recording systems that involve equipment changes will require a recharacterization of the UIR.

This method can be computationally intensive as the computation time scales exponentially with the length of the signal being reconstructed. Depending on the computing resources available, inverse filtering longer signals (>4hrs) may be not practical, although this issue may be bypassed by reconstructing a series of shorter clips and concatenating the results. Significant downsampling of the signals can be also used to reduce computing time since high sampling rates are not necessary to study low frequency activity.

Finally, this method will also reconstruct any low frequency artifacts that can obscure or confound seizure-related ISA. Therefore, any signal being used must be reasonably noise-free, and reconstructions should be screened for results that likely contain artifactual drifts.

3.4.3 Potential clinical applications

The most distinct advantage of this deconvolution-based inverse filter is that it may be applied retroactively to clinical recordings of seizures. Because ISA has emerged as a topic of interest in identifying epileptogenic tissue (reviewed in Lee et al. (2020)), the ability to observe low frequency activity in larger clinical datasets is critical for further investigation. Although the exact clinical utility of ISA and its potential mechanistic role in seizure generation is beyond the scope of this study, the clinical examples presented here suggest that distinct patterns of ISA can be observed in the SOZ. For Patient 1, the clinically defined SOZ were channels RHD3 and RHD4. Interestingly, these two channels also showed the most prominent ISA at the seizure onset (Fig. 3.9). This is consistent with literature that have suggested that ISA is concordant with the SOZ (Ikeda et al., 1999; Modur et al., 2012). Large amplitude, downward ISAs were also observed in channels RHD5-6, but they occurred after the ISA in channels RHD3-4 and had a longer time course. The mechanistic implication of these observations is a target for future studies, but our current results suggest that ISA patterns allow for differentiation between electrodes in a way that is not evident by conventional methods.

For Patient 2, the standard clinical assessment identified a much more diffuse SOZ spanning RHD1 to RHD8. In contrast to this assessment, Patient 2 shows a concentration of ISA power in a smaller range of electrodes, namely electrodes RHD3 and RHD4 (Fig. 3.10). This observation is consistent with the literature that have suggested that ISA may allow delineation of a smaller epileptogenic area compared to conventional methods (Ikeda et al., 1996; Mader et al., 2005; Rampp & Stefan, 2012; Rodin & Modur, 2008).

3.5 Methods[2]

3.5.1 Recording of synthetic and biological test signals

The three synthetic signals (step, step with 10Hz sine overlay, mixed sine) were generated in MATLAB (MATLAB, Natick, MA, USA) (Fig. 3.4, 3.5, 3.6). Signals were generated with a sampling rate of 1000 samples/s. The mouse hippocampal seizure recording was downloaded from a publicly available repository (https://doi.org/10.5281/zenodo.5655535) (Bonaccini Calia et al., 2022) in HDF5 format, downsampled to 1000 samples/s, and converted to a *.mat file (Fig. 3.7A1). These signals were saved as text files, and a plain-text word processor (WordPad, Microsoft, Windows 10) was used to add a header and convert them into *.atf files that could be read by Clampex (Molecular Devices LLC, San Jose, CA, USA, v.10.4.1.10).

Next, a Clampex episodic stimulation protocol was used with a digital/analog (D/A) converter (Digidata 144A, Molecular Devices LLC, San Jose, CA, USA) to generate an analog output corresponding to each test signal. The output from the D/A converter was attenuated by a factor of 1/1000 using a 10 kOhm/10 Ohm resistor pair in series. This attenuated signal was

---

[2] Custom scripts used to generate the results presented in this chapter can be found at https://github.com/sominlee14/deconvolution_based_inverse_filter (Appendix).

recorded with a clinical EEG machine (Natus XLTEK Brain monitor with Connex headbox). The recorded signals were exported in the *.edf format for subsequent analysis in MATLAB.

3.5.2 Unit impulse response curve fitting and deconvolution

Curve fitting to approximate the step response was performed using the *polyfit* interface in MATLAB. A 9th order polynomial was used. Deconvolution was performed using the *deconv* function. Signals were zeroed by subtracting the mean prior to deconvolution. MATLAB scripts that demonstrate this process step-by-step are available in a Github repository (https://github.com/sominlee14/deconvolution_based_inverse_filter) (Appendix).

3.5.3 Signal processing and statistical analysis

All signal processing and statistical analyses were performed in MATLAB. All reconstructed signals were filtered with a 2nd order, high-pass Butterworth filter with a cutoff frequency of 0.005Hz prior to visualization. This filter step is necessary because the deconvolution process, in some cases, introduces a triangular drift due to the accumulation of rounding errors. The frequency of this drift is entirely dependent on the epoch length of the signal being deconvolved and is equal to $\frac{1}{2 \times epoch\ length}$. To avoid confounding this triangular drift with ictal-associated slow activity, we only used signals with lengths at least three times the period of the lowest frequency of interest. For example, to analyze frequencies around 0.005Hz, the signal being inverse filtered was at least 600 seconds long.

3.5.4 Patients and clinical data acquisition

Clinical EEG recordings were collected from two patients undergoing phase II monitoring for medically intractable, right temporal lobe epilepsy at the University of Chicago Adult Epilepsy Center (Supplementary Table S3). Written informed consent was obtained through a process approved by The University of Chicago Institutional Review Board. For both patients, intracranial recordings were collected using depth electrodes placed into the right hippocampus, 12 channel depth electrodes placed along the length of the right hippocampus with contact #1 (RHD1) being most anterior and contact #12 (RHD12) being most posterior. Other intracranial electrodes were placed in other locations, but recordings from these channels were not used for this study.

All patient recordings used in this study were collected using an XLTEK EEG recording system (Natus Neurolink IP EEG Amplifier, INBOX-1166A/B, Natus, Pleasanton, CA, USA). Signals were digitized at 1024 samples/s and referenced to the FCz electrode. The raw broadband (0.1-344Hz) was converted into *.mat files using a custom C++ routine. Signals were downsampled to 256 samples/s for all subsequent analyses.

CHAPTER 4

Characterization of the spatiotemporal relationship between spiking and LFP during focal seizures[1]

Attestation statement

The work presented in this chapter was a collaborative effort with Sarita Deshpande, a fellow PhD student in the Wim van Drongelen lab. She and I equally split all major elements of this project including project design, data preprocessing, data analysis, and figure generation.

4.1 Summary

The relationship between action potentials and the associated local field potential (LFP) in neural recordings is typically studied only in the temporal domain using the spike-triggered average (STA). In this study, we present a novel approach, termed the spatiotemporal spike-centered average (st-SCA), that allows for visualization of the spike-LFP relationship in both the temporal and spatial domains. In this method, a 3D spatiotemporal topography of spike-associated LFP is calculated from a 2D spatial average of the LFP centered around the time and location of individual spikes. We applied this method to 25 microelectrode array (MEA) recordings obtained from seven patients with pharmacoresistant focal epilepsy during ictal and interictal states. Five patients in this dataset had MEA implants in recruited cortex, and two had implants in unrecruited cortex. Of the five patients with arrays implanted in recruited territory, three showed STAs that resembled sine cardinal (sinc) functions, and two showed non-sinc functions. Using the st-SCA, we found that the patients who showed a sinc-function pattern in the temporal domain showed a donut-shaped ring of LFP activity in the spatial domain. This observation was corroborated by a theoretical model describing an ictal spike as measured by a

---

[1] Results presented in this chapter are in revision at *Communications Biology*.

macroelectrode. The model also revealed a special symmetry wherein the temporal component of the st-SCA predicts the spatial component when they both approximate sinc-functions. Supporting this theoretical derivation, a radial cut of the donut-shaped st-SCA showed a spatial pattern consistent with a sinc-function. This spatial sinc-function had peaks separated by ~2.5mm—a measurement that supports the role of mid-range excitatory connections during ictal activity. In sum, these findings suggest that patients whose seizures engage mid-range connections may be identifiable by the spatiotemporal features of ictal spike-associated LFP activity.

4.2 Introduction

Spatiotemporal patterns of brain electrical activity reflect neural mechanisms underpinning different brain pathologies. Consequently, temporal and spatial patterns observed in electrographic recordings are frequently employed to guide diagnostic and therapeutic approaches in the treatment of epilepsy. During surgical evaluation of patients with epilepsy, a variety of electrodes are used to record brain electrical activity across different scales. For example, large-scale global activity can be recorded by macroelectrodes at the scalp or cortex, and meso- and microscale activity can be recorded by intracranial arrays or bundles of microelectrodes (Eissa et al., 2017; Eissa et al., 2016; Schevon et al., 2012). Despite the heavy reliance on electrophysiology in clinical practice, the relationship between neural activity across scales and the mechanistic implications of the observed spatiotemporal patterns remain poorly characterized.

One important question in understanding cortical seizure dynamics is how the activity of individual neurons relates to local and global network activity in ictal and interictal states. The interactions of neural networks during human focal seizures across micro-, meso- and macroscopic scales have been characterized by other recent studies (Eissa et al., 2017). Specifically, one study showed that the spike-triggered average (STA) of the ongoing low frequency component of the local field potential (LFP) could be approximated by a sine cardinal (sinc) function (Eissa et al., 2018). Furthermore, filtering a train of ictal action potentials with a rectangular (brick wall) filter generated an output that correlated well with the observed seizure, consistent with the fact that the Fourier transform of a rectangular function is the sinc-function (Van Drongelen, 2018). While the ictal STA was determined in the temporal and frequency domains, the spatial component of the relationship between action potentials and low frequency LFP was not characterized.

Similarly, most previous studies that describe the relationship between single spiking activity and the surrounding LFP have focused primarily on temporal descriptions using the STA (Bazelot et al., 2010; Glickfeld et al., 2009). The few studies that have investigated the spatial component of this relationship do so by incorporating spatial information into the STA through the addition of spatial filters (Telenczuk et al., 2017) or use a covariance-based approach (Rust et al., 2004). None so far have directly visualized the full spatial topography of LFP associated with spiking activity.

In this study, we present a novel approach, termed the spatiotemporal spike-centered average (st-SCA), in which a mesoscale spatial topography of spike-associated LFP can be visualized by calculating a spatial average of the LFP centered around the location of individual spikes. Calculation of this topography results in a powerful tool that allows for the visualization of both the spatial and temporal components of the spike-LFP relationship. We apply this method to microelectrode array (MEA) recordings of human focal seizures to reveal unique spatiotemporal patterns that support the role of mid-range excitatory connections during ictal activity. We then combine these MEA observations with a mathematical model describing an ictal spike as measured by a macroelectrode to show that, in special cases, the temporal and spatial features of the spike-associated LFP can predict one another. In the discussion, we explore the biological mechanisms and clinical implications of the newly observed spatiotemporal properties in the context of pharmacoresistant focal epilepsy.

4.3 Results

To expand upon the traditional temporal characterization of the complex relationship between neuronal firing and the overlying global LFP, we introduce a novel calculation termed the spatiotemporal spike-centered average (st-SCA). The st-SCA builds upon the more typically utilized STA by accounting for both spike timing and location. The st-SCA is determined with respect to the action potential's timing (t, temporal component) and location in the cortical plane (x, y; spatial component). To do this, we characterize the multi-unit action potential train (with i = 1, ... , N action potentials occurring at x_i, y_i, t_i) as a series of unit impulses:

$$\sum_{i=1}^{N} \delta(x - x_i, y - y_i, t - t_i) \tag{4.1}$$

This produces the expression for the normalized spatiotemporal cross-correlation $C(\xi, \psi, \tau)$ between the LFP and action potential:

$$C(\xi, \psi, \tau) = \frac{1}{N} \iiint \left(\sum_{i=1}^{N} \delta(x - x_i, y - y_i, t - t_i)\right) LFP(x + \xi, y + \psi, t + \tau)\ dx\, dy\, dt \tag{4.2}$$

To evaluate this expression, we interchange the integration and summation operations and integrate over the spatiotemporal domain. The resulting expression is defined as the st-SCA:

$$C(\xi, \psi, \tau) = \frac{1}{N} \sum_{i=1}^{N} LFP(x_i + \xi, y_i + \psi, t_i + \tau)\ =\ st\text{-}SCA(\xi, \psi, \tau) \tag{4.3}$$

Note that if we set the range of (ξ, ψ) equal to the area covered by a fixed spatial range, we obtain the well-known temporal STA (Fig. 4.1A). In contrast, if we set τ to a fixed temporal range, we obtain purely the spatial component of the st-SCA for that epoch. In the following, we describe the computational steps to determine the st-SCA in MEA recordings.

4.3.1 Calculation of the st-SCA in MEA recordings

To apply the st-SCA to MEA recordings, we must account for the irregular timing and location of spiking activity across the array. A simplified analogy of this approach is to visualize spiking activity as stones being tossed into water. Consider throwing a single stone into water and analyzing the consequent effects by observing the resulting water ripples. We can simulate multiple sources by dropping identical stones from the same height but at different times and locations across the horizontal plane of the water surface, resulting in a complex landscape. To determine the contribution of a single stone to this landscape, we can take a field of view centered around individual stones. According to Eq. 4.3, averaging across all stones gives us the spatial pattern of activity associated with each stone. If we also include the time interval around each dropped stone, we obtain the stone's characteristic spatiotemporal perturbation.

To apply this to the analysis of MEA recordings, spikes are detected for each channel in the MEA (Fig. 4.1B, left column), and the low frequency LFP associated with each spike is determined (Fig. 4.1B, middle column). This LFP is then spatially translated such that the associated spike position (x, y) is at the origin of a new set of axes (ξ, ψ) (Fig 4.1B, right column). This spike detection and LFP translation process is then applied to all channels. Averaging the results across all channels results in a field of view of the spike-associated LFP that is (1) centered around individual spikes and (2) approximately four times larger than the area of the MEA. This field is then calculated for time points τ to result in the st-SCA (Fig. 4.1B, right panel).

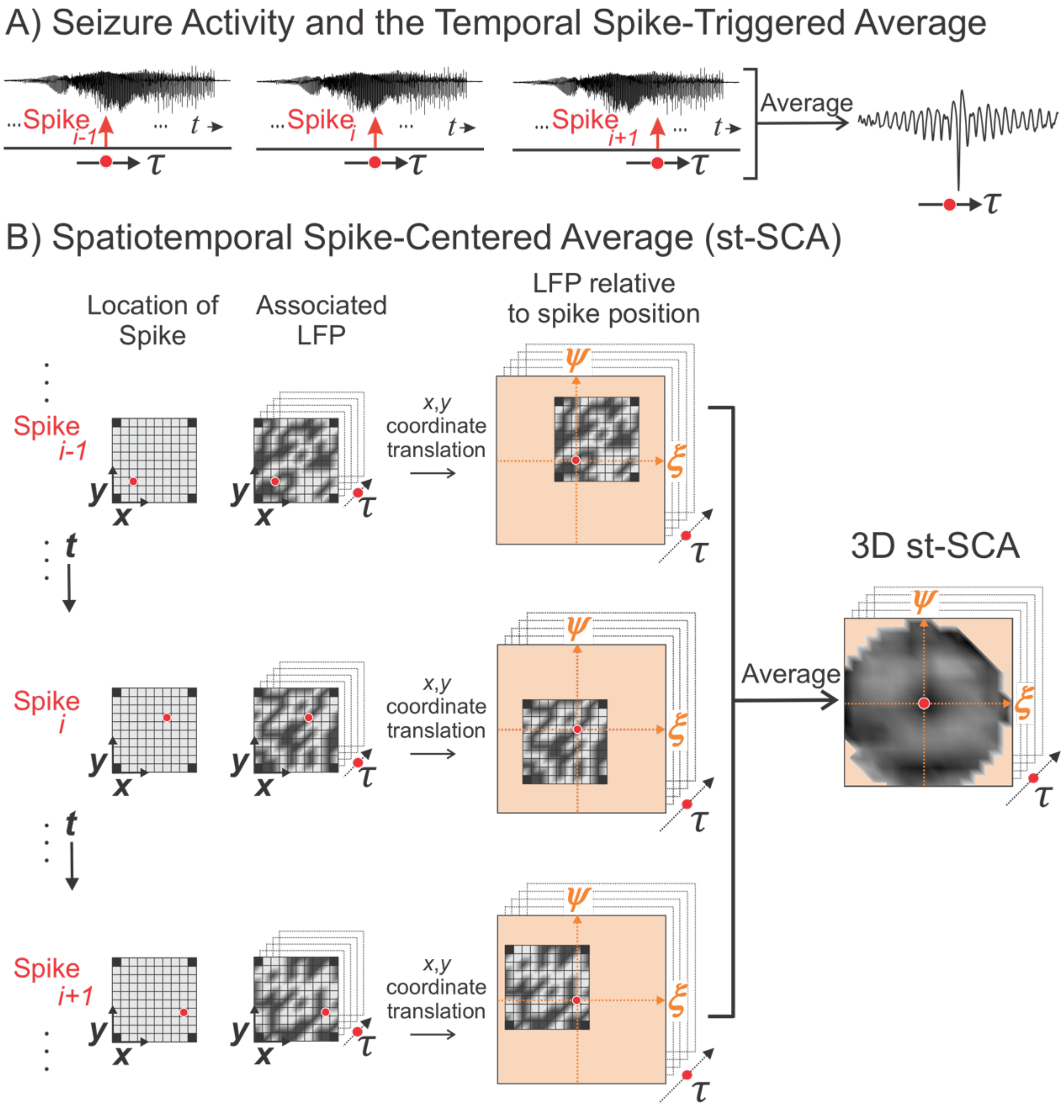

Figure 4.1. Schematic for computing the mesoscale spatiotemporal spike-centered average (st-SCA) between spiking activity and the local field potential (LFP) during a human focal seizure.

(A) During seizure activity, the LFPs within the area of the electrode array (the summed LFP of the microelectrode array is depicted in the upper trace) are associated with a multi-unit action potential train. The LFP's relationship to the spike is considered over time τ relative to the spike events.

(B) For each spike (left column) across the MEA, its associated spatiotemporal LFP (middle column) is determined. The red circle in the middle column indicates the spike position on the MEA. Next, the (x, y)axes of the LFP are translated into the (ξ, ψ) axes, such that the associated spike position is at the origin (right column). Finally, the results in the right column are averaged to create a matrix that contains the st-SCA. Note that the corners of the average are undefined because the MEA does not have electrodes in the corner positions.

4.3.2 Application of st-SCA to clinical recordings of human focal seizures

We applied the st-SCA method to analyze microelectrode recordings of focal seizures in patients undergoing epilepsy surgery evaluation. These recordings were obtained from 96-channel, 4x4mm MEA during and around ictal activity (Schevon et al., 2012; Truccolo et al., 2011). Filtering was used to extract local multi-unit activity and the associated low frequency component of the LFP of the surrounding network (Methods). A total of 19 seizures from seven patients was used for the study (Table 4.1). Both ictal and interictal recordings were evaluated, where interictal was defined as being at least two hours away from any known ictal activity. Of the seven patients analyzed for this study, five patients had arrays implanted in the recruited seizure territory (Patients 1-5), and two patients had arrays implanted in unrecruited seizure territory but within the clinically-determined seizure onset zone (Patients 6-7) (Schevon et al., 2012). As previously described, recruited seizure territory is defined as local tissue invasion by the seizure wavefront. Unrecruited territory is located outside of the recruited territory but can show rhythmic EEG activity due to local synaptic activity (Merricks et al., 2021; Schevon et al., 2012).

Table 4.1. Patient Table: Demographics and Clinical Features

Patient (age/gender)	Implant location	MEA location	Seizure onset zone	No. seizures analyzed	Seizure type(s)	Pathology
Patient 1 (25yo/female)	Left lateral and subtemporal	Left inferior temporal gyrus 2.5 cm from anterior temporal pole	Left basal/anterior temporal	3	Complex partial	Mild CA1 neuronal loss; lateral temporal nonspecific
Patient 2 (19yo/female)	Right lateral and subtemporal, parietal, occipital	Right posterior temporal, 1 cm inferior to angular gyrus	Right posterior lateral temporal	1	Complex partial with secondary generalization	Nonspecific
Patient 3 (21yo/male)	Left lateral frontal, subfrontal, temporal, subtemporal	Left middle temporal gyrus 1–2 cm posterior to the temporal tip	Left mesial temporal	3	Complex partial	Moderate CA3 & CA4 neuronal loss and gliosis
Patient 4 (32yo/male)	Left lateral temporal, subtemporal, parietal, frontal	Left superior temporal gyrus	Left anterior fronto-temporal	3	Complex partial	Cortical dysplasia
Patient 5 (45yo/male)	Right lateral temporal, parietal, frontal	Right superior temporal gyrus	Right anterior temporo-parieto-occipital	3	Complex partial with secondary generalization	Nonspecific

Table 4.1 (continued).

Patient 6 (30yo/male)	Left lateral frontal, mesial frontal, temporal	Left supplementary motor area, 3 cm superior to Broca’s area	Left supplementary motor area	3	Complex partial/tonic	N/A (multiple subpial transections performed)
Patient 7 (39yo/male)	Left lateral and mesial frontal	Left lateral frontal 2 cm superior to Broca's area	Left frontal operculum (3 × 3-cm cortical area)	3	Complex partial	Nonspecific

The representative STAs calculated across ictal and interictal states for two recruited territory recordings and one unrecruited territory recording are depicted in Figure 4.2. The black lines represent the STAs, the red lines represent the associated noise estimates, and the vertical dotted lines indicate $t = 0$, i.e., the timing of the spike trigger. For both recruited and unrecruited territory recordings, the amplitudes of the ictal STAs (Fig. 4.2C, E, G) were larger than the corresponding the interictal STAs (Fig. 4.2D, F, H). The amplitude for the unrecruited ictal STA (Fig. 4.2G), however, was much smaller than the recruited ictal STAs (Fig. 4.2C, E).

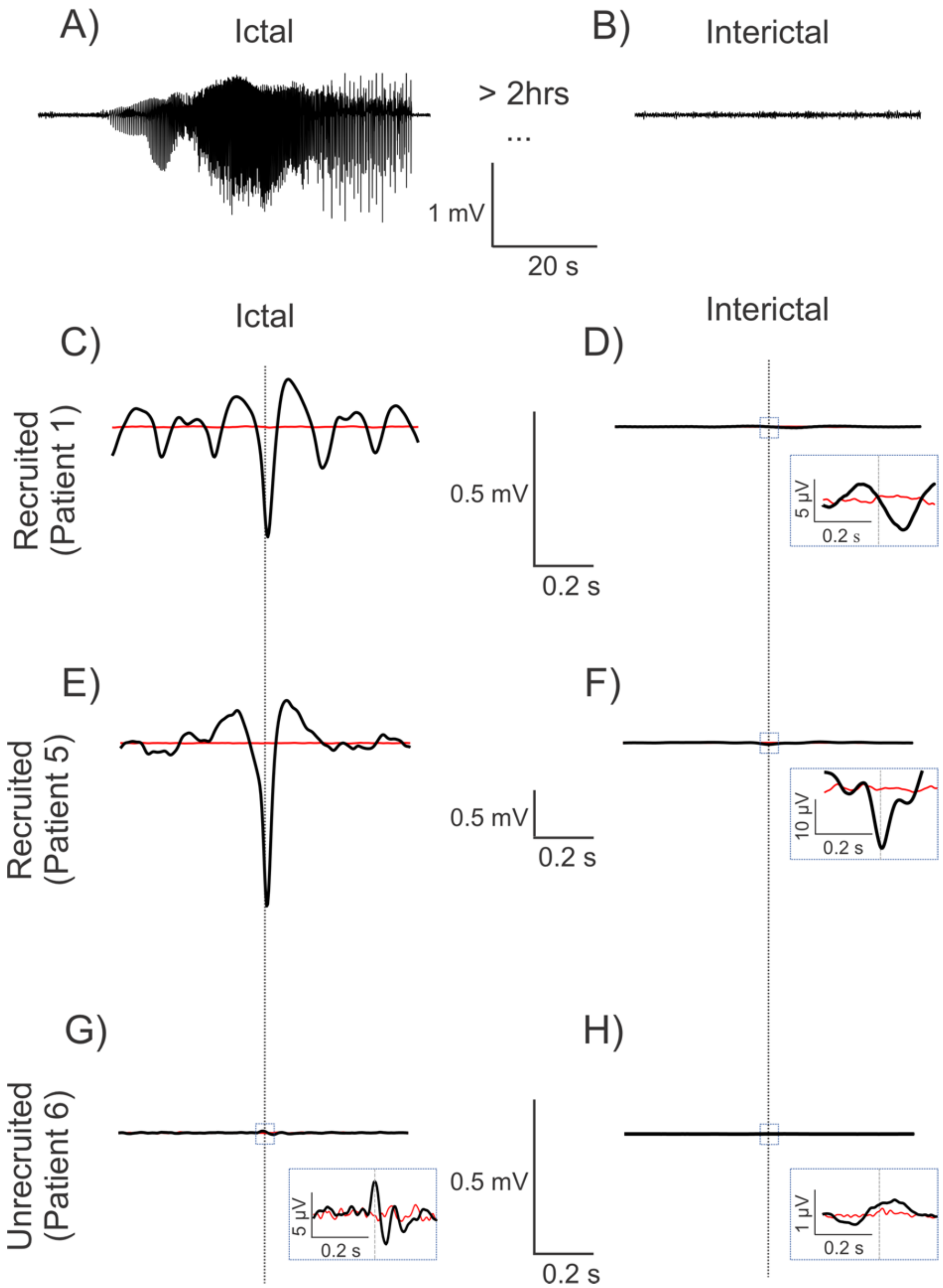

Figure 4.2. Spike-triggered averages (STAs) in recruited and unrecruited cortical territories during ictal and interictal phases show different patterns.

The black traces are the signals, and the red traces represent the associated noise estimates. Vertical stippled lines represent the zero of the time-axis.

(A—B) Example signal trace of average ictal and interictal LFP activity across MEA channels.

(C—F) The STA in the recruited territories show an evolution towards a characteristic negative peak, with or without surrounding oscillations, during the ictal phase. The ictal phase amplitudes are also much higher than those of the interictal phase.

Figure 4.2. (continued)
(G—H) The STA in the unrecruited territory show much smaller, non-zero ictal signals than the ones in the recruited territories. In contrast to the recruited territories, the small but dominant ictal peak polarity is positive in this case.
The insets in panels D, F, G, H show that all unrecruited ictal conditions and all interictal conditions show smaller amplitude, albeit non-zero STAs.

Patients with the MEA located in recruited seizure territory showed STAs with different morphologies (Fig. 4.3A-E), but all had a dominant negative peak around $t = 0$. Consistent with previous findings, we found that the STA for Patients 1-3 resembled a sinc-function with a peak embedded in a weak oscillatory component (Fig. 4.3A-C) (Eissa et al., 2018). In contrast, the STA for Patients 4 and 5 did not resemble a sinc-function as Patient 4 showed a dominant peak embedded in a strong oscillation (Fig. 4.3D) while Patient 5 showed no oscillatory component (Fig. 4.3E). The STAs for Patients 6 and 7 with the MEA in unrecruited territory were weak with a smaller amplitude deflection around to $t = 0$ (Fig. 4.3F, G).

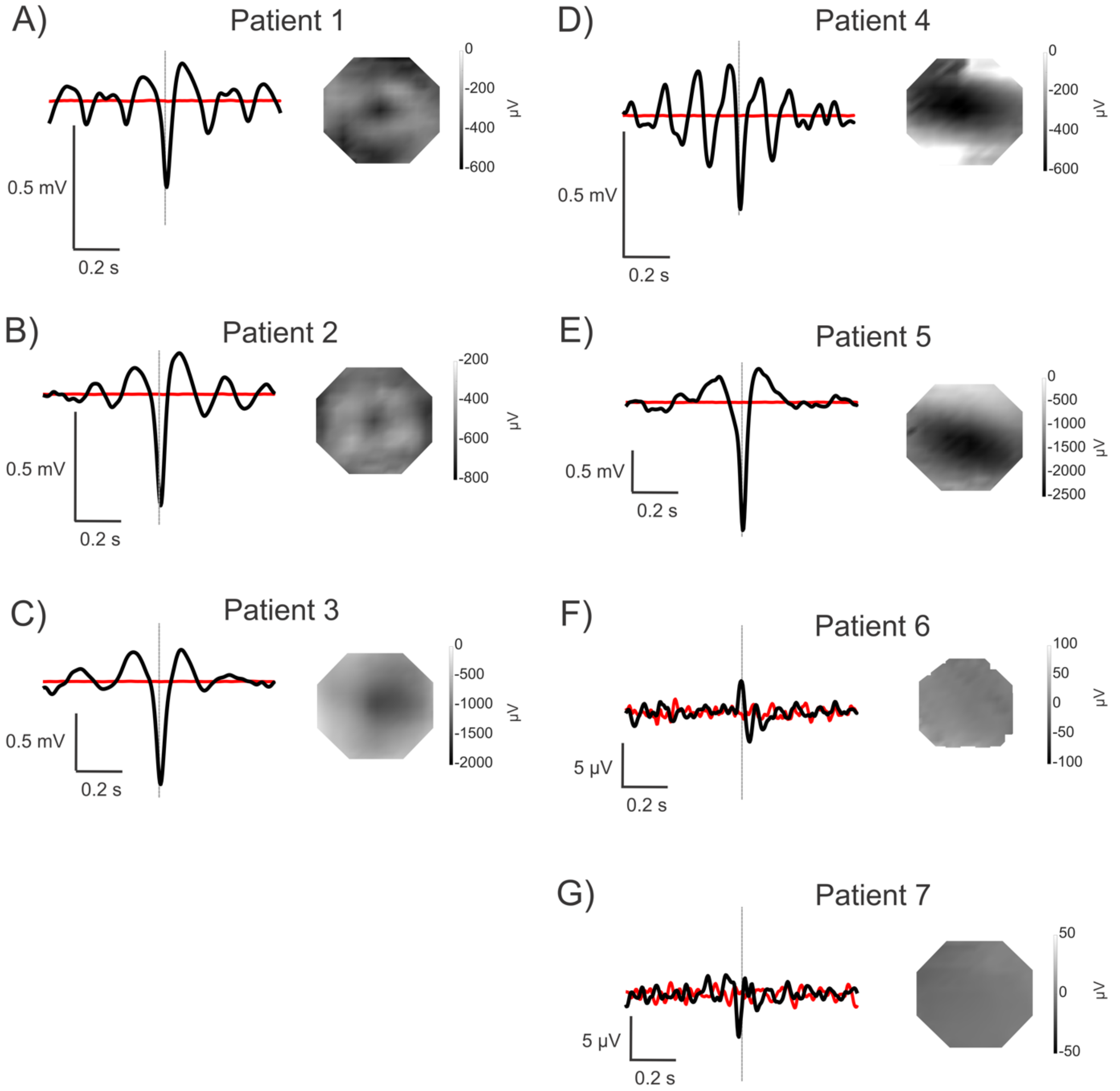

Figure 4.3. Representative temporal and spatial components of the spike-centered averages (SCAs) for each patient.

Patients 1-5 had microelectrode arrays (MEAs) implanted in recruited territory, and Patients 6-7 had MEAs implanted in unrecruited territory. Grayscale is in μV units.

(A—C) Patients 1-3 resemble sinc-functions in the temporal domain.

(D—E) Patients 4-5 resemble deep wells of excitatory activity in the spatial domain.

(F—G) Patients 6-7 are characterized by comparatively smaller amplitude signals in both the temporal and spatial components.

We then evaluated the relationship between spiking activity and the LFP in the spatiotemporal domain by computing the st-SCA over the entire MEA (ξ, ψ) and times $\tau = \pm 1$ms (Fig. 4.4C, D). This 2ms interval was averaged to yield a 2D spatial topography. In the ictal phase for Patients 1-3, we observed a centrally located trough surrounded by a pair of rings with apparent radial symmetry (Fig. 4.3A, B, 4.4C). The distance between the center and the region indicated by the inner circle was ~1.5mm, and the distance between center and the region indicated by the outer circle was ~2.5mm (Fig. 4.4C). In contrast, the ictal phase for Patients 4 and 5 showed a deep well of stronger negative activity (Fig. 4.3D-E, 4.4D). The st-SCAs during the interictal phase as well as the results obtained in unrecruited territories showed different patterns with relatively smaller amplitude signals (Fig. 4.5B, D-F).

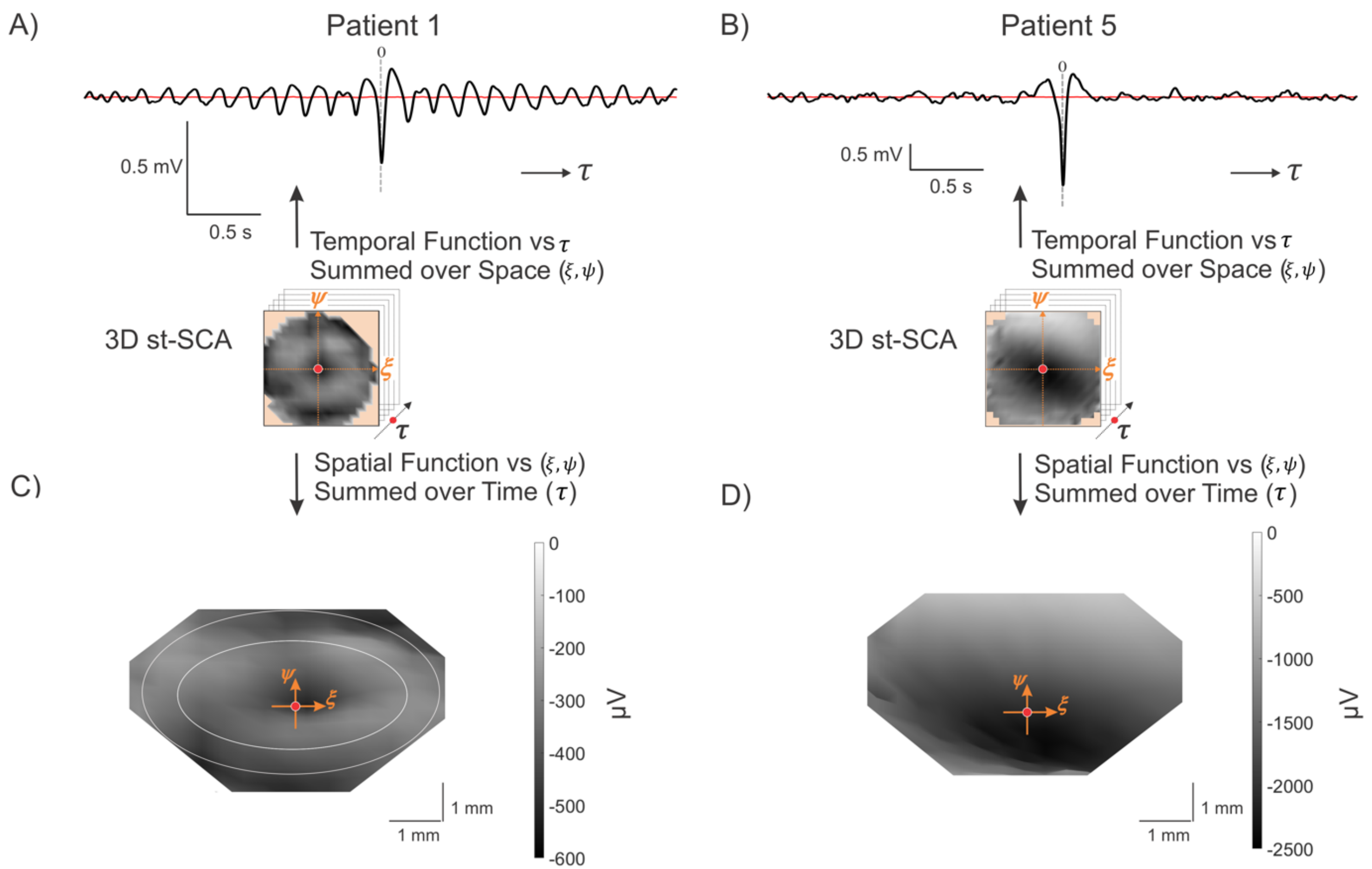

Figure 4.4. Properties of the ictal spatiotemporal spike-centered average (st-SCA) function during a focal seizure show different patterns for two representative patients.

(A—B) The temporal average is calculated by averaging the st-SCA over all spatial contributions (±3.6mm).

(C—D) A 3D view (azimuth = 0°, elevation = 70°) of the 3D st-SCA summed over time τ =±35ms. The center (ξ, ψ = 0,0) is indicated by the red dot. The two concentric circles are drawn to indicate that the center is surrounded by two rings. Note the apparent radial symmetry of the st-SCA pattern in (C). Grayscale is in μV units.

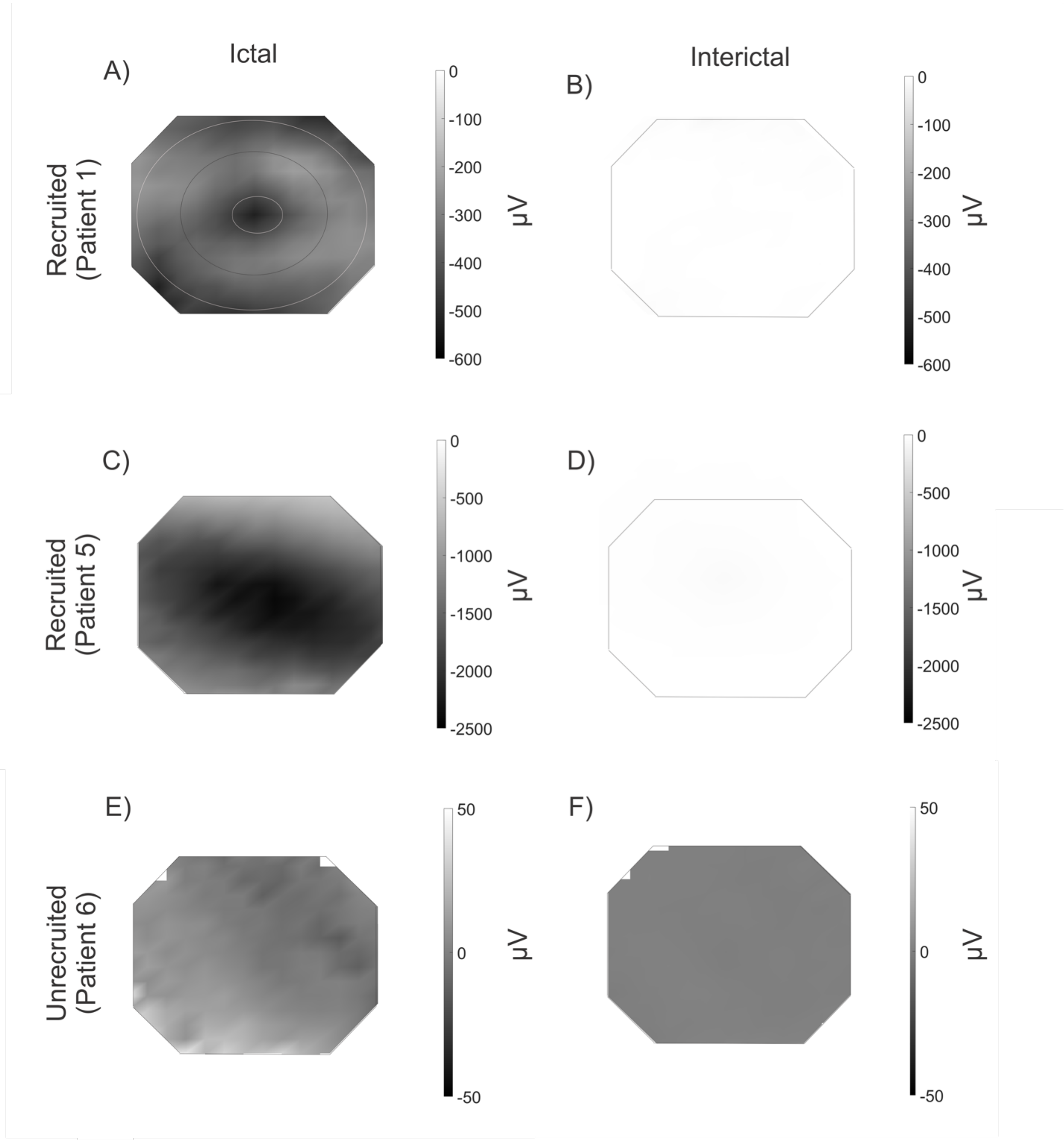

Figure 4.5. Spatial components of the spatiotemporal spike-centered averages (st-SCAs) in recruited and unrecruited territories show differing patterns.
The st-SCA in panels A and C represent the same spike-LFP relationship as depicted in Figure 4.4C and D, respectively. In all patients, the ictal signal **(A, C, E)** is stronger than the interictal one **(B, D, F)**. In Patient 1 **(A)**, the two rings surrounding the center are indicated by the circles. Patient 5 **(C)** instead shows a deep well of negative activity. The dynamics in unrecruited territories **(E-F)** are markedly different and are also much smaller in amplitude. Grayscale is in μV units.

In sum, three of five patients with recordings from recruited territories (Patients 1-3) showed st-SCAs resembling sinc-functions in the temporal domain and st-SCAs resembling donut-shaped rings of activity in the spatial domain (Fig. 4.3A-C, 4.4C). In Patients 4 and 5, the STAs were characterized by a non-sinc morphology, and the st-SCAs showed deep and diffuse wells of negative activity (Fig. 4.3D-E, 4.4D).

Note that these observations were not attributable to widespread correlations among MEA electrodes. To demonstrate that the observed st-SCA patterns are representative of the spike-LFP relationship and not the global, macroscale correlations amongst network LFPs, we showed that STAs in unrecruited territory show a large and significant oscillatory component only when triggered by spikes from recruited territories (Fig. 4.6B), and not when triggered by spikes from unrecruited territories (Fig. 4.6C). This result is a replication of previous studies (Eissa et al., 2017). Furthermore, randomizing the spike times detected across the MEA resulted in complete destruction of the observed st-SCA patterns, emphasizing the importance of spike timing as the driver for these spatiotemporal patterns (Fig. 4.7). Finally, calculation of the st-SCA after applying a spatial filter to decorrelate LFP signals across MEA channels did not qualitatively alter the st-SCA patterns (Fig. 4.8) (Methods).

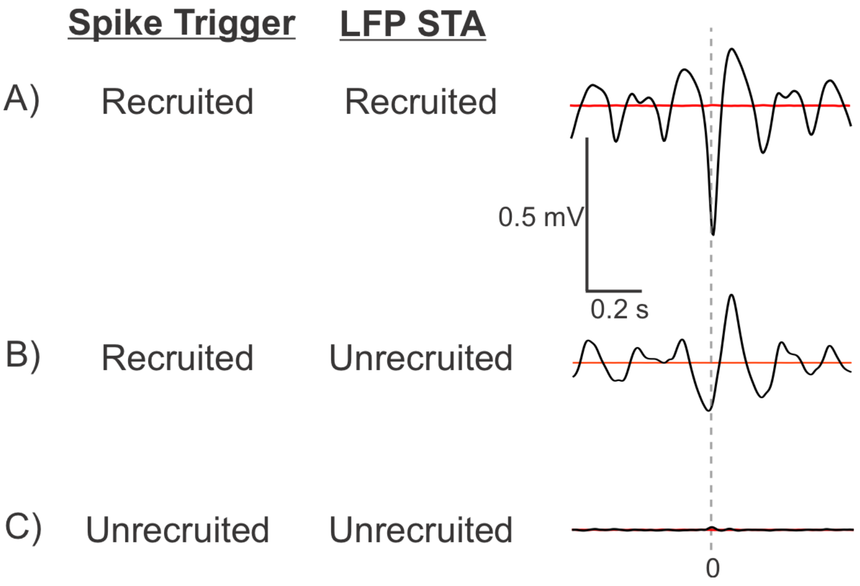

Figure 4.6. Temporal spike-triggered averages (STAs) in recruited and unrecruited territories are calculated with spike triggers from different locations.

The STA of the LFP in the recruited area triggered by spikes in the recruited area **(A)** shows a large negative peak at the time of the trigger. The STA in the unrecruited areas have a strong signal component when triggered by spikes in from the recruited areas **(B)**, but not if triggered by spikes in the unrecruited area **(C)**.

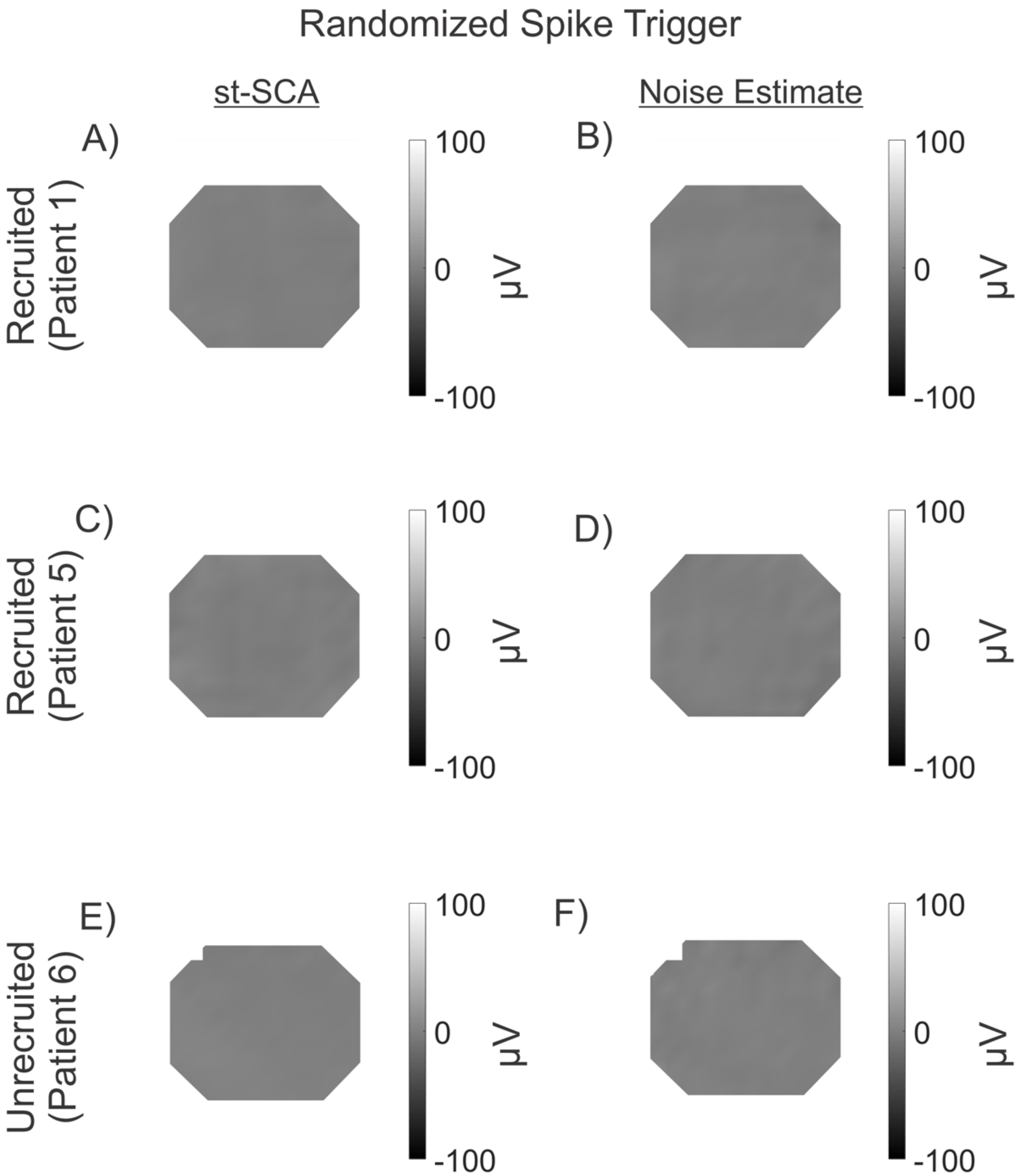

Figure 4.7. Representative spatiotemporal spike-centered averages (st-SCAs) after randomization of spike trigger timing.

When the spikes and local field potential are no longer coupled temporally, no spatial patterns are seen, highlighting the importance of spike timing in the st-SCA calculation. Grayscale is in μV units.

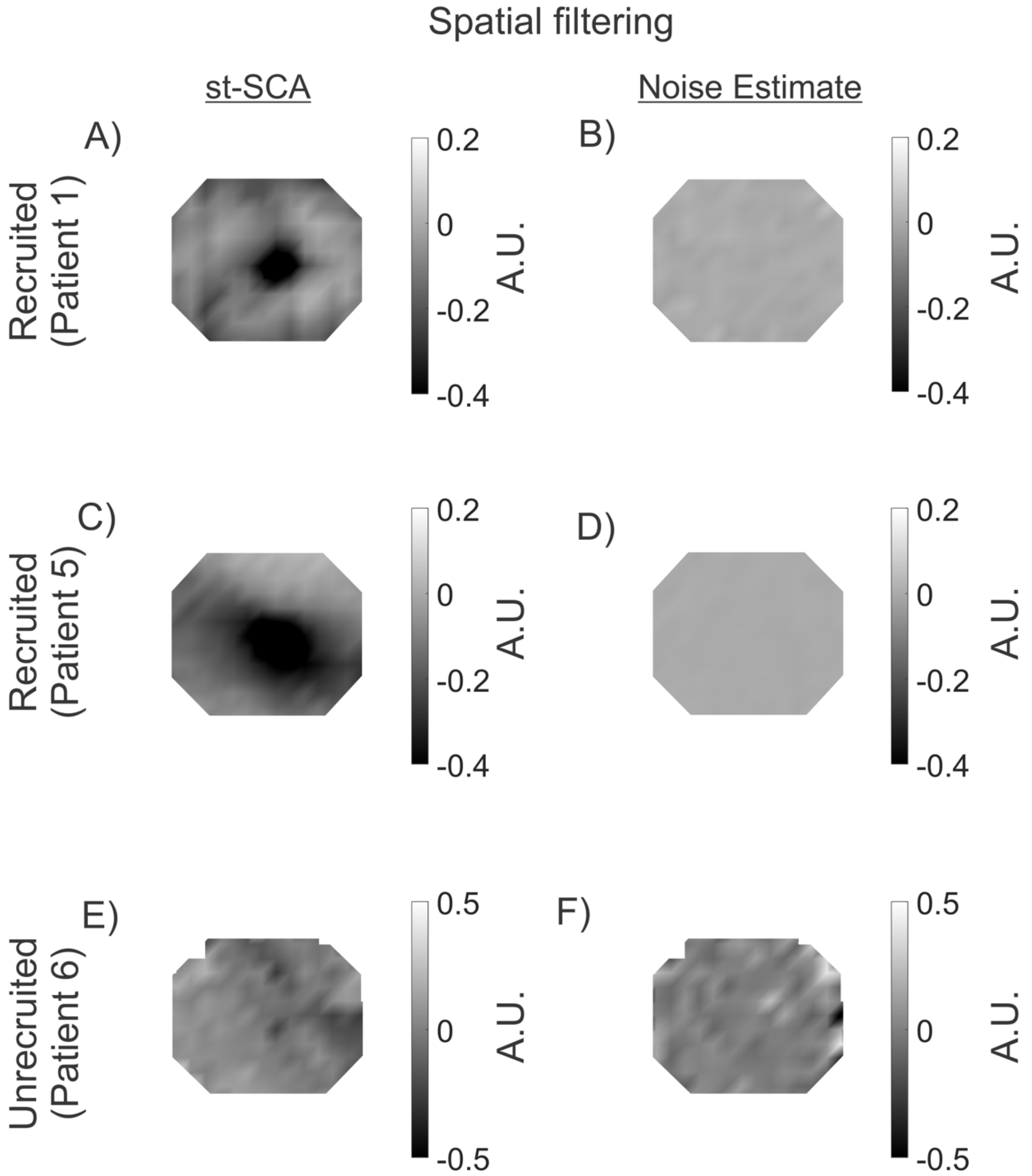

Figure 4.8. Representative spatiotemporal spike-centered averages (st-SCAs) after spatial filtering

The spatially filtered st-SCAs resemble similar patterns to non-whitened st-SCAs, albeit a smaller amplitude signal. Grayscale is in arbitrary units (A.U.).

4.3.3 Theoretical model of a macroelectrode

The st-SCA calculations presented above were obtained indirectly by an averaging procedure in order to reduce the noise not associated with the spike trigger in the spike-LFP relationship. In this section, we simulate an ideal noise-free, controlled environment where spatial and temporal relationships can be measured directly (Fig. 4.9).

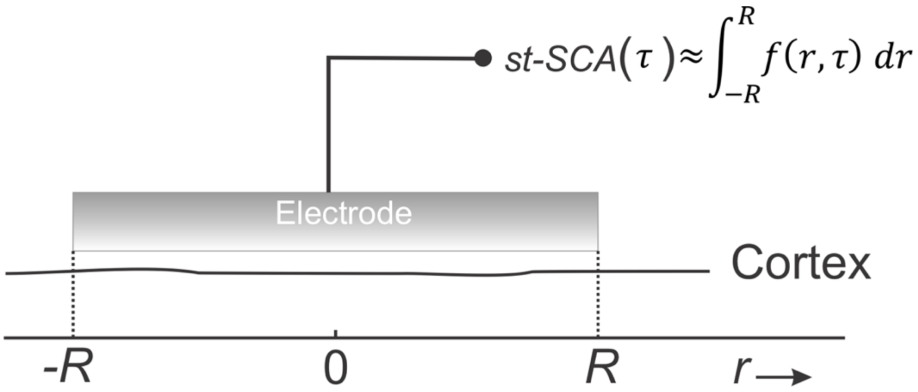

Figure 4.9. A mathematical model as represented by the recording of macroelectrode measuring the underlying network's st-SCA.
The electrode covers an area of one-dimensional cortex where we record the effect associated with a single, centrally located ictal action potential, $\delta(\mathrm{r}, \tau) = \delta(0,0)$; i.e., the macroelectrode measures the underlying network's temporal component of the st-SCA, $st - SCA_t(\tau)$. This measurement can be approximated by an unknown action potential's spatiotemporal cortical activation function, $f(r, \tau)$, integrated over the spatial range $[-R, R]$ covered by the electrode.

Here, the sum of all measurements across the MEA can be represented by a single macroelectrode, which records cortical activity when a spike occurs at time zero and at the center of the electrode. This is a measurement of the noise-free, spatiotemporal local field function $f(r, \tau)$ (space (r) and time (τ)) associated with the central spike represented by a delta function, $\delta(r, \tau)$. Because the potential of cortical generators attenuates sharply with distance, we consider contributions from activity in areas not directly under the macroscopic electrode to be negligible.

Under this assumption, the electrode's signal can be approximated by summing the contributions over the neocortical area under the electrode, and we find the following expression for $STA(\tau)$:

$$STA(\tau) \approx \int_{-R}^{R} f(r,\tau)\, dr \;=\; \int_{-\infty}^{\infty} rect(-R,R)\, f(r,\tau)\, dr \tag{4.4}$$

with $rect(-R,R)$ representing a rectangular window bounded by $[-R,R]$. Similarly, if we compute the spatial component of the SCA, $st\text{-}SCA_s(r)$, by integration over a fixed time epoch, $[-T,T]$, around the seizure onset, we get:

$$st\text{-}SCA_s(r) = \int_{-T}^{T} f(r,\tau) dt \;=\; \int_{-\infty}^{\infty} rect(-T,T) f(r,\tau) d\tau \tag{4.5}$$

Because the action potential can be represented by a unit impulse, $STA(\tau)$ and $st\text{-}SCA_s(r)$ are equivalent to a cortical unit impulse response (UIR). Thus, the UIR can be used to link the spike train to the associated LFP.[2] In most cases the function $f(r,\tau)$ cannot be simply derived from measuring the $STA(\tau)$ and $st\text{-}SCA_s(r)$, but one could apply an *ad hoc* solution so that Eqs. 4.4 and 4.5 produce the correct characterization:

$$f(r,\tau) \propto st\text{-}SCA_s(r) STA(\tau) \tag{4.6}$$

In special cases, however, $f(r,\tau)$ may be mathematically derived. Note that we determined earlier that in three of five patients with recordings in the recruited territory, the $STA(\tau)$ resembles a sinc-function:

$$STA(\tau) \;\propto\; sinc(\tau) \tag{4.7}$$

---

[2] A detailed stepwise explanation of how action potentials and LFP can be represented as the inputs and outputs of a linear time invariant (LTI) system can be found in the supplementary section of this chapter (section 4.6).

This represents a unique scenario in which the $f(r,\tau)$ and $st\text{-}SCA_s(r)$ may be predicted from the characterization of $STA(\tau)$ alone. The sinc-function is the UIR of an ideal filter, and a previous study has used this property to show that an ictal spike train passed through an ideal filter recreates the seizure's LFP (Eissa et al., 2018). Since the sinc-function is defined as the Fourier transform of a rectangular function, the relationship between time and space conveniently parallels a time-frequency Fourier-transform-pair. Accordingly, we find:

$$f(r,\tau) \propto e^{jr\tau} \tag{4.8}$$

Substitution of this finding into Eq. 5 enables us to find the $st\text{-}SCA_s(r)$, which represents the spatial postsynaptic effects of an action potential effective over a fixed time epoch around the seizure onset ($[-T,T]$):

$$st\text{-}SCA_s(r) \propto \int_{-\infty}^{\infty} rect(-T,T)\, e^{jr\tau} d\tau \;=\; sinc(r) \tag{4.9}$$

Thus, we find that in the special case where both $STA(\tau)$ and $st\text{-}SCA_s(r)$ are described by sinc-functions, the temporal features of the spike-associated LFP can predict the spatial features, and vice versa.

4.3.4 Quantification of the st-SCA spatial patterns

Since the model showed that a sinc-function in the temporal domain predicts a sinc-function in the spatial domain, we aimed to more quantitatively describe the donut-shaped activity observed in Fig. 4.4C. Taking advantage of the radial symmetry observed in the st-SCA, we converted the Cartesian coordinates (ξ,ψ) into polar coordinates (r,θ) and focused on the spatial relationship with respect to r (Fig. 4.10A). This enabled us to depict the st-SCA in two dimensions, (r, τ) (Fig. 4.10B). A detail of that relationship is depicted in Figure 4.10C, and the summed values across this two-dimensional detail are plotted along its margins. These summed values are the two components as a function of space and time (r and τ). Note that the bottom graph in Figure 4.10C represents the central trough ($\tau = \pm 35$ms) of the function shown in Figure 4.4A. As anticipated by the outcome in Eq. 4.9, we observed a spatial component that shows a central trough with smaller amplitude side lobes (Fig. 4.10C, left trace) –a pattern consistent with the shape of a sinc-function. Note that the resolution and range of the spatial component ($r = \pm 3.6$mm) is limited by the size of the MEA (Fig. 4.1B). Consistent with the donut-shaped rings observed in Figure 4.4C, the peaks of the spatial component were separated by ~2.5mm (Fig. 4.10C, left trace, blue arrows).

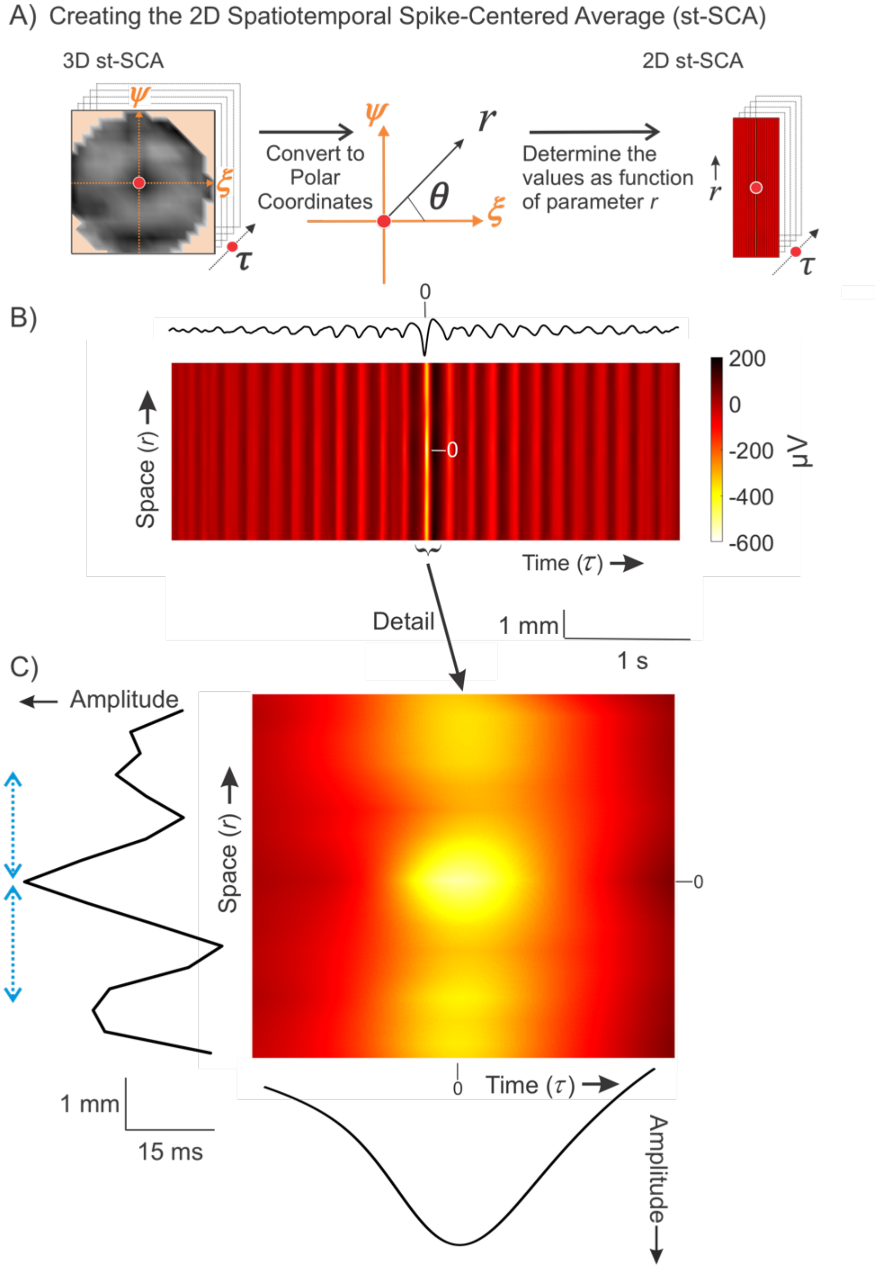

Figure 4.10. The 2D spatiotemporal spike-centered average for Patient 1.

(A) The Cartesian coordinates (ξ, ψ) from the 3D st-SCA are converted into polar coordinates (r, θ), resulting in a 2D st-SCA.

(B) A color representation of $st\text{-}SCA(r, \tau)$. The top trace, the temporal component of the $st\text{-}SCA_t(\tau)$, is obtained by the sum of $st\text{-}SCA(r, \tau)$ over r. Amplitude and color scale are in μV.

(C) Detail of the central part of Panel B. The left margin shows the resulting wave from summation over time, generating the spatial component of st-SCA. The green arrows on the left indicate the distance (~2.5mm) between the peaks seen in this function. The bottom margin depicts the resulting wave from summation over space, generating the temporal component of the st-SCA.

4.4 Discussion

The neural dynamics of human focal seizures show a complex relationship between action potential activity and the LFP (Movie S1). Because characterizing this relationship is important for understanding seizure generation and propagation, this study aimed to determine the spatiotemporal patterns observed across seizure states and cortical locations. Analyses of clinical recordings (Fig. 4.2-4.5) showed that the spike-LFP relationship for some focal seizures can be approximated by a sinc-function in both the spatial and temporal domains. Our theoretical model (Eq. 4.4-4.9; Fig. 4.9) further showed that a sinc-function in the temporal domain can predict a sinc-function in the spatial domain. Here, we discuss the potential biological implications of our findings.

Under physiological conditions, synaptic activity is a major contributor to the extracellular potential field (Nunez et al., 2006). Other contributors may include intrinsic membrane currents, gap junctions, neuron-glia interactions, and ephaptic effects (Buzsaki et al., 2012; Herreras, 2016). While the relative contributions of these different mechanisms during pathological states such as seizures have not been fully elucidated, a non-zero cross-correlation between action potentials and LFPs is expected because synaptic currents are a major component in the compound activities observed in ictal states.

In our discussion of the mechanistic implications of the observed st-SCAs, we assign a net excitation to negative deflections and net inhibition to positive deflections, as previously described (Eissa et al., 2017). Accordingly, our st-SCA analyses (Fig. 4.2, 4.3) show that in the recruited ictal territory, the spike-LFP correlation at small lags are dominated by net excitation during seizures in all patients. The activity level in the excitatory center, representing the activity at the ictal wave, is excessively high, possibly due to saturation of the local inhibitory population (Tryba et al., 2019). In Patients 1 and 2, we also observe a ring of reduced excitation at a distance ~1.5mm around the excitatory center (Fig. 4.4C, 4.3A-B). In turn, the ring of reduced excitation is surrounded by a second ring at an additional distance of ~1mm where excitation increases again.

For these patients, this donut-shaped st-SCA is specific to the recruited seizure territory in the ictal phase (Fig. 4.5A, B). This observation suggests that the ictal wave in the recruited territory, represented by the excitatory center ($\xi, \psi = 0{,}0$), creates an escape of hyperexcitation via a jump that engages mid-range connectivity in the millimeter range (Fig. 4.4C, 4.10C). Decorrelation of the LFP prior to the st-SCA calculations yielded similar spatiotemporal patterns (Fig. 4.8), further corroborating the importance of local mm-range excitatory connections in focal seizures.

A question that remains is the biological basis for this connectivity. Histological studies have shown that there are indeed excitatory mid-range connections at the millimeter scale mediated by axon collaterals within the gray matter in the neocortex in addition to short-range excitatory and inhibitory connections at a scale of hundreds of μm (Fig. 4.11A) (Nieuwenhuys, 1994; Oberlaender et al., 2011; Pichon et al., 2012; Zhang & Deschênes, 1997). Additionally, previous studies of ictal wave dynamics provide direct evidence that mm-range connections are invoked during seizure activity (Schevon et al., 2012). An example of this jump in action potential activity is depicted in the spatial plot in Figure 4.11B, in which there are multiple areas of simultaneously increased neural activity across the MEA, separated by mm-range gaps. This is consistent with the distance between the excitatory center and outer ring we observe in the donut-shaped spatial cross-correlation depicted in Figure 4.4C. This pathological escape of uncontrolled excitation across the cortex could be considered a candidate mechanism in seizure recruitment and propagation.

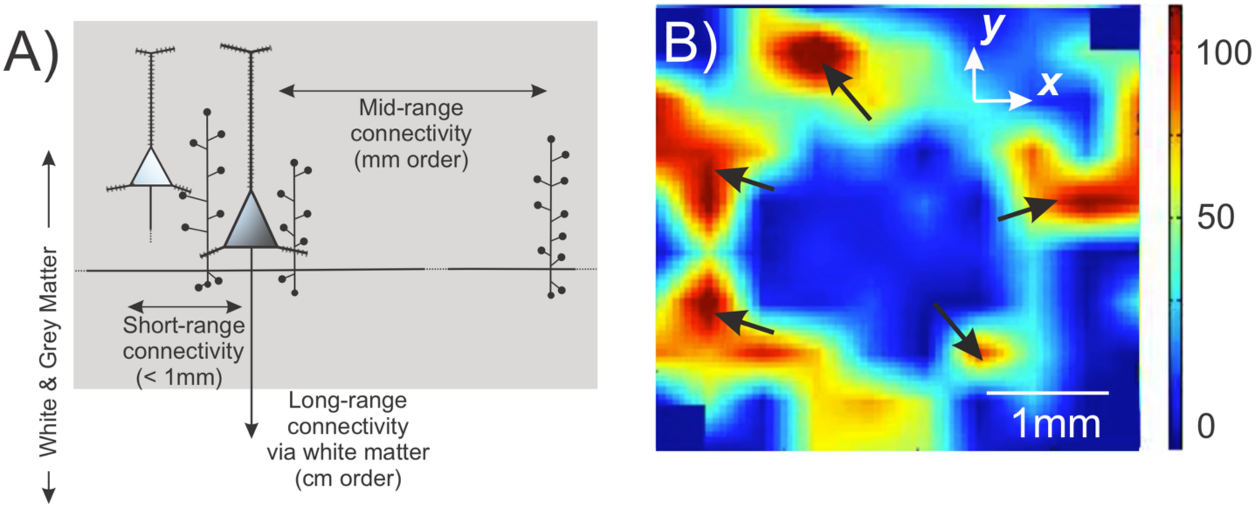

Figure 4.11. The propagation of the ictal wavefront and the involvement of mid-range excitatory neocortical connectivity by axon collaterals.
(A) Diagram of gray matter excitatory connections of a neocortical pyramidal cell showing the short-range connections (order of 100s of µm) and mid-range connections (order of mm) via the pyramidal cell axon collaterals (based on Figure 5 in Nieuwenhuys, 1994).
(B) A snapshot of a video (see Supplement) showing the propagation of ictal, multi-unit action potentials across part of a Utah array. The black arrows show multiple contiguously active areas that are separated by a mid-range, mm-sized distance, supporting that the excitatory axon collateral connections are invoked for propagation of the ictal activity. Color scale represents the number of spikes per second.

By combining current and previous findings on ictal dynamics, we can outline the following summary for an evolving, neocortical focal seizure. At the micro and meso-scales, an ictal wave of action potential activity propagates at a velocity of ~1 mm/s by invoking excitation via the local connections over distances < 1 mm. This wave of hyperexcitation propagates locally when the inhibition in front of this wave fails to constrain the excitation (Eissa et al., 2017; Schevon et al., 2012; Tryba et al., 2019). In this context, it is interesting to note that this propagation process seems compatible with the evolution of the clinically observed Jacksonian march first described by Hughlings Jackson in 1870 (Extercatte et al., 2015). We now find evidence that, in addition to the slow propagation process, the ictal wave excites cortical areas farther than 1 mm away, probably via axon collaterals within the gray matter, which allows excitation to 'escape,' and enables recruitment of additional cortical territory. This activation of areas > 1 mm away might also explain modular propagation of ictal activity, a property previously observed in experimental seizures (Trevelyan et al., 2006). At the macro-scale, white matter, intracortical connections are invoked, spreading ictal activity across a cm-sized territory. The activity in this macroscale territory is still highly correlated with the action potential activity in the ictal wave located in the recruited territory rather than the local action potential activity located in the non-recruited areas (Fig. 4.6) (Eissa et al., 2017). In addition, while local inhibition fails at the ictal wavefront, longer range inhibition remains intact and plays a critical role in sustaining the synchronous oscillatory component of the ongoing seizure at the macroscale (Eissa et al., 2017; Eissa et al., 2018).

Not all patients with implants in recruited territory showed spatiotemporal patterns resembling a sinc-function, and the clinical etiologies for these patients may offer some clues about why this is the case. The diffuse depressions observed in the spatial domains for both Patients 4 and 5 (Fig. 4.3D-E, 4.4D) are consistent with a local flood of excitation. Indeed, the seizures in both of these patients were characterized as secondarily generalized. This suggests that in generalized seizures, the mid-range excitatory connectivity structure (as represented by the sinc-function) may play a diminished role in comparison to other mechanisms of ictal propagation, such as local excitation or engagement of white matter tracts (Fig. 4.11A). Furthermore, a unique case is Patient 3, who was diagnosed with cortical dysplasia. The STA is sinc-like, and the st-SCA partially resembles a sinc-function (Fig. 4.3C). Cortical dysplasias have been shown to be associated with functional connectivity defects (Hong et al., 2017; Jeong et al., 2014; Rezayev et al., 2018) which may explain the partial donut ring of activity in the st-STA (Fig. 4.3C).

From these results, we propose that focal seizures that engage mid-range, excitatory circuits may be identified by their spike-LFP spatiotemporal patterns. With this information, clinicians can potentially target specific mechanisms underlying a patient's seizures and choose appropriate therapeutic strategies. For example, removal of horizontal interactions on a mm-scale has been the rationale for performing subpial transections in patients with intractable epilepsy (Morrel et al., 1989). In these cases, characterization of the st-SCA may inform the appropriateness of such interventions in personalized patient treatment plans.

In addition, our results suggest that these spatiotemporal patterns may be obtained without the use of MEAs. While MEAs are advantageous for monitoring and studying seizure activity with high temporal and spatial resolution, their current clinical utility is limited as they cannot be easily used to sample from multiple cortical areas. Our theoretical model, however, showed that a sinc-function in the temporal domain can predict the presence of a donut-shaped ring of activity in the spatial domain. Consequently, a clinician could hypothesize that mid-range excitatory connections may be involved during a patient's focal seizure if a sinc-function is observed in the temporal domain. Interestingly, we found that the sinc-function can be characterized in the temporal domain by using spiking and LFP information from a random subset of only eight electrodes (Fig. 4.12). This suggests that the st-SCA may be characterized by using neocortical microelectrodes that allow for recording from multiple areas by reducing the number of channels per probe. The development of such electrodes is technologically feasible as similar probes are already used clinically for the monitoring of deep brain structures (Misra et al., 2014).

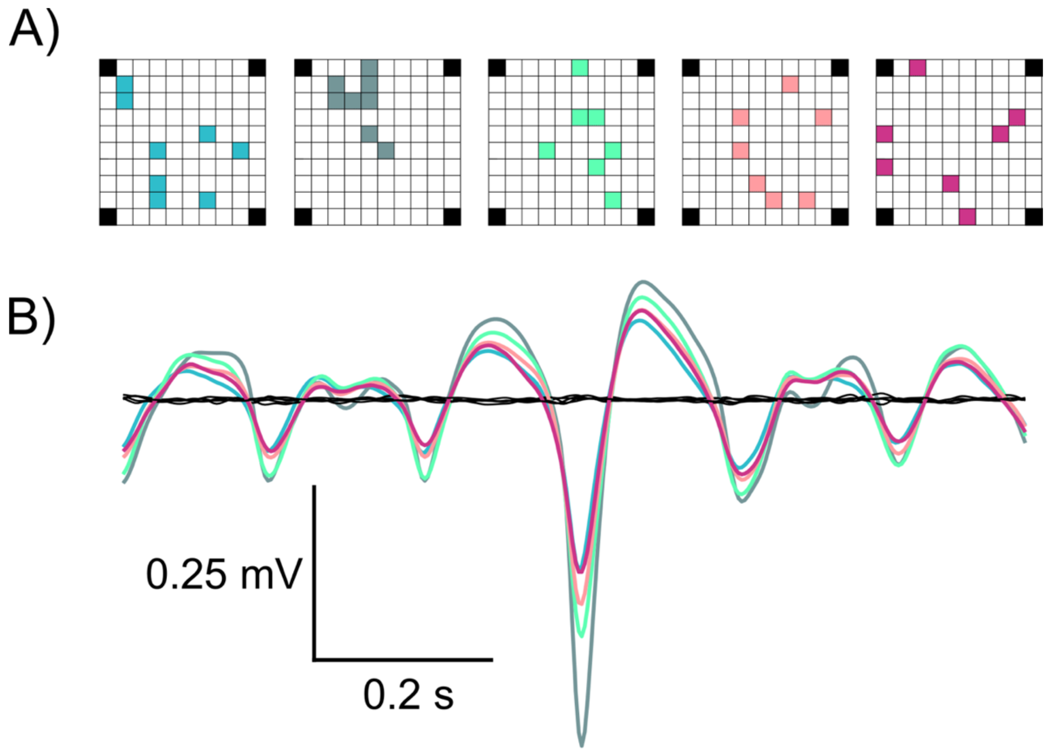

Figure 4.12. The spike-triggered average (STA) calculated from spike timing and LFP activity from only a random subset of eight electrodes for Patient 1.
The sinc-function may be characterized in the temporal domain using signals from only eight channels across the MEA. The different colors in **(A)** represent different random subset of eight electrodes, and their corresponding STA in **(B)**.

4.5 Methods[3]

4.5.1 Patients

Seven patients with pharmacoresistant focal epilepsy underwent chronic intracranial EEG studies to help identify the epileptogenic zone for subsequent removal. Patients 1, 4, 6, and 7 were recruited at Columbia University Medical Center, and Patients 2, 3, and 5 were recruited from Massachusetts General Hospital/Brigham and Women's Hospitals (Table 4.1). Procedures were approved by the Internal Review Board committees at Columbia University Medical Center, The University of Chicago Comer Children's Hospital, and Massachusetts General Hospital/Brigham and Women's Hospitals. The patients' surgeries and treatment plans were not directed by or altered as a result of these studies.

4.5.2 Signal acquisition and pre-processing

A 96-channel, 4 x 4mm MEA (Utah array; Blackrock Microsystems) was implanted along with subdural electrodes (ECoG) with the goal of recording from seizure onset sites. Additional details of study enrollment and surgical procedures have been previously published (Schevon et al., 2012; Truccolo et al., 2014). Signals from the MEA were acquired continuously at a sample rate of 30 kHz per channel (0.3-7500Hz bandpass, 16-bit precision, range ±8 mV). The reference was epidural. Up to three seizures from each patient were selected for detailed analysis to avoid biasing the dataset from the patients from whom many seizures were recorded. Seizure recordings were categorized as recruited or unrecruited territory using previously described methods (Schevon et al., 2012). Channels and time periods with excessive artifact or low signal-to-noise ratio were excluded.

Unit activity was identified using filtered 0.3-3kHz signals with spikes defined as deflections ≥4 standard deviations below the mean. The low frequency component of the local

---

[3] Custom scripts used to generate the results presented in this chapter can be found at https://github.com/sominlee14/stSCA_scripts (Appendix).

field potential (LFP) activity across the array was created by averaging the artifact-free LFP activity from all micro-electrode signals filtered 2-50Hz. The averaged LFP procedure has been shown to generate signals that are representative of and comparable to nearby electrocorticography signals (Eissa et al., 2017; Eissa et al., 2018).

4.5.3 Spatiotemporal spike-centered average (st-SCA) calculations and signal analysis

All signal processing and statistical analyses were performed in MATLAB (MATLAB, Natick, MA, USA). The st-SCA was determined as follows: first, as previously described (Eissa et al., 2017; Eissa et al., 2018), we detected the spikes in the multi-unit activity. Next, we collected the spatiotemporal data around each spike and translated the time and position of all associated LFPs relative to each spike's time and position (Fig. 4.1). Finally, we summed all translated data and computed the average at each time and position by dividing the sum by its number of contributions. Note that this position-dependent average is necessary because not every position receives the same number of contributions during the translation of the LFP's axes.

Evidence of radial symmetry of the st-SCA (Fig. 4.4C) allowed conversion from Cartesian coordinates (ξ, ψ) to polar coordinates (r, θ). By ignoring the minor deviations from radial symmetry, we focused on the spatial component of the st-SCA with respect to r (Fig. 4.10A), which enabled us to depict the spatiotemporal properties in two dimensions (Fig. 4.10B). Furthermore, if we compute the sum across space, we obtain purely the temporal component of the st-SCA, which is equivalent to the STA. Similarly, summation over time τ generates the spatial component of the st-SCA. With these results, we can assess to what extent our model of the ictal network, a linear time-invariant (LTI) system with unit impulse response $C(\tau) \propto sinc(r, \tau)$, fits the data. The following is a stepwise description of this method:

1. Each broadband signal of the 10×10 MEA was bandpass filtered for the low frequency component (2-50Hz) of the local field potential (LFP) and for spike detection (0.3–3kHz).

2. Spikes were detected in the multi-unit activity as negative deflections that exceeded four standard deviations of the filtered signal. A complete list of spike detection results can be found in Table 4.2.
3. For each spike, the 10×10 frames of the LFP data were collected for $\pm n$ sample times representing ±5s around the spike time, and the timescale of the frames was set such that the spike occurred at time zero, $\tau = 0$.
4. All LFP frames associated with a single spike were translated such that the spike location was at the origin of the new spatial coordinate system $\xi, \psi = 0{,}0$. Note that this spatial translation is necessarily spike specific because spikes do occur at different locations.
5. Next, the translated $10 \times 10 \times (2n + 1)$ frames were put into a three dimensional $19 \times 19 \ \times (2n + 1)$ configuration with the spatiotemporal origin $(\xi, \psi, \tau = 0{,}0{,}0)$ is at position $10{,}10, n + 1$. This step was done to keep the LFP frames compatible across spikes.
6. For each spike, these frames were summed into a three dimensional $19 \times 19 \times (2n + 1)$ matrix.
7. For each position in the $19 \times 19 \times (2n + 1)$ matrix, the total number of contributions N was counted.
8. Finally, to obtain the spatiotemporal cross-correlation, the sum obtained in step 6 was divided by the N obtained in step 7 for each position. This resulted in the discrete spatiotemporal estimate of $C(\xi, \psi, \tau)$, as shown in Eq. 4.3.

Table 4.2. Patient Table: Seizure recording and spike detection information

	Epoch Length (sec)	n spikes*	spikes/s*
PATIENT 1			
Interictal	180	7720	43
Seizure 1	58	78479	1353
Seizure 2	80	77788	972
Seizure 3	102	153063	1501
PATIENT 2			
Interictal	180	181116	1006
Seizure 1	29	110896	3824
PATIENT 3			
Interictal	180	16582	92
Seizure 1	52	162707	3129
Seizure 2	88	274656	3121
Seizure 3	57	193733	3399
PATIENT 4			
Interictal**	180	23881	133
Seizure 1	82	385978	4707
Seizure 2	102	366705	3595
Seizure 3	96.23	322148	3348
PATIENT 5			
Interictal	180	52998	294
Seizure 1	102	304058	2981
Seizure 2	101	314402	3113
Seizure 3	73	349189	4783
PATIENT 6			
Interictal	180	24438	136
Seizure 1	12	3471	289
Seizure 2	13	4902	377
Seizure 3	6	1635	273
PATIENT 7			
Seizure 1	20	17157	858
Seizure 2	23	7778	338
Seizure 3	31	7065	228

*Across all channels of the MEA.

**Due to limitations in available recordings, this interictal clip is 12 minutes away from the nearest known ictal activity.

4.5.4 Spatial filtering

For calculations involving the spatial filtering of LFP signals, we applied the spatial whitening process as described in Hyvärinen et al. (2001) and Telenczuk et al. (2017). As previously published, a signal is spatially filtered by matrix multiplication with a whitening matrix $\boldsymbol{W}$, where $\boldsymbol{W}$ is the inverse square root of the signal's covariance matrix, $\boldsymbol{C}$:

$$\boldsymbol{W} = \boldsymbol{C}_{signal}^{-1/2} = \boldsymbol{E}\boldsymbol{D}^{-1/2}\boldsymbol{E}^{T} \tag{4.10}$$

where $\boldsymbol{E}$ is a matrix of eigenvectors of $\boldsymbol{C}_{signal}$, and $\boldsymbol{D}$ is a diagonal matrix with inverse square roots of eigenvalues $\lambda_i$on its diagonal, such that $\boldsymbol{D}_{ii} = \frac{1}{\lambda_i}$ and $\boldsymbol{D}_{ij} = 0$ (Telenczuk et al., 2017). In this study, the signals being transformed were the MEA channel signals bandpass filtered at 2-50Hz.

4.5.5 *Noise estimation*

To evaluate the signal-to-noise ratio (SNR) of the averaged results, we estimated the residual noise using the plus-minus averaging approach. We implemented this by employing the above eight steps while keeping two three-dimensional 19 × 19 matrices: one summed the even contributions for each location and the other summed the odd ones. To obtain the averages for the odd and even components, each position in the matrix was then divided by its number of contributions. The sum of the even and odd averages is the same result obtained in step 8 above. In contrast, the difference between the even and odd averages cancels the consistent component (i.e., the signal) while preserving the random noise estimate (4). The SNR was estimated by computing the root mean square (rms) of the signals and the rms of their noise estimates, leading to a signal-to-noise ratio calculated by:

$$SNR = 20\, log\left(\frac{rms_{signal}}{rms_{noise}}\right) \text{dB} \tag{4.11}$$

Average ratios for the st-SCAs across space and time all were >30dB (Fig. 4.13).

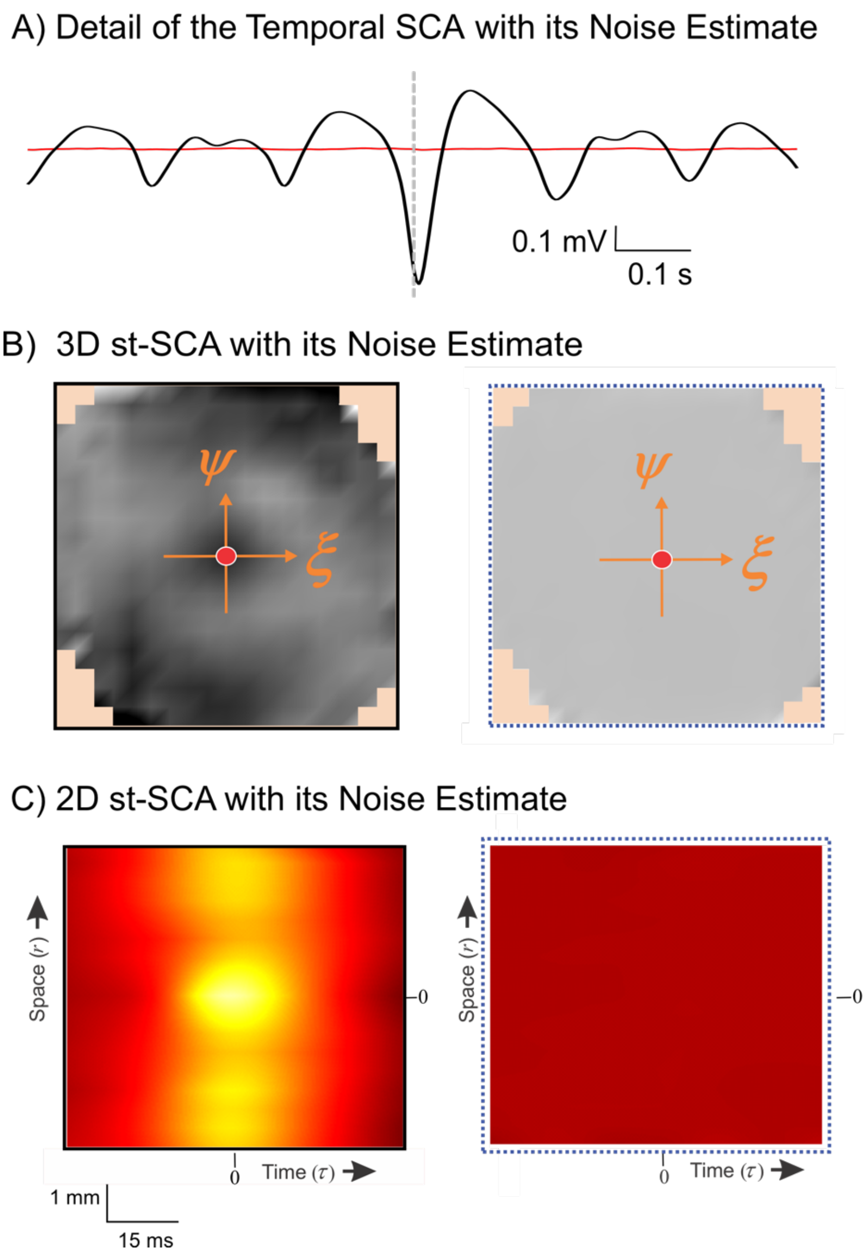

Figure 4.13. Representative noise estimates of the spatiotemporal spike-centered average (st-SCA) for Patient 1.

(A) Detail of the temporal component of the st-SCA from Figure 4.4A (black) and its noise estimate (red). The signal-to-noise ratio (SNR) of the depicted data is 45dB.

(B) The spatial component of the st-SCA depicted in Figure 4.4C (left) and its estimated noise component (right). The location specific SNR of the depicted data range is 26 – 80dB, with an average of 38dB. The units for the grayscale are identical for both maps and identical to the scale in Figure 4.4.

(C) The 2D st-SCA from Figure 4.10C (left) and its noise estimate (right). The SNR of the depicted data is 39dB. The units for the color scale are identical for both maps and the same as in Figure 4.10.

4.6 Supplementary information

Spikes and local field potentials as inputs and outputs to a linear time invariant (LTI) system

Computation of the spatiotemporal spike-centered average (st-SCA) using ictal recordings presents a challenge because the occurrence of action potentials across a seizing network is not experimentally controlled, unlike the scenario in which the location and timing of the neuronal activities are evoked by external stimuli. The derivation presented below addresses this problem and demonstrates that the st-SCA is a spatiotemporal analog of the well-known spike-triggered average (STA).

For convenience, we repeat here that (x, y, t) are the spatiotemporal components of the signals; (x_i, y_i, t_i) are the spatiotemporal coordinates of spike i and (ξ, ψ, τ) are the spatiotemporal components of the signal relative to the spike. Using a similar approach as in (Eissa et al., 2018), we now extend the model of the ictal network as a linear time invariant (LTI) system with the multi-unit action potential activity as input, the LFP as its output, and the network's unit impulse response (UIR) defined as the LFP associated with a single unit impulse (δ):

$$UIR = st\text{-}SCA \; = C(\xi, \psi, \tau) \tag{4.12}$$

We now can recover the network output Z using the convolution of the UIR and the network's input, i.e., the spikes:

$$Z \; = \iiint C(\xi, \psi, \tau) \left\{ \frac{1}{N} \sum_{i=1}^{N} \delta(x - x_i - \xi, y - y_i - \psi, t - t_i - \tau) \right\} d\xi \; d\psi \; d\tau \tag{4.13}$$

Note that we used the $\frac{1}{N}$ scaled version of the input here. Plugging in the expression for $C(\xi, \psi, \tau)$ results in:

$$Z = \iiint \left\{\frac{1}{N}\sum_{i=1}^{N} LFP(x_i + \xi, y_i + \psi, t_i + \tau)\right\}\ldots$$

$$\ldots\left\{\frac{1}{N}\sum_{i=1}^{N} \delta(x - x_i - \xi, y - y_i - \psi, t - t_i - \tau)\right\} d\xi\, d\psi\, d\tau \qquad (4.14)$$

Exchange of the summation and integration operations and evaluation of the triple integral gives the model's estimate of the spatiotemporal LFP from the LTI system:

$$Z = \frac{1}{N^2}\sum_{i=1}^{N}\sum_{i=1}^{N} LFP(x, y, t) \; = \; LFP(x, y, t) \qquad (4.15)$$

As shown in Eissa et al. (2018), the time domain component of this linear estimate produces a close approximation of the ongoing seizure activity with significant correlation ($p < 0.01$) between recorded and estimated activity.

CHAPTER 5

CONCLUSIONS

5.1 Summary of thesis work

On my first day of work after deciding to join an EEG analysis lab, I naively pointed to an EEG recording open on my advisor's desktop and asked,

"So, what does this EEG mean?"

"Great question. Why don't you look into it?" was his reply.

At the time, I found his response annoying but in hindsight I can appreciate its depth. At its core, this thesis grapples with this ostensibly simple question I had on my first day: When we read an EEG, exactly what are we looking at?

To address this question, studies presented in Chapter 2-4 approached the following three questions from different angles:

(1) How do seizure dynamics change across spatial and temporal scales?
(2) How do these dynamics manifest in recorded EEG signals?
(3) What may be the biological mechanisms underlying these dynamics?

In Chapter 2, I presented a study that used interictal recordings obtained with scalp EEG and intracranial depth electrodes. This design allowed comparison between the intracranial and extracranial manifestations of epileptiform activity. The results showed that intracranially recorded hippocampal interictal discharges have correlates on scalp EEG. The tight temporal coupling between the scalp EEG and intracranial waveforms suggest that the scalp EEG manifestations are due to volume conduction of signals originating from the hippocampus. Furthermore, the features of these scalp correlates may allow differentiation between static and propagating discharges.

In Chapter 3, I presented an algorithm that allowed for digital reconstruction of low frequency activity that is attenuated by a high-pass filter. This digital reconstruction was performed with a deconvolution-based inverse filter that relied on characterizing the unit impulse response of an EEG recording system. I showed that this algorithm can be stably performed on seizures recordings obtained on clinical EEG machines. Application of this inverse filter to clinical ictal recordings obtained from temporal lobe epilepsy patients showed that infraslow activity is associated with the conventionally determined seizure onset zone. Furthermore, these reconstructions showed that the infraslow activity patterns may allow more unique characterization of the seizure onset zone compared to traditional methods.

In Chapter 4, I presented a spatiotemporal calculation that showed that the spiking activity in an ictal network was associated with various spatial patterns in the global local field potential (LFP). I also showed that this spike-LFP relationship has unique mathematical features that allow the temporal component to predict the spatial component, and vice versa. Furthermore, characterization of these spatial patterns allows differentiation of seizures that engage mesoscale networks from seizures that engage micro or macro level networks.

5.2 Bench to bedside: future directions

The ultimate goal of this research is to take the tools and insights presented in this thesis from the lab (bench) and translate them to improved care and outcomes for epilepsy patients (bedside). In this section, I discuss the questions that still need to be addressed and the potential clinical applications of the work presented in this thesis.

5.2.1 Understanding neural mechanisms underlying seizure generation

The research presented here focused on identification and characterization of electrographic features that expand the current repertoire of epileptiform activity. From these characterizations, we can make some informed hypotheses about their underlying mechanisms.

For example, in Chapter 2, I discussed how the rotating scalp marker may be more indicative of a propagating interictal discharge. In Chapter 4, I discuss the possibility that the spatiotemporal characteristics of the spike-associated LFP may reflect the engagement of midrange horizontal connections.

From these studies alone, however, it is difficult to ascertain the neural mechanisms that underlie these observations. To address this question, other experimental systems such as animal or computer modeling must be pursued. Human data, although interesting, makes it difficult to conduct experiments. In the face of this obstacle, computational modeling may be used to confirm (or refute) biological plausible explanations to explain particular electrographic features. Better understanding the mechanisms will help parse out which features are likely to be causative or correlative. Such an understanding would be important for improving EEG interpretation.

5.2.2 *Improving outcomes of epilepsy surgery*

Surgical treatment of epilepsy depends heavily on the concept of the epileptogenic zone (EZ), the putative source of seizure activity. It is formally defined as the minimum amount of tissue that can be resected to achieve seizure freedom (Rosenow & Lüders, 2001). This definition highlights the two opposing goals that are at a fine balance during neurosurgical interventions. If the procedure is to be curative, all of the epileptogenic tissue must be removed. On the other hand, the resection areas should be minimized to avoid potential loss of function. Thus, surgical planning may be improved in the following ways:

(1) *Improve identification of epileptogenic tissue*

One major way to improve surgical planning is to identify features that are unique to epileptogenic tissue. The results in this thesis point to the possibility that triangulating between several metrics may have the best chance at delineating a more accurate target for surgery. In Chapter 2, I presented data that showed that interictal discharges are very heterogeneous in nature and have different propagation patterns. Consequently, understanding how these patterns link to pathology may allow interictal discharges to become more valuable in surgical planning. In Chapter 3, I showed that infraslow activity has a more heterogeneous time course between electrodes than activity in the conventional clinical band (1-70Hz), suggesting that this feature may be used to identify a smaller set of electrodes that need to be resected. The current studies are correlative, meaning that while features such as ISA are observed in the SOZ, whether ISA is a true marker of the EZ remains unknown. Discerning the true utility of these biomarkers will rely on future prospective studies that can link these features to clinical outcomes.

(2) *Better identify patients who would benefit from resective or ablative procedures*

The results presented in Chapter 4 suggest that EEG techniques may be used to identify whether a patient's seizures engage microscale, mesoscale, or macroscale networks. The ability to identify these mechanisms in individual patients may be useful in determining what kind of procedure would most benefit the patient. If the seizure originates from a small, localized network, then resection of the area may be sensible. If a mesoscale network is involved, then an intervention such as subpial transections that disconnects mi-drange horizontal connections may be effective. The engagement of larger networks with long-range connections may be useful for indicating neuromodulation techniques such as RNS. Determining the efficacy of choosing specific interventions based on a patient's seizure network characteristics will require prospective studies that monitor surgical outcomes.

5.2.3 Improving epilepsy diagnostic and monitoring

Presurgical monitoring frequently requires invasive surgeries and long hospital stays. When invasive monitoring is indicated, patients undergo surgery for electrode implantation and must stay at the hospital until one or more seizures can be properly captured and characterized. There are two ways to improve this onerous process:

(1) Reduce the need for invasive monitoring by increasing the informative value of non-invasive EEG techniques.
(2) Decrease monitoring time by extracting more useful information from interictal recordings.

In Chapter 2, I showed that simultaneously recorded intracranial and extracranial signals may be used to better understand how seizure activity from deep sources manifest on scalp EEG. One of the future directions for this project is to develop a more complete understanding of the link between intracranially and extracranially recorded signals such that epileptiform activity may be inferred by looking at the scalp EEG alone. Furthermore, the ability to identify these scalp markers for TLE can increase sensitivity for scalp EEG in detecting TLE, which would allow for earlier diagnoses, ultimately reducing morbidity and mortality. Prospective studies must be done to see if these scalp markers truly have value in identifying TLE patients earlier in the course of the disease.

This project also showed that interictal data can be used to identify different morphologies of interictal discharges. A 2-hour recording from each patient was sufficient to capture enough interictal discharges to discern discharges with static versus propagating patterns. If these features could be linked directly to epileptogenicity, then interictal data would become much more valuable in surgical planning, and seizure monitoring times may be dramatically reduced. The results in Chapter 3 identify ISA as a marker of interest for seizure activity. It is possible that ISA may be observed in interictal periods as well, although this analysis has yet to be completed. The ability to use interictal ISA would also give more diagnostic value to interictal recordings and potentially reduce monitoring times.

Studying ISA also has potential for reducing invasive monitoring as low frequencies may be more obvious and better observed on the scalp, unlike high frequency oscillations, which has also become popular to study as a marker of the SOZ. HFOs require synchrony in microscale networks, and desynchronization at larger networks makes them unobservable at meso- to macroscales (Eissa et al., 2016). ISA, in comparison, tends to be much larger in amplitude and does not require high levels of synchronized spiking. Consequently, ISA may be more readily accessible than HFOs in the context of scalp recordings.

5.2.4 Automation of EEG interpretation

All of the markers and electrographic features of epileptiform activity discussed in this thesis were characterized quantitatively, and the analyses presented are algorithmic pipelines that are readily automated. The ability to use computational methods to identify epileptiform activity potentially has several clinical advantages:

(1) Reduction of clinical workload in EEG interpretation

EEG are often large datasets composed of hours to days to weeks of continuous data. The ability to better automate detection of seizure markers would potentially decrease the amount of EEG that needs to be manually read by a human reader.

(2) Increased sensitivity to epileptogenic markers

Algorithmic methods may be better suited to identifying seizure markers that are too subtle to be easily discerned by a human reader. Furthermore, human readers are subject to error due to lapses in attention and fatigue. Consequently, automating some of these tasks may be useful in decreasing human error.

(3) Increased consistency in EEG interpretation

A chronic issue to clinical EEG interpretation is that inter-rater variability tends to be very high, even amongst expert neurologists with subspecialty training in clinical neurophysiology (Jing et al., 2020). When multiple clinicians look at the same EEG, they can come to very different conclusions. Because patient treatment plans are dependent on EEG interpretation, a more quantitative approach to identifying seizure markers would for increased standardization in seizure assessments

5.3 Closing thoughts

No scientific story is ever truly complete, and epilepsy research is no exception. As is so often the case in science, it seems that each new finding spawns another dozen questions. This is perhaps best illustrated by the fact that a search in the PubMed database for “epilepsy” results in over 169,000 results.[1] Nearly half of those papers were published in the past ten years. In 2021 alone (even in the midst of the global COVID-19 pandemic), over 10,000 papers were published on the topic. We are all clearly working very hard.

The past several years, my advisor has frequently greeted me with,

“So, Somin, have you cured epilepsy yet?”

While I am sorry to say that I have not in fact cured epilepsy, I am happy to have contributed to the enormous amount of effort and resources expended by the scientific and medical community to better understanding this disease. I do hope that one day, I’ll be able to answer,

“Why yes, yes we have.”

---

[1] Search conducted June 7, 2022.

REFERENCES

Akiyama, T., McCoy, B., Go, C. Y., Ochi, A., Elliott, I. M., Akiyama, M., Donner, E. J., Weiss, S. K., Snead, O. C., 3rd, Rutka, J. T., Drake, J. M., & Otsubo, H. (2011). Focal resection of fast ripples on extraoperative intracranial EEG improves seizure outcome in pediatric epilepsy. *Epilepsia*, *52*(10), 1802-1811. https://doi.org/10.1111/j.1528-1167.2011.03199.x

Alarcon, G., Garcia Seoane, J. J., Binnie, C. D., Martin Miguel, M. C., Juler, J., Polkey, C. E., Elwes, R. D., & Ortiz Blasco, J. M. (1997). Origin and propagation of interictal discharges in the acute electrocorticogram. Implications for pathophysiology and surgical treatment of temporal lobe epilepsy. *Brain*, *120 (Pt 12)*, 2259-2282. https://doi.org/10.1093/brain/120.12.2259

Alarcon, G., Guy, C. N., Binnie, C. D., Walker, S. R., Elwes, R. D., & Polkey, C. E. (1994). Intracerebral propagation of interictal activity in partial epilepsy: implications for source localisation. *Journal of Neurology, Neurosurgery & Psychiatry*, *57*(4), 435-449. https://doi.org/10.1136/jnnp.57.4.435

Asadi-Pooya, A. A., Stewart, G. R., Abrams, D. J., & Sharan, A. (2017). Prevalence and Incidence of Drug-Resistant Mesial Temporal Lobe Epilepsy in the United States. *World Neurosurg*, *99*, 662-666. https://doi.org/10.1016/j.wneu.2016.12.074

Attal, Y., Bhattacharjee, M., Yelnik, J., Cottereau, B., Lefevre, J., Okada, Y., Bardinet, E., Chupin, M., & Baillet, S. (2007). Modeling and detecting deep brain activity with MEG & EEG. *Annu Int Conf IEEE Eng Med Biol Soc*, *2007*, 4937-4940. https://doi.org/10.1109/IEMBS.2007.4353448

Bazelot, M., Dinocourt, C., Cohen, I., & Miles, R. (2010). Unitary inhibitory field potentials in the CA3 region of rat hippocampus. *J Physiol*, *588*(Pt 12), 2077-2090. https://doi.org/10.1113/jphysiol.2009.185918

Berg, A. T. (2004). Understanding the delay before epilepsy surgery: who develops intractable focal epilepsy and when? *CNS Spectr*, *9*(2), 136-144. https://doi.org/10.1017/s109285290000849x

Berg, A. T. (2008). The natural history of mesial temporal lobe epilepsy. *Curr Opin Neurol*, *21*(2), 173-178. https://doi.org/10.1097/WCO.0b013e3282f36ccd

Berger, H. (1929). Über das Elektrenkephalogramm des Menschen. *Archiv für Psychiatrie und Nervenkrankheiten*, *87*(1), 527-570. https://doi.org/10.1007/BF01797193

Blair, R. D. (2012). Temporal lobe epilepsy semiology. *Epilepsy Res Treat*, *2012*, 751510. https://doi.org/10.1155/2012/751510

Bonaccini Calia, A., Masvidal-Codina, E., Smith, T. M., Schafer, N., Rathore, D., Rodriguez-Lucas, E., Illa, X., De la Cruz, J. M., Del Corro, E., Prats-Alfonso, E., Viana, D., Bousquet, J., Hebert, C., Martinez-Aguilar, J., Sperling, J. R., Drummond, M., Halder, A., Dodd, A., Barr, K., . . . Garrido, J. A. (2022). Full-bandwidth electrophysiology of seizures and epileptiform activity enabled by flexible graphene microtransistor depth neural probes. *Nat Nanotechnol*, *17*(3), 301-309. https://doi.org/10.1038/s41565-021-01041-9

Bower, M. R., Stead, M., Meyer, F. B., Marsh, W. R., & Worrell, G. A. (2012). Spatiotemporal neuronal correlates of seizure generation in focal epilepsy. *Epilepsia*, *53*(5), 807-816. https://doi.org/10.1111/j.1528-1167.2012.03417.x

Britton, J. W., Frey, L. C., Hopp, J. L., Korb, P., Koubeissi, M. Z., Lievens, W. E., Pestana-Knight, E. M., & St. Louis, E. K. (2016). In E. K. St. Louis & L. C. Frey (Eds.), *Electroencephalography (EEG): An Introductory Text and Atlas of Normal and Abnormal Findings in Adults, Children, and Infants*.

Buzsaki, G., Anastassiou, C. A., & Koch, C. (2012). The origin of extracellular fields and currents--EEG, ECoG, LFP and spikes. *Nat Rev Neurosci*, *13*(6), 407-420. https://doi.org/10.1038/nrn3241

Cendes, F. (2022). Neocortical temporal lobe seizures. https://www.medlink.com/articles/neocortical-temporal-lobe-seizures

Chen, Z., Issa, N. P., Wu, S., Liu, X., Sun, T., Bodnya, J., Rose, S., & Tao, J. X. (2020). The clinical significance of small sharp spikes: A retrospective study of 909 patients in epilepsy monitoring unit. *Epilepsy Res*, *168*, 106477. https://doi.org/10.1016/j.eplepsyres.2020.106477

Chowdhury, F. A., Silva, R., Whatley, B., & Walker, M. C. (2021). Localisation in focal epilepsy: a practical guide. *Pract Neurol*, *21*(6), 481-491. https://doi.org/10.1136/practneurol-2019-002341

Conrad, E. C., Tomlinson, S. B., Wong, J. N., Oechsel, K. F., Shinohara, R. T., Litt, B., Davis, K. A., & Marsh, E. D. (2020). Spatial distribution of interictal spikes fluctuates over time and localizes seizure onset. *Brain*, *143*(2), 554-569. https://doi.org/10.1093/brain/awz386

de Tisi, J., Bell, G. S., Peacock, J. L., McEvoy, A. W., Harkness, W. F. J., Sander, J. W., & Duncan, J. S. (2011). The long-term outcome of adult epilepsy surgery, patterns of seizure remission, and relapse: a cohort study. *The Lancet*, *378*(9800), 1388-1395. https://doi.org/10.1016/s0140-6736(11)60890-8

Delorme, A., & Makeig, S. (2004). EEGLAB: an open source toolbox for analysis of single-trial EEG dynamics including independent component analysis. *J Neurosci Methods*, *134*(1), 9-21. https://doi.org/10.1016/j.jneumeth.2003.10.009

Diehl, B., & Lüders, H. O. (2000). Temporal lobe epilepsy: when are invasive recordings needed? *Epilepsia*, *41 Suppl 3*, S61-74. https://doi.org/10.1111/j.1528-1157.2000.tb01536.x

Drazkowski, J. (2007). An overview of epilepsy and driving. *Epilepsia*, *48 Suppl 9*, 10-12. https://doi.org/10.1111/j.1528-1167.2007.01392.x

Dubey, A., & Ray, S. (2019). Cortical Electrocorticogram (ECoG) Is a Local Signal. *J Neurosci*, *39*(22), 4299-4311. https://doi.org/10.1523/JNEUROSCI.2917-18.2019

Dworetzky, B. A., & Reinsberger, C. (2011). The role of the interictal EEG in selecting candidates for resective epilepsy surgery. *Epilepsy Behav*, *20*(2), 167-171. https://doi.org/10.1016/j.yebeh.2010.08.025

Eissa, T. L., Dijkstra, K., Brune, C., Emerson, R. G., van Putten, M., Goodman, R. R., McKhann, G. M., Jr., Schevon, C. A., van Drongelen, W., & van Gils, S. A. (2017). Cross-scale effects of neural interactions during human neocortical seizure activity. *Proc Natl Acad Sci U S A*, *114*(40), 10761-10766. https://doi.org/10.1073/pnas.1702490114

Eissa, T. L., Schevon, C. A., Emerson, R. G., McKhann, G. M., Jr., Goodman, R. R., & Van Drongelen, W. (2018). The Relationship Between Ictal Multi-Unit Activity and the Electrocorticogram. *Int J Neural Syst*, *28*(10), 1850027. https://doi.org/10.1142/S0129065718500272

Eissa, T. L., Tryba, A. K., Marcuccilli, C. J., Ben-Mabrouk, F., Smith, E. H., Lew, S. M., Goodman, R. R., McKhann, G. M., Jr., Frim, D. M., Pesce, L. L., Kohrman, M. H., Emerson, R. G., Schevon, C. A., & van Drongelen, W. (2016). Multiscale Aspects of Generation of High-Gamma Activity during Seizures in Human Neocortex. *eNeuro*, *3*(2). https://doi.org/10.1523/ENEURO.0141-15.2016

Engel, J., Wiebe, S., French, J., Sperling, M., Williamson, P., Spencer, D., Gumnit, R., Zahn, C., Westbrook, E., & Enos, B. (2003). Practice parameter: Temporal lobe and localized neocortical resections for epilepsy. *Report of the Quality Standards Subcommittee of the American Academy of Neurology, in Association with the American Epilepsy Society and the American Association of Neurological Surgeons*, *60*(4), 538-547. https://doi.org/10.1212/01.Wnl.0000055086.35806.2d

Extercatte, J., de Haan, G. J., & Gaitatzis, A. (2015). Teaching Video NeuroImages: Frontal opercular seizures with jacksonian march. *Neurology*, *84*(11), e83-84. https://doi.org/10.1212/wnl.0000000000001363

Fedele, T., Burnos, S., Boran, E., Krayenbuhl, N., Hilfiker, P., Grunwald, T., & Sarnthein, J. (2017). Resection of high frequency oscillations predicts seizure outcome in the individual patient. *Sci Rep*, *7*(1), 13836. https://doi.org/10.1038/s41598-017-13064-1

Feigin, V. L., Abajobir, A. A., Abate, K. H., Abd-Allah, F., Abdulle, A. M., Abera, S. F., Abyu, G. Y., Ahmed, M. B., Aichour, A. N., Aichour, I., Aichour, M. T. E., Akinyemi, R. O., Alabed, S., Al-Raddadi, R., Alvis-Guzman, N., Amare, A. T., Ansari, H., Anwari, P., Ärnlöv, J., . . . Vos, T. (2017). Global, regional, and national burden of neurological disorders during 1990–2015: a systematic analysis for the Global Burden of Disease Study 2015. *The Lancet Neurology*, *16*(11), 877-897. https://doi.org/10.1016/s1474-4422(17)30299-5

Ferrari-Marinho, T., Perucca, P., Dubeau, F., & Gotman, J. (2016). Intracranial EEG seizure onset-patterns correlate with high-frequency oscillations in patients with drug-resistant epilepsy. *Epilepsy Res*, *127*, 200-206. https://doi.org/10.1016/j.eplepsyres.2016.09.009

Fisher, R. S., Acevedo, C., Arzimanoglou, A., Bogacz, A., Cross, J. H., Elger, C. E., Engel, J., Jr., Forsgren, L., French, J. A., Glynn, M., Hesdorffer, D. C., Lee, B. I., Mathern, G. W., Moshe, S. L., Perucca, E., Scheffer, I. E., Tomson, T., Watanabe, M., & Wiebe, S. (2014). ILAE official report: a practical clinical definition of epilepsy. *Epilepsia*, *55*(4), 475-482. https://doi.org/10.1111/epi.12550

Fisher, R. S., Cross, J. H., D'Souza, C., French, J. A., Haut, S. R., Higurashi, N., Hirsch, E., Jansen, F. E., Lagae, L., Moshe, S. L., Peltola, J., Roulet Perez, E., Scheffer, I. E., Schulze-Bonhage, A., Somerville, E., Sperling, M., Yacubian, E. M., & Zuberi, S. M. (2017). Instruction manual for the ILAE 2017 operational classification of seizure types. *Epilepsia*, *58*(4), 531-542. https://doi.org/10.1111/epi.13671

Frauscher, B., Bartolomei, F., Kobayashi, K., Cimbalnik, J., van 't Klooster, M. A., Rampp, S., Otsubo, H., Holler, Y., Wu, J. Y., Asano, E., Engel, J., Jr., Kahane, P., Jacobs, J., & Gotman, J. (2017). High-frequency oscillations: The state of clinical research. *Epilepsia*, *58*(8), 1316-1329. https://doi.org/10.1111/epi.13829

Fujiwara, H., Greiner, H. M., Lee, K. H., Holland-Bouley, K. D., Seo, J. H., Arthur, T., Mangano, F. T., Leach, J. L., & Rose, D. F. (2012). Resection of ictal high-frequency oscillations leads to favorable surgical outcome in pediatric epilepsy. *Epilepsia*, *53*(9), 1607-1617. https://doi.org/10.1111/j.1528-1167.2012.03629.x

Glickfeld, L. L., Roberts, J. D., Somogyi, P., & Scanziani, M. (2009). Interneurons hyperpolarize pyramidal cells along their entire somatodendritic axis. *Nat Neurosci*, *12*(1), 21-23. https://doi.org/10.1038/nn.2230

Gnatkovsky, V., de Curtis, M., Pastori, C., Cardinale, F., Lo Russo, G., Mai, R., Nobili, L., Sartori, I., Tassi, L., & Francione, S. (2014). Biomarkers of epileptogenic zone defined by quantified stereo-EEG analysis. *Epilepsia*, *55*(2), 296-305. https://doi.org/10.1111/epi.12507

Goldenholz, D. M., Ahlfors, S. P., Hamalainen, M. S., Sharon, D., Ishitobi, M., Vaina, L. M., & Stufflebeam, S. M. (2009). Mapping the signal-to-noise-ratios of cortical sources in magnetoencephalography and electroencephalography. *Hum Brain Mapp*, *30*(4), 1077-1086. https://doi.org/10.1002/hbm.20571

Granbichler, C. A., Zimmermann, G., Oberaigner, W., Kuchukhidze, G., Ndayisaba, J. P., Taylor, A., Luef, G., Bathke, A. C., & Trinka, E. (2017). Potential years lost and life expectancy in adults with newly diagnosed epilepsy. *Epilepsia*, *58*(11), 1939-1945. https://doi.org/10.1111/epi.13902

Grooms, J. K., Thompson, G. J., Pan, W. J., Billings, J., Schumacher, E. H., Epstein, C. M., & Keilholz, S. D. (2017). Infraslow Electroencephalographic and Dynamic Resting State Network Activity. *Brain Connect*, *7*(5), 265-280. https://doi.org/10.1089/brain.2017.0492

Gross, R. A. (1992). A brief history of epilepsy and its therapy in the Western Hemisphere. *Epilepsy Res*, *12*(2), 65-74. https://doi.org/10.1016/0920-1211(92)90028-r

Gumnit, R. J., & Takahashi, T. (1965). CHANGES IN DIRECT CURRENT ACTIVITY DURING EXPERIMENTAL FOCAL SEIZURES. *Electroencephalogr Clin Neurophysiol*, *19*, 63-74. https://doi.org/10.1016/0013-4694(65)90007-6

Haegelen, C., Perucca, P., Chatillon, C. E., Andrade-Valenca, L., Zelmann, R., Jacobs, J., Collins, D. L., Dubeau, F., Olivier, A., & Gotman, J. (2013). High-frequency oscillations, extent of surgical resection, and surgical outcome in drug-resistant focal epilepsy. *Epilepsia*, *54*(5), 848-857. https://doi.org/10.1111/epi.12075

Harrison, B. J., & Pantelis, C. (2010). Multiunit Activity. In I. P. Stolerman (Ed.), *Encyclopedia of Psychopharmacology* (pp. 809-809). Springer Berlin Heidelberg. https://doi.org/10.1007/978-3-540-68706-1_1350

Hashimoto, H., Khoo, H. M., Yanagisawa, T., Tani, N., Oshino, S., Kishima, H., & Hirata, M. (2020). Coupling between infraslow activities and high-frequency oscillations precedes seizure onset. *Epilepsia Open*, *5*(3), 501-506. https://doi.org/10.1002/epi4.12425

Hashimoto, H., Khoo, H. M., Yanagisawa, T., Tani, N., Oshino, S., Kishima, H., & Hirata, M. (2021). Phase-amplitude coupling between infraslow and high-frequency activities well discriminates between the preictal and interictal states. *Sci Rep*, *11*(1), 17405. https://doi.org/10.1038/s41598-021-96479-1

Herreras, O. (2016). Local Field Potentials: Myths and Misunderstandings. *Front Neural Circuits*, *10*, 101. https://doi.org/10.3389/fncir.2016.00101

Hesdorffer, D. C., Shinnar, S., Lax, D. N., Pellock, J. M., Nordli, D. R., Jr., Seinfeld, S., Gallentine, W., Frank, L. M., Lewis, D. V., Shinnar, R. C., Bello, J. A., Chan, S., Epstein, L. G., Moshe, S. L., Liu, B., Sun, S., & team, F. s. (2016). Risk factors for subsequent febrile seizures in the FEBSTAT study. *Epilepsia*, *57*(7), 1042-1047. https://doi.org/10.1111/epi.13418

Hippocrates. (c.a. 400 B.C.E.). *Prognostic. Regimen in Acute Diseases. The Sacred Disease. The Art. Breaths. Law. Decorum. Physician (Ch. 1). Dentition* (W. H. S. Jones, Trans.). Harvard University Press. https://www.loebclassics.com/view/LCL148/1923/volume.xml (1923)

Hong, S. J., Bernhardt, B. C., Gill, R. S., Bernasconi, N., & Bernasconi, A. (2017). The spectrum of structural and functional network alterations in malformations of cortical development. *Brain*, *140*(8), 2133-2143. https://doi.org/10.1093/brain/awx145

Hopcroft, J., & Tarjan, R. (1973). Algorithm 447: efficient algorithms for graph manipulation. *Commun. ACM*, *16*(6), 372–378. https://doi.org/10.1145/362248.362272

Hyvärinen, A., Karhunen, J., & Oja, E. (2001). *Independent Component Analysis*. Wiley. https://books.google.com/books?id=9TQNEAAAQBAJ

Ikeda, A., Takeyama, H., Bernard, C., Nakatani, M., Shimotake, A., Daifu, M., Matsuhashi, M., Kikuchi, T., Kunieda, T., Matsumoto, R., Kobayashi, T., & Sato, K. (2020). Active direct current (DC) shifts and "Red slow": two new concepts for seizure mechanisms and identification of the epileptogenic zone. *Neurosci Res*, *156*, 95-101. https://doi.org/10.1016/j.neures.2020.01.014

Ikeda, A., Taki, W., Kunieda, T., Terada, K., Mikuni, N., Nagamine, T., Yazawa, S., Ohara, S., Hori, T., Kaji, R., Kimura, J., & Shibasaki, H. (1999). Focal ictal direct current shifts in human epilepsy as studied by subdural and scalp recording. *Brain*, *122 (Pt 5)*, 827-838. https://doi.org/10.1093/brain/122.5.827

Ikeda, A., Terada, K., Mikuni, N., Burgess, R. C., Comair, Y., Taki, W., Hamano, T., Kimura, J., Lüders, H. O., & Shibasaki, H. (1996). Subdural recording of ictal DC shifts in neocortical seizures in humans. *Epilepsia*, *37*(7), 662-674. https://doi.org/10.1111/j.1528-1157.1996.tb00631.x

Issa, N. P., Lee, S., Wu, S., Rose, S., Towle, V. L., Warnke, P. C., van Drongelen, W., & Tao, J. X. (2018). Reply to "which small sharp spikes are benign epileptiform transients of sleep?". *Clin Neurophysiol*, *129*(11), 2495-2496. https://doi.org/10.1016/j.clinph.2018.09.002

Issa, N. P., Sedler, M. J., Del Brutto, V. J., Darsan, E., Milla, L., Montes, J., Zambrano, M., & Del Brutto, O. H. (2018). EEG Patterns in Patients With Calcified Neurocysticercosis With or Without Hippocampal Atrophy. *J Clin Neurophysiol*, *35*(4), 332-338. https://doi.org/10.1097/WNP.0000000000000471

Issa, N. P., Wu, S., Rose, S., Towle, V. L., Warnke, P. C., & Tao, J. X. (2018). Small sharp spikes as EEG markers of mesiotemporal lobe epilepsy. *Clin Neurophysiol*, *129*(9), 1796-1803. https://doi.org/10.1016/j.clinph.2018.06.011

Jacobs, J., Zijlmans, M., Zelmann, R., Chatillon, C. E., Hall, J., Olivier, A., Dubeau, F., & Gotman, J. (2010). High-frequency electroencephalographic oscillations correlate with outcome of epilepsy surgery. *Ann Neurol*, *67*(2), 209-220. https://doi.org/10.1002/ana.21847

Jacoby, A., Baker, G. A., Steen, N., Potts, P., & Chadwick, D. W. (1996). The clinical course of epilepsy and its psychosocial correlates: findings from a U.K. Community study. *Epilepsia*, *37*(2), 148-161. https://doi.org/10.1111/j.1528-1157.1996.tb00006.x

Jayakar, P., Gotman, J., Harvey, A. S., Palmini, A., Tassi, L., Schomer, D., Dubeau, F., Bartolomei, F., Yu, A., Krsek, P., Velis, D., & Kahane, P. (2016). Diagnostic utility of invasive EEG for epilepsy surgery: Indications, modalities, and techniques. *Epilepsia*, *57*(11), 1735-1747. https://doi.org/10.1111/epi.13515

Jehi, L. (2018). The Epileptogenic Zone: Concept and Definition. *Epilepsy Curr*, *18*(1), 12-16. https://doi.org/10.5698/1535-7597.18.1.12

Jeong, W., Jin, S. H., Kim, M., Kim, J. S., & Chung, C. K. (2014). Abnormal functional brain network in epilepsy patients with focal cortical dysplasia. *Epilepsy Res*, *108*(9), 1618-1626. https://doi.org/10.1016/j.eplepsyres.2014.09.006

Jing, J., Herlopian, A., Karakis, I., Ng, M., Halford, J. J., Lam, A., Maus, D., Chan, F., Dolatshahi, M., Muniz, C. F., Chu, C., Sacca, V., Pathmanathan, J., Ge, W., Sun, H., Dauwels, J., Cole, A. J., Hoch, D. B., Cash, S. S., & Westover, M. B. (2020). Interrater Reliability of Experts in Identifying Interictal Epileptiform Discharges in Electroencephalograms. *JAMA Neurol*, *77*(1), 49-57. https://doi.org/10.1001/jamaneurol.2019.3531

Jobst, B. C., Bartolomei, F., Diehl, B., Frauscher, B., Kahane, P., Minotti, L., Sharan, A., Tardy, N., Worrell, G., & Gotman, J. (2020). Intracranial EEG in the 21st Century. *Epilepsy Curr*, *20*(4), 180-188. https://doi.org/10.1177/1535759720934852

Jurcak, V., Tsuzuki, D., & Dan, I. (2007). 10/20, 10/10, and 10/5 systems revisited: their validity as relative head-surface-based positioning systems. *Neuroimage*, *34*(4), 1600-1611. https://doi.org/10.1016/j.neuroimage.2006.09.024

Kahn, E., Lane, M., & Sagher, O. (2017). Eloquent: history of a word's adoption into the neurosurgical lexicon. *J Neurosurg*, *127*(6), 1461-1466. https://doi.org/10.3171/2017.3.JNS17659

Kanazawa, K., Matsumoto, R., Imamura, H., Matsuhashi, M., Kikuchi, T., Kunieda, T., Mikuni, N., Miyamoto, S., Takahashi, R., & Ikeda, A. (2015). Intracranially recorded ictal direct current shifts may precede high frequency oscillations in human epilepsy. *Clin Neurophysiol*, *126*(1), 47-59. https://doi.org/10.1016/j.clinph.2014.05.028

Kaplan, R. M. (2011). The mind reader: the forgotten life of Hans Berger, discoverer of the EEG. *Australas Psychiatry*, *19*(2), 168-169. https://doi.org/10.3109/10398562.2011.561495

Keezer, M. R., Sisodiya, S. M., & Sander, J. W. (2016). Comorbidities of epilepsy: current concepts and future perspectives. *The Lancet Neurology*, *15*(1), 106-115. https://doi.org/10.1016/s1474-4422(15)00225-2

Kemp, B., van Beelen, T., Stijl, M., van Someren, P., Roessen, M., & van Dijk, J. G. (2010). A DC attenuator allows common EEG equipment to record fullband EEG, and fits fullband EEG into standard European Data Format. *Clin Neurophysiol*, *121*(12), 1992-1997. https://doi.org/10.1016/j.clinph.2010.05.006

Kim, D. W., Kim, H. K., Lee, S. K., Chu, K., & Chung, C. K. (2010). Extent of neocortical resection and surgical outcome of epilepsy: intracranial EEG analysis. *Epilepsia*, *51*(6), 1010-1017. https://doi.org/10.1111/j.1528-1167.2010.02567.x

Kim, W., Miller, J. W., Ojemann, J. G., & Miller, K. J. (2009). Ictal localization by invasive recording of infraslow activity with DC-coupled amplifiers. *J Clin Neurophysiol*, *26*(3), 135-144. https://doi.org/10.1097/WNP.0b013e3181a768d8

Kobau, R., Zahran, H., Thurman, D. J., Zack, M. M., Henry, T. R., Schachter, S. C., & Price, P. H. (2008). Epilepsy surveillance among adults--19 States, Behavioral Risk Factor Surveillance System, 2005. *MMWR Surveill Summ*, *57*(6), 1-20.

Koessler, L., Cecchin, T., Colnat-Coulbois, S., Vignal, J. P., Jonas, J., Vespignani, H., Ramantani, G., & Maillard, L. G. (2015). Catching the invisible: mesial temporal source contribution to simultaneous EEG and SEEG recordings. *Brain Topogr*, *28*(1), 5-20. https://doi.org/10.1007/s10548-014-0417-z

Krendl, R., Lurger, S., & Baumgartner, C. (2008). Absolute spike frequency predicts surgical outcome in TLE with unilateral hippocampal atrophy. *Neurology*, *71*(6), 413-418. https://doi.org/10.1212/01.wnl.0000310775.87331.90

Kural, M. A., Duez, L., Sejer Hansen, V., Larsson, P. G., Rampp, S., Schulz, R., Tankisi, H., Wennberg, R., Bibby, B. M., Scherg, M., & Beniczky, S. (2020). Criteria for defining interictal epileptiform discharges in EEG: A clinical validation study. *Neurology*, *94*(20), e2139-e2147. https://doi.org/10.1212/WNL.0000000000009439

Kwan, P., & Brodie, M. J. (2000). Early identification of refractory epilepsy. *N Engl J Med*, *342*(5), 314-319. https://doi.org/10.1056/nejm200002033420503

Labat, R. (1951). *Traité akkadien de diagnostics et pronostics médicaux: Transcription, traduction, introduction et facsimiles. 1. Transcription et traduction; 2. Planches*. Brill. https://brill.com/view/title/5723

Laxer, K. D., Trinka, E., Hirsch, L. J., Cendes, F., Langfitt, J., Delanty, N., Resnick, T., & Benbadis, S. R. (2014). The consequences of refractory epilepsy and its treatment. *Epilepsy Behav*, *37*, 59-70. https://doi.org/10.1016/j.yebeh.2014.05.031

Lee, C., Kim, J. S., Jeong, W., & Chung, C. K. (2014). Usefulness of interictal spike source localization in temporal lobe epilepsy: electrocorticographic study. *Epilepsy Res*, *108*(3), 448-458. https://doi.org/10.1016/j.eplepsyres.2013.12.008

Lee, S., Issa, N. P., Rose, S., Tao, J. X., Warnke, P. C., Towle, V. L., van Drongelen, W., & Wu, S. (2020). DC shifts, high frequency oscillations, ripples and fast ripples in relation to the seizure onset zone. *Seizure*, *77*, 52-58. https://doi.org/10.1016/j.seizure.2019.05.001

Lewis, D. V., Shinnar, S., Hesdorffer, D. C., Bagiella, E., Bello, J. A., Chan, S., Xu, Y., MacFall, J., Gomes, W. A., Moshe, S. L., Mathern, G. W., Pellock, J. M., Nordli, D. R., Jr., Frank, L. M., Provenzale, J., Shinnar, R. C., Epstein, L. G., Masur, D., Litherland, C., . . . Team, F. S. (2014). Hippocampal sclerosis after febrile status epilepticus: the FEBSTAT study. *Ann Neurol*, *75*(2), 178-185. https://doi.org/10.1002/ana.24081

Mader, E. C., Jr., Fisch, B. J., Carey, M. E., & Villemarette-Pittman, N. R. (2005). Ictal onset slow potential shifts recorded with hippocampal depth electrodes. *Neurol Clin Neurophysiol*, *2005*, 4.

Marks, W. J., Jr., & Laxer, K. D. (1998). Semiology of temporal lobe seizures: value in lateralizing the seizure focus. *Epilepsia*, *39*(7), 721-726. https://doi.org/10.1111/j.1528-1157.1998.tb01157.x

Merlet, I., & Gotman, J. (1999). Reliability of dipole models of epileptic spikes. *Clin Neurophysiol*, *110*(6), 1013-1028. https://doi.org/10.1016/s1388-2457(98)00062-5

Merricks, E. M., Smith, E. H., Emerson, R. G., Bateman, L. M., McKhann, G. M., Goodman, R. R., Sheth, S. A., Greger, B., House, P. A., Trevelyan, A. J., & Schevon, C. A. (2021). Neuronal Firing and Waveform Alterations through Ictal Recruitment in Humans. *J Neurosci*, *41*(4), 766-779. https://doi.org/10.1523/jneurosci.0417-20.2020

Miller, J. W., Kim, W., Holmes, M. D., & Vanhatalo, S. (2007). Ictal localization by source analysis of infraslow activity in DC-coupled scalp EEG recordings. *Neuroimage*, *35*(2), 583-597. https://doi.org/10.1016/j.neuroimage.2006.12.018

Mirsattari, S. M., Gofton, T. E., & Chong, D. J. (2011). Misdiagnosis of epileptic seizures as manifestations of psychiatric illnesses. *Can J Neurol Sci*, *38*(3), 487-493. https://doi.org/10.1017/s0317167100011914

Misra, A., Burke, J. F., Ramayya, A. G., Jacobs, J., Sperling, M. R., Moxon, K. A., Kahana, M. J., Evans, J. J., & Sharan, A. D. (2014). Methods for implantation of micro-wire bundles and optimization of single/multi-unit recordings from human mesial temporal lobe. *J Neural Eng*, *11*(2), 026013. https://doi.org/10.1088/1741-2560/11/2/026013

Modur, P. N. (2014). High frequency oscillations and infraslow activity in epilepsy. *Ann Indian Acad Neurol*, *17*(Suppl 1), S99-S106. https://doi.org/10.4103/0972-2327.128674

Modur, P. N., & Scherg, M. (2009). Intracranial broadband EEG analysis and surgical outcome: case report. *Clin Neurophysiol*, *120*(6), 1220-1224. https://doi.org/10.1016/j.clinph.2009.03.022

Modur, P. N., Vitaz, T. W., & Zhang, S. (2012). Seizure localization using broadband EEG: comparison of conventional frequency activity, high-frequency oscillations, and infraslow activity. *J Clin Neurophysiol*, *29*(4), 309-319. https://doi.org/10.1097/WNP.0b013e318262435d

Morrell, F. (1985). Secondary epileptogenesis in man. *Arch Neurol*, *42*(4), 318-335. https://doi.org/10.1001/archneur.1985.04060040028009

Morrell, F., Whisler, W. W., & Bleck, T. P. (1989). Multiple subpial transection: a new approach to the surgical treatment of focal epilepsy. *J Neurosurg*, *70*(2), 231-239. https://doi.org/10.3171/jns.1989.70.2.0231

Naess, S., Chintaluri, C., Ness, T. V., Dale, A. M., Einevoll, G. T., & Wójcik, D. K. (2017). Corrected Four-Sphere Head Model for EEG Signals. *Front Hum Neurosci*, *11*, 490. https://doi.org/10.3389/fnhum.2017.00490

Napolitano, C. E., Magunacelaya, P., & Orriols, M. (2021). Absolute spike frequency and different comorbidities in temporal lobe epilepsy. *Epilepsy Behav*, *116*, 107730. https://doi.org/10.1016/j.yebeh.2020.107730

Nasretdinov, A., Evstifeev, A., Vinokurova, D., Burkhanova-Zakirova, G., Chernova, K., Churina, Z., & Khazipov, R. (2021). Full-Band EEG Recordings Using Hybrid AC/DC-Divider Filters. *eNeuro*, *8*(4). https://doi.org/10.1523/ENEURO.0246-21.2021

Nieuwenhuys, R. (1994). The neocortex. An overview of its evolutionary development, structural organization and synaptology. *Anat Embryol (Berl)*, *190*(4), 307-337. https://doi.org/10.1007/bf00187291

Noachtar, S., & Remi, J. (2009). The role of EEG in epilepsy: a critical review. *Epilepsy Behav*, *15*(1), 22-33. https://doi.org/10.1016/j.yebeh.2009.02.035

Nunez, P. L., Srinivasan, R., & Press, O. U. (2006). *Electric Fields of the Brain: The Neurophysics of EEG*. Oxford University Press. https://books.google.com/books?id=81VRmGlprS8C

Oberlaender, M., Boudewijns, Z. S., Kleele, T., Mansvelder, H. D., Sakmann, B., & de Kock, C. P. (2011). Three-dimensional axon morphologies of individual layer 5 neurons indicate cell type-specific intracortical pathways for whisker motion and touch. *Proc Natl Acad Sci U S A*, *108*(10), 4188-4193. https://doi.org/10.1073/pnas.1100647108

Panteliadis, C. P., Vassilyadi, P., Fehlert, J., & Hagel, C. (2017). Historical documents on epilepsy: From antiquity through the 20th century. *Brain Dev*, *39*(6), 457-463. https://doi.org/10.1016/j.braindev.2017.02.002

Parvizi, J., & Kastner, S. (2018). Promises and limitations of human intracranial electroencephalography. *Nat Neurosci*, *21*(4), 474-483. https://doi.org/10.1038/s41593-018-0108-2

Paulk, A. C., Kfir, Y., Khanna, A. R., Mustroph, M. L., Trautmann, E. M., Soper, D. J., Stavisky, S. D., Welkenhuysen, M., Dutta, B., Shenoy, K. V., Hochberg, L. R., Richardson, R. M., Williams, Z. M., & Cash, S. S. (2022). Large-scale neural recordings with single neuron resolution using Neuropixels probes in human cortex. *Nat Neurosci*, *25*(2), 252-263. https://doi.org/10.1038/s41593-021-00997-0

Picchioni, D., Horovitz, S. G., Fukunaga, M., Carr, W. S., Meltzer, J. A., Balkin, T. J., Duyn, J. H., & Braun, A. R. (2011). Infraslow EEG oscillations organize large-scale cortical-subcortical interactions during sleep: a combined EEG/fMRI study. *Brain Res*, *1374*, 63-72. https://doi.org/10.1016/j.brainres.2010.12.035

Pichon, F., Nikonenko, I., Kraftsik, R., & Welker, E. (2012). Intracortical connectivity of layer VI pyramidal neurons in the somatosensory cortex of normal and barrelless mice. *Eur J Neurosci*, *35*(6), 855-869. https://doi.org/10.1111/j.1460-9568.2012.08011.x

Pillai, J., & Sperling, M. R. (2006). Interictal EEG and the diagnosis of epilepsy. *Epilepsia*, *47 Suppl 1*, 14-22. https://doi.org/10.1111/j.1528-1167.2006.00654.x

Pizzo, F., Roehri, N., Medina Villalon, S., Trebuchon, A., Chen, S., Lagarde, S., Carron, R., Gavaret, M., Giusiano, B., McGonigal, A., Bartolomei, F., Badier, J. M., & Benar, C. G. (2019). Deep brain activities can be detected with magnetoencephalography. *Nat Commun*, *10*(1), 971. https://doi.org/10.1038/s41467-019-08665-5

Pyrzowski, J., Le Douget, J. E., Fouad, A., Sieminski, M., Jedrzejczak, J., & Le Van Quyen, M. (2021). Zero-crossing patterns reveal subtle epileptiform discharges in the scalp EEG. *Sci Rep*, *11*(1), 4128. https://doi.org/10.1038/s41598-021-83337-3

Rampp, S., & Stefan, H. (2012). Ictal onset baseline shifts and infraslow activity. *J Clin Neurophysiol*, *29*(4), 291-297. https://doi.org/10.1097/WNP.0b013e31826242b3

Rathore, C., & Radhakrishnan, K. (2010). Prognostic Significance of Interictal Epileptiform Discharges After Epilepsy Surgery. *Journal of Clinical Neurophysiology*, *27*(4), 255-262. https://doi.org/10.1097/WNP.0b013e3181eaa5fa

Rathore, C., & Radhakrishnan, K. (2015). Concept of epilepsy surgery and presurgical evaluation. *Epileptic Disord*, *17*(1), 19-31; quiz 31. https://doi.org/10.1684/epd.2014.0720

Rezayev, A., Feldman, H. A., Levman, J., & Takahashi, E. (2018). Bilateral thalamocortical abnormalities in focal cortical dysplasia. *Brain Res*, *1694*, 38-45. https://doi.org/10.1016/j.brainres.2018.05.005

Rodin, E., Bornfleth, H., & Johnson, M. (2017). DC-EEG recordings of mindfulness. *Clin Neurophysiol*, *128*(4), 512-519. https://doi.org/10.1016/j.clinph.2016.12.031

Rodin, E., & Modur, P. (2008). Ictal intracranial infraslow EEG activity. *Clin Neurophysiol*, *119*(10), 2188-2200. https://doi.org/10.1016/j.clinph.2008.07.222

Rosenow, F., & Lüders, H. (2001). Presurgical evaluation of epilepsy. *Brain*, *124*(Pt 9), 1683-1700. https://doi.org/10.1093/brain/124.9.1683

Rossetti, A. O., & Kaplan, P. W. (2010). Seizure semiology: an overview of the 'inverse problem'. *Eur Neurol*, *63*(1), 3-10. https://doi.org/10.1159/000258634

Rust, N. C., Schwartz, O., Movshon, J. A., & Simoncelli, E. (2004). Spike-triggered characterization of excitatory and suppressive stimulus dimensions in monkey V1. *Neurocomputing*, *58-60*, 793-799. https://doi.org/10.1016/j.neucom.2004.01.128

Scheffer, I. E., Berkovic, S., Capovilla, G., Connolly, M. B., French, J., Guilhoto, L., Hirsch, E., Jain, S., Mathern, G. W., Moshe, S. L., Nordli, D. R., Perucca, E., Tomson, T., Wiebe, S., Zhang, Y. H., & Zuberi, S. M. (2017). ILAE classification of the epilepsies: Position paper of the ILAE Commission for Classification and Terminology. *Epilepsia*, *58*(4), 512-521. https://doi.org/10.1111/epi.13709

Schevon, C. A., Weiss, S. A., McKhann, G., Jr., Goodman, R. R., Yuste, R., Emerson, R. G., & Trevelyan, A. J. (2012). Evidence of an inhibitory restraint of seizure activity in humans. *Nat Commun*, *3*, 1060. https://doi.org/10.1038/ncomms2056

Seidel, S., Pablik, E., Aull-Watschinger, S., Seidl, B., & Pataraia, E. (2016). Incidental epileptiform discharges in patients of a tertiary centre. *Clin Neurophysiol*, *127*(1), 102-107. https://doi.org/10.1016/j.clinph.2015.02.056

Serles, W., Caramanos, Z., Lindinger, G., Pataraia, E., & Baumgartner, C. (2000). Combining ictal surface-electroencephalography and seizure semiology improves patient lateralization in temporal lobe epilepsy. *Epilepsia*, *41*(12), 1567-1573. https://doi.org/10.1111/j.1499-1654.2000.001567.x

Shi, Y., Liu, S., Wang, J., Li, C., & Zhang, J. (2021). Stigma experienced by patients with epilepsy: A systematic review and meta-synthesis of qualitative studies. *Epilepsy Behav*, *118*, 107926. https://doi.org/10.1016/j.yebeh.2021.107926

Shukla, G., & Prasad, A. N. (2012). Natural history of temporal lobe epilepsy: antecedents and progression. *Epilepsy Res Treat*, *2012*, 195073. https://doi.org/10.1155/2012/195073

Simonato, M., Loscher, W., Cole, A. J., Dudek, F. E., Engel, J., Jr., Kaminski, R. M., Loeb, J. A., Scharfman, H., Staley, K. J., Velisek, L., & Klitgaard, H. (2012). Finding a better drug for epilepsy: preclinical screening strategies and experimental trial design. *Epilepsia*, *53*(11), 1860-1867. https://doi.org/10.1111/j.1528-1167.2012.03541.x

Sinha, N., Dauwels, J., Kaiser, M., Cash, S. S., Brandon Westover, M., Wang, Y., & Taylor, P. N. (2017). Predicting neurosurgical outcomes in focal epilepsy patients using computational modelling. *Brain*, *140*(2), 319-332. https://doi.org/10.1093/brain/aww299

Smith, E. H., Liou, J. Y., Merricks, E. M., Davis, T., Thomson, K., Greger, B., House, P., Emerson, R. G., Goodman, R., McKhann, G. M., Sheth, S., Schevon, C., & Rolston, J. D. (2022). Human interictal epileptiform discharges are bidirectional traveling waves echoing ictal discharges. *Elife*, *11*. https://doi.org/10.7554/eLife.73541

Spencer, S., & Huh, L. (2008). Outcomes of epilepsy surgery in adults and children. *The Lancet Neurology*, *7*(6), 525-537. https://doi.org/10.1016/s1474-4422(08)70109-1

Sperling, M. R. (2004). The consequences of uncontrolled epilepsy. *CNS Spectr*, *9*(2), 98-101, 106-109. https://doi.org/10.1017/s1092852900008464

Staley, K. J., & Dudek, F. E. (2006). Interictal spikes and epileptogenesis. *Epilepsy Curr*, *6*(6), 199-202. https://doi.org/10.1111/j.1535-7511.2006.00145.x

Stern, J. M. (2021). Mesial temporal lobe epilepsy with hippocampal sclerosis. https://www.medlink.com/articles/mesial-temporal-lobe-epilepsy-with-hippocampal-sclerosis

Tan, M., Boston, R., Cook, M. J., & D'Souza, W. J. (2019). Risk factors for injury in a community-treated cohort of patients with epilepsy in Australia. *Epilepsia*, *60*(3), 518-526. https://doi.org/10.1111/epi.14659

Tatum, W. O. (2021). EEG in epilepsy. https://www.medlink.com/articles/eeg-in-epilepsy

Tatum, W. O. t. (2012). Mesial temporal lobe epilepsy. *J Clin Neurophysiol*, *29*(5), 356-365. https://doi.org/10.1097/WNP.0b013e31826b3ab7

Telenczuk, B., Dehghani, N., Le Van Quyen, M., Cash, S. S., Halgren, E., Hatsopoulos, N. G., & Destexhe, A. (2017). Local field potentials primarily reflect inhibitory neuron activity in human and monkey cortex. *Sci Rep*, *7*, 40211. https://doi.org/10.1038/srep40211

Téllez-Zenteno, J. F., Dhar, R., & Wiebe, S. (2005). Long-term seizure outcomes following epilepsy surgery: a systematic review and meta-analysis. *Brain*, *128*(Pt 5), 1188-1198. https://doi.org/10.1093/brain/awh449

Tellez-Zenteno, J. F., Patten, S. B., Jette, N., Williams, J., & Wiebe, S. (2007). Psychiatric comorbidity in epilepsy: a population-based analysis. *Epilepsia*, *48*(12), 2336-2344. https://doi.org/10.1111/j.1528-1167.2007.01222.x

Temkin, O. (1994). *The Falling Sickness: A History of Epilepsy from the Greeks to the Beginnings of Modern Neurology*. Johns Hopkins University Press. https://books.google.com/books?id=cPi6NR5qbsAC

Thompson, S. A., Krishnan, B., Gonzalez-Martinez, J., Bulacio, J., Jehi, L., Mosher, J., Alexopoulos, A., & Burgess, R. C. (2016). Ictal infraslow activity in stereoelectroencephalography: Beyond the "DC shift". *Clin Neurophysiol*, *127*(1), 117-128. https://doi.org/10.1016/j.clinph.2015.03.020

Trevelyan, A. J., Sussillo, D., Watson, B. O., & Yuste, R. (2006). Modular propagation of epileptiform activity: evidence for an inhibitory veto in neocortex. *J Neurosci*, *26*(48), 12447-12455. https://doi.org/10.1523/JNEUROSCI.2787-06.2006

Truccolo, W., Ahmed, O. J., Harrison, M. T., Eskandar, E. N., Cosgrove, G. R., Madsen, J. R., Blum, A. S., Potter, N. S., Hochberg, L. R., & Cash, S. S. (2014). Neuronal ensemble synchrony during human focal seizures. *J Neurosci*, *34*(30), 9927-9944. https://doi.org/10.1523/JNEUROSCI.4567-13.2014

Truccolo, W., Donoghue, J. A., Hochberg, L. R., Eskandar, E. N., Madsen, J. R., Anderson, W. S., Brown, E. N., Halgren, E., & Cash, S. S. (2011). Single-neuron dynamics in human focal epilepsy. *Nat Neurosci*, *14*(5), 635-641. https://doi.org/10.1038/nn.2782

Tryba, A. K., Merricks, E. M., Lee, S., Pham, T., Cho, S., Nordli, D. R., Jr., Eissa, T. L., Goodman, R. R., McKhann, G. M., Jr., Emerson, R. G., Schevon, C. A., & van Drongelen, W. (2019).

Role of paroxysmal depolarization in focal seizure activity. *J Neurophysiol*, *122*(5), 1861-1873. https://doi.org/10.1152/jn.00392.2019

Tufenkjian, K., & Luders, H. O. (2012). Seizure semiology: its value and limitations in localizing the epileptogenic zone. *J Clin Neurol*, *8*(4), 243-250. https://doi.org/10.3988/jcn.2012.8.4.243

van 't Klooster, M. A., Leijten, F. S., Huiskamp, G., Ronner, H. E., Baayen, J. C., van Rijen, P. C., Eijkemans, M. J., Braun, K. P., Zijlmans, M., & group, H. F. O. s. (2015). High frequency oscillations in the intra-operative ECoG to guide epilepsy surgery ("The HFO Trial"): study protocol for a randomized controlled trial. *Trials*, *16*, 422. https://doi.org/10.1186/s13063-015-0932-6

Van Drongelen, W. (2018). *Signal processing for neuroscientists*. Academic press.

Vanhatalo, S., Holmes, M. D., Tallgren, P., Voipio, J., Kaila, K., & Miller, J. W. (2003). Very slow EEG responses lateralize temporal lobe seizures: an evaluation of non-invasive DC-EEG. *Neurology*, *60*(7), 1098-1104. https://doi.org/10.1212/01.wnl.0000052993.37621.cc

Vanhatalo, S., Palva, J. M., Holmes, M. D., Miller, J. W., Voipio, J., & Kaila, K. (2004). Infraslow oscillations modulate excitability and interictal epileptic activity in the human cortex during sleep. *Proc Natl Acad Sci U S A*, *101*(14), 5053-5057. https://doi.org/10.1073/pnas.0305375101

Vollmar, C., Stredl, I., Heinig, M., Noachtar, S., & Remi, J. (2018). Unilateral temporal interictal epileptiform discharges correctly predict the epileptogenic zone in lesional temporal lobe epilepsy. *Epilepsia*, *59*(8), 1577-1582. https://doi.org/10.1111/epi.14514

Weiss, S. A., Alvarado-Rojas, C., Bragin, A., Behnke, E., Fields, T., Fried, I., Engel, J., Jr., & Staba, R. (2016). Ictal onset patterns of local field potentials, high frequency oscillations, and unit activity in human mesial temporal lobe epilepsy. *Epilepsia*, *57*(1), 111-121. https://doi.org/10.1111/epi.13251

Weiss, S. A., Banks, G. P., McKhann, G. M., Jr., Goodman, R. R., Emerson, R. G., Trevelyan, A. J., & Schevon, C. A. (2013). Ictal high frequency oscillations distinguish two types of seizure territories in humans. *Brain*, *136*(Pt 12), 3796-3808. https://doi.org/10.1093/brain/awt276

Weiss, S. A., Lemesiou, A., Connors, R., Banks, G. P., McKhann, G. M., Goodman, R. R., Zhao, B., Filippi, C. G., Nowell, M., Rodionov, R., Diehl, B., McEvoy, A. W., Walker, M. C., Trevelyan, A. J., Bateman, L. M., Emerson, R. G., & Schevon, C. A. (2015). Seizure localization using ictal phase-locked high gamma: A retrospective surgical outcome study. *Neurology*, *84*(23), 2320-2328. https://doi.org/10.1212/wnl.0000000000001656

Wennberg, R., Quesney, F., Olivier, A., & Dubeau, F. (1997). Mesial temporal versus lateral temporal interictal epileptiform activity: comparison of chronic and acute intracranial recordings. *Electroencephalogr Clin Neurophysiol*, *102*(6), 486-494. https://doi.org/10.1016/s0013-4694(97)96018-5

Wennberg, R., Tarazi, A., & Zumsteg, D. (2018). Which small sharp spikes are benign epileptiform transients of sleep? *Clin Neurophysiol*, *129*(11), 2492-2494. https://doi.org/10.1016/j.clinph.2018.08.026

Wennberg, R., Valiante, T., & Cheyne, D. (2011). EEG and MEG in mesial temporal lobe epilepsy: where do the spikes really come from? *Clin Neurophysiol*, *122*(7), 1295-1313. https://doi.org/10.1016/j.clinph.2010.11.019

Wilfong, A. (2022). Epilepsy syndromes in children. https://www.uptodate.com/contents/epilepsy-syndromes-in-children

Williams, L. P. (2021). Michael Faraday. https://www.britannica.com/biography/Michael-Faraday

Wilson, J. V., & Reynolds, E. H. (1990). Texts and documents. Translation and analysis of a cuneiform text forming part of a Babylonian treatise on epilepsy. *Med Hist*, *34*(2), 185-198. https://doi.org/10.1017/s0025727300050651

Wong, S. M., Arski, O. N., Workewych, A. M., Donner, E., Ochi, A., Otsubo, H., Snead, O. C., 3rd, & Ibrahim, G. M. (2021). Detection of high-frequency oscillations in electroencephalography: A scoping review and an adaptable open-source framework. *Seizure*, *84*, 23-33. https://doi.org/10.1016/j.seizure.2020.11.009

World Health Organization. (2005). *Atlas: epilepsy care in the world*. World Health Organization.

World Health Organization. (2022). *Epilepsy*. https://www.who.int/news-room/fact-sheets/detail/epilepsy

Wu, S., Kunhi Veedu, H. P., Lhatoo, S. D., Koubeissi, M. Z., Miller, J. P., & Luders, H. O. (2014). Role of ictal baseline shifts and ictal high-frequency oscillations in stereo-electroencephalography analysis of mesial temporal lobe seizures. *Epilepsia*, *55*(5), 690-698. https://doi.org/10.1111/epi.12608

Yamazaki, M., Tucker, D. M., Fujimoto, A., Yamazoe, T., Okanishi, T., Yokota, T., Enoki, H., & Yamamoto, T. (2012). Comparison of dense array EEG with simultaneous intracranial EEG for interictal spike detection and localization. *Epilepsy Res*, *98*(2-3), 166-173. https://doi.org/10.1016/j.eplepsyres.2011.09.007

Yang, J. C., Paulk, A. C., Salami, P., Lee, S. H., Ganji, M., Soper, D. J., Cleary, D., Simon, M., Maus, D., Lee, J. W., Nahed, B. V., Jones, P. S., Cahill, D. P., Cosgrove, G. R., Chu, C. J., Williams, Z., Halgren, E., Dayeh, S., & Cash, S. S. (2021). Microscale dynamics of electrophysiological markers of epilepsy. *Clin Neurophysiol*, *132*(11), 2916-2931. https://doi.org/10.1016/j.clinph.2021.06.024

Zack, M. M., & Kobau, R. (2017). National and State Estimates of the Numbers of Adults and Children with Active Epilepsy - United States, 2015. *MMWR Morb Mortal Wkly Rep*, *66*(31), 821-825. https://doi.org/10.15585/mmwr.mm6631a1

Zhang, Y., van Drongelen, W., & He, B. (2006). Estimation of in vivo brain-to-skull conductivity ratio in humans. *Appl Phys Lett*, *89*(22), 223903-2239033. https://doi.org/10.1063/1.2398883

Zhang, Z. W., & Deschênes, M. (1997). Intracortical axonal projections of lamina VI cells of the primary somatosensory cortex in the rat: a single-cell labeling study. *J Neurosci*, *17*(16), 6365-6379. https://doi.org/10.1523/jneurosci.17-16-06365.1997

Zijlmans, M., Worrell, G. A., Dumpelmann, M., Stieglitz, T., Barborica, A., Heers, M., Ikeda, A., Usui, N., & Le Van Quyen, M. (2017). How to record high-frequency oscillations in epilepsy: A practical guideline. *Epilepsia*, *58*(8), 1305-1315. https://doi.org/10.1111/epi.13814

APPENDIX

Guide to Github repositories

Custom scripts written for the projects described in this thesis are available publicly in Github repositories. For ease of navigation, this section lists scripts with their corresponding results. The figure reference is to indicate that the output of a script was used to generate the figure. In many cases, the script does not directly generate the referenced figure. Not all files and scripts found in the repositories are listed here. Only key and representative scripts are described here for guidance purposes.

This appendix was written June 20, 2022, therefore any versions that may have been created after this date may not correspond to this thesis exactly.

Chapter 2: Manifestation of hippocampal interictal discharges on clinical scalp EEG recordings
Repository link: https://github.com/sominlee14/hippocampal_ied

File Name	File Type	Description
channel_locs	.mat	Variable containing coordinates for scalp EEG electrodes. Used to calculate dipole angle. (Fig. 2.4)
dipole_angle_calculation	.m	Calculates dipole angle of scalp STA (Fig. 2.4)
grouped_sta_calculation	.m	Calculates STA scalp and intracranial interictal discharges by group (Fig. 2.1)
peak_detection	.m	Detects interictal discharges using hippocampal intracranial recordings
xcorr_lag_simulation	.m	Monte-Carlo simulation to determine jitter and acceptable range for zero lag in cross-correlation analysis (Fig. 2.3B)

Chapter 3: Digital reconstruction of infraslow activity in ictal recordings
Repository link: https://github.com/sominlee14/deconvolution_based_inverse_filter

File Name	File Type	Description
calculate_uir_portable_system	.mlx	MATLAB Live Script demonstrating how to characterize a system's unit impulse response using a step input signal (Fig. 3.3)
inverse_filter_mixed_sine	.mlx	MATLAB Live Script demonstrating application of deconvolution filter to a synthetic sine signal. Also calculates amplitude spectra and phase spectra (Fig. 3.6)
noise_robustness	.mlx	MATLAB Live Script showing that deconvolution method is robust to noise (Fig. 3.4)

Chapter 4: Characterization of the spatiotemporal relationship between spiking and LFP during focal seizures
Repository link: https://github.com/sominlee14/stSCA_scripts

File Name	File Type	Description
fx_calculate_temporal_sta	.m	Function that calculates just the temporal STA (e.g., Fig. 4.2)
fx_calculate_spatiotemporal_sta	.m	Function that calculates the spatiotemporal SCA (Fig. 4.1)
fx_calculate_temporal_sta_subset_channels	.m	Function that chooses a random subset of channels for spike timing to calculate the temporal STA (Fig. 4.12)
fx_find_spikes_columbia_data	.m	Function for spike detection
fx_randomize_spike_times	.m	Function that shuffles spike times before calculating st-SCA (Fig. 4.7)